# Electron Transport in 2-Dimensional Films: FePt-C Nanogranular Films, Ag Nanocluster Films and Microfabricated Magnetic Tunnel Junctions

Thesis submitted for the degree of Doctor of Philosophy in Physics

by

Joshy Joseph
13PHPH20

Under the guidance of Dr. A. Rajanikanth



School of Physics University of Hyderabad Hyderabad - 500 046, India

November 2020



## **DECLARATION**

I, Joshy Joseph, hereby declare that the matter embodied in this thesis entitled "Electron transport in 2-dimensional films: FePt-C nanogranular films, Ag nanocluster films and microfabricated magnetic tunnel junctions", is the result of investigations carried out by me in the School of Physics, University of Hyderabad, Hyderabad, India under the supervision of Dr. A. Rajanikanth and it is a bonafide research work which is also free from plagiarism. I also declare that it has not been submitted previously in part or in full to this university or any other university or institute for the award of any degree or diploma.

Hyderabad

November 17, 2020

Joshy Joseph 13PHPH20



#### CERTIFICATE

This is to certify that the thesis entitled, "Electron transport in 2-dimensional films: FePt-C nanogranular films, Ag nanocluster films and microfabricated magnetic tunnel junctions", submitted by Joshy Joseph bearing Reg. No. 13PHPH20 in partial fulfillment of the requirements for the award of Doctor of Philosophy in the School of Physics is a bonafide work carried out by him under my direct supervision.

This thesis is free from plagiarism and has not been submitted previously in part or in full to this or any other University or Institution for the award of any degree or diploma. Further, The student has passed the four courses towards the fulfillment of course-work required for Ph.D.

Dean

School of Physics

DEAN

School of Physics University of Hyderabad HYDERABAD - 500 046. Dr. A. Rajanikanth

Research Supervisor

School of Physics

Dr. A. Rajani Kanth School of Physics University of Hyderabad Hyderabad-500 046, INDIA.



#### **ACKNOWLEDGEMENT**

It would be impossible to complete this PhD without the support of many people in various ways. On the journey of research, here, I was convinced not to be hesistated to ask someone for some help provided I offer help to others in their needs. And the impact was huge. With great gratitude I would like to acknowledge all the people who stood with me in many ways in this journey.

My research supervisor, Dr. A. Rajanikanth, gave me a lot of opportunities to learn and work on various experimental techniques. He inspired me to become a skilled and keen researcher and to work passionately. He meticulously and systematically guided me on all the junctions of this journey. I extend my overwhelming gratitude to him.

Whenever I visit Prof. Bansal, I have come out with so much of enthusiasm to do research. He has always motivated me to do research with great thirst and shared his experiences and ideas. Dr. Manivel Raja was another person who encouraged me at different occasions. Dr. Takahashi from NIMS, Japan, provided the FePt samples according to the requirement. Dr. Karthik Raman and his student, Satyaki, from TIFR, Hyderabad, offered the resistivity measurement at 5 T field. I remember them with gratitude.

I would like to thank my doctoral committee members, Prof. S. Srinath and Prof. A. Chatterjee. Fruitful discussions with them and their suggestion have helped me in this journey. Further, I thank Prof. Srinath for encouraging me at various occasions and offering support generously.

I express my gratitude to the Dean, Prof. A. Chatterjee, previous deans Prof.



V. Seshubai, Prof. Bindu A Bambah and Prof. S Chaturvedi and all the faculties in school of physics for their support during this period.

My lab members Dr. Seema Awasthi, Dr. Charan, Dr. Raju Botta, Jitu, Venki, Jonathan and Praveen supported me well and were good companions in the midst of intense research to have a cup of tea. I would like to mention Dr. Seema for motivating me at various times towards research. I extend my gratitude to all of them.

I had been stuck at various occasions of research, where I was in need of other lab facilities or experienced hands and minds and academic discussions. In this regard, I would be grateful to Ravikumar, Ravi DMRL, Arun Nimmala, Sandeep, Sravani, Harsha, Sreejith and many others. Further, I wish to acknowledge the non-teaching staffs in the School of Physics, especially Mr. Mukunda Reddy, Office staffs during the period, Mr. T. Abraham, Ms. Deepthi, Mr. Sudarshan Singh, Mr. Sekhar, etc. for their timely assistance at various occasions.

A good set of friends means a lot and necessary at the break of the day to revamp in the next day. Samlan, Shihab, Andrews, Masroor, Zuhair, Midhunlal, Vineeth, and many others come in this list. I thank them for their company.

Finally, I would like to thank my parents and brother who supported me all the way throughout my academic endeavor. I remember the encouragement and support from Shaju uncle, Jessy aunt and many more, my cousins and in-laws and my wife, Geethu, who came in the middle of this journey stood beside me in the midst of joy and sorrow giving all the care and courage to complete this PhD work. I extend my gratitude to all of them.

November 17, 2020

Joshy Joseph



## **ABSTRACT**

Nanomaterials offer wide range of applications arising from the tunability of properties of these materials by size, structure and dimension. Increased surface to volume ratio and quantum confinement of electrons in nanostructures results in emergence of different physical, chemical and optical properties. Nanogranular and nanocluster films are potential materials for tuning the electron transport by external electric field. In this regard, this thesis discusses on the electron transport mechanism in FePt-C nanogranular films and Ag nanocluster films by varying the coverage of granules/clusters on the surfaces. In addition, a simple and cost effective techniqe of fabricating magnetic tunnel junctions using optical lithography has been conducted.

FePt-C granular films show huge perpendicular magnetic anisotropy. A set of films with varying average intergranular separation was prepared and measured the resistivity. Hopping transport in these films are found to be tunable with intergranular separation to different mechanisms such as Mott Variable range hopping, Efros-Shklovskii variable range hopping and extended critical regime above 25K. An enhanced conduction was observed below 25 K with a metal insulator transition shown by reduced activation energy calculation. Further, enhanced conduction was modelled to spin dependent transport of tunneling electrons.

Ag nanoclusters were deposited at various surface coverage with different deposition time. Metallic conductivity with emergance of minima was observed as the deposition time reduces. Metallic conductivity was fitted to Bloch-Gruneisen formula modified for different scattering mechanisms such as carrier-carrier interaction. The region of resistivity minimum and below was fitting to an additional  $-T^{1/2}$  dependence proposed by Altshuler and Aronov considering interference of electron-electron scattering at low temperature. Hall effect measurement of the film with lowest resistance have shown a Hall coefficient of one order higher compared to the bulk counterpart indicating the emergence of Giant Hall effect. Hall effect of other samples could not be measured because of the large noice. The Hall effect can be further improved by engineering the morphology.

Magnetic tunnel junctions offer huge magnetoresistance useful for magnetic field sensor, read-head, MRAM, etc. A simple and cost effective microfabrication technique has been explored by using photolithography as the only tool for patternig the film. Exchange bias of IrMn/FeCo bilayer has been optimized to pin the reference layer magnetization to single direction. Fabrication process has been elaborated which consists of four step mask process. The J-V characteristics of the junctions were fitted to Simmon's relation for tunneling current. A TMR of upto 7 % has been obtained. Further, a circuit has been designed integrating the MTJs into bridge circuit and amplifying using op-amp and measured the output. Though the TMR ratio is quite less, the given method gives a simple and viable technique as it can be fabricated in the absence of expensive instruments such as material selective ion etching.

Two dimensional nanomaterials offer controllable electronic properties suitable for various electric and magnetic field controlled devices. The research on this has to be further explored.

# **Contents**

1	Intr	roduction		
	1.1	Introduction	1	
	1.2	Nanotechnology	2	
	1.3	Nanomaterials	4	
		1.3.1 Synthesis of nanomaterials	6	
		1.3.2 Properties of nanomaterials	7	
		1.3.3 Electron transport in nanomaterials	8	
		1.3.3.1 Quantum transport	9	
	1.4	Nanogranular films	11	
	1.5	Nanocluster films	12	
	1.6	Magnetic tunnel junctions	13	
	1.7	Motivation	14	
	1.8	Plan of the thesis	15	
	Rofe	prences	19	

2	Exp	perimental Techniques		
	2.1	Samp	le preparation	23
		2.1.1	Sputtering	24
		2.1.2	Nanocluster deposition	26
		2.1.3	Electron beam lithography	29
		2.1.4	Optical lithography	31
	2.2	Chara	cterization	33
		2.2.1	Transmission electron eicroscopy	33
		2.2.2	Scanning electron microscopy	35
		2.2.3	Cryogenic probe station	37
		2.2.4	Cryogenic magnetic probe station	40
		2.2.5	Physical Property Measurement System - Vibrating Sample	41
			Magnetometry	41
	2.3	Analy	sis	42
		2.3.1	Curve fitting	42
	2.4	Concl	usion	43
	Refe	erences		45
3	Elec	tron Tr	ansport in FePt-C nanogranular films	47
	3.1	Introd	luction	47
	3.2	Sampl	e preparation	50

3.3 Characterization and analysis				51
		3.3.1	TEM microstrucure	51
		3.3.2	Magnetization versus field	54
		3.3.3	Resistivity versus temperature	55
			3.3.3.1 Anderson localization	56
			3.3.3.2 Nearest neighbour hopping	57
			3.3.3.3 Mott variable range hopping	58
			3.3.3.4 Efros-Shklovskii variable range hopping	59
			3.3.3.5 Analysis of resistivity data	60
		3.3.4	Reduced activation energy	63
		3.3.5	Model for spin dependent electron transport	66
	3.4	Concl	usion	69
	Refe	erences		71
1	El	tura a Ta	an angular Anguna dagatan Class	75
4	Elec		ansport in Ag nanocluster films	<b>7</b> 5
	4.1	Introd	uction	<b>7</b> 5
	4.2	Sampl	le preparation and Measurements	77
	4.3	Chara	cterization and Analysis	79
		4.3.1	FESEM characterization	79
		4.3.2	Resistivity of Ag nanoclusters	81
			4.3.2.1 Resistivity of Metals	81

		4.3.2.2 Minumum in the resistivity 8	35
		4.3.3 Hall effect	39
		4.3.3.1 Hall effect of Ag nanocluster film 9	90
	4.4	Conclusion	93
	Refe	rences	95
5	Mic	rofabrication of Magnetic Tunnel Junction using Photolithography 9	99
	5.1	Introduction	99
	5.2	Optimization of the growth of MgO (001) over $Si/SiO_2$ substrate . 10	)1
	5.3	Optimization of exchange bias in IrMn/FeCo bilayer 10	)2
	5.4	Microfabrication of magnetic tunnel junction	)7
	5.5	J-V characteristics of MTJ	l 1
	5.6	Tunneling Magnetoresistance of MTJ	۱5
	5.7	Circuit design for MTJ sensor	16
	5.8	Conclusion	18
	Refe	rences	۱9
6	Con	clusion 12	21
	6.1	Summary	21
	6.2	Future perspectives	25
	Rofe	rences 12	77

List of publications, Conferences and Workshops	129
Plagiarism report	131



## Chapter 1

## Introduction

This chapter introduces nanomaterials as the nanogranular films, nanocluster films and magnetic tunnel junctions studied in the thesis come under this class of materials. Importance of these materials and the physical and electrical properties of these materials in comparison with its bulk counterparts are discussed and finally arrives at nanogranular films, nanocluster films and magnetic tunnel junctions. In addition to that, motivation for the present work and organization of the thesis have been sketched out.

## 1.1 Introduction

The materials in the solid form have generally been classified into crystalline and amorphous. Though most stable form of any material is crystalline as free energy of the material is the least in this form, it is not easy to make a material perfectly crystalline. Many methods such as sputtering, molecular beam epitaxy, substrate heating, annealing, etc. have been adopted by researchers around the world to

make the materials crystalline. On the other side, the theory of crystalline materials has grown so much with the help of quantum theory, group theory, Fourier transform, density functional theory, etc. as the fundamental building block in a crystal (atom) has been arranged in a regular pattern. In such a scenario, the emergence of nanotechnology has paved the way to a new era of scientific curiousity and understanding with the unique properties of materials in nanoscale bringing out diverse applications. Many of the fascinating properties of nanomaterials are due to the increase in surface to volume ratio and quantum mechanical effects due to its size. A tremendous increase in the surface to volume ratio occurs in nanoscale as shown in figure 1.1. As the size of the material reduces to nanoscale the energy level spacing increases and this leads to quantum confinement [1]. This can be understood from the particle in a box model in quantum mechanics. Energy level spacing increases quadratically as the length of the box (particle size) reduces. Thus, exploration of quantum mechanical properties hidden in nanomaterials can offer ample opportunities to provide applicable results to facilitate human needs.

## 1.2 Nanotechnology

The idea of nanotechnology was originated from the well known lecture of Richard Feynman in 1959, titled "There is plenty of room at the bottom" [3]. Scientists further observed that the properties of the materials drastically change in nanoscale. For the last three decades, nanotechnology has achieved tremendous progress in perceiving, fabricating and controlling structures in nanoscale. Thus, nanotechnology has grown as an area of science endowing a lot of applications

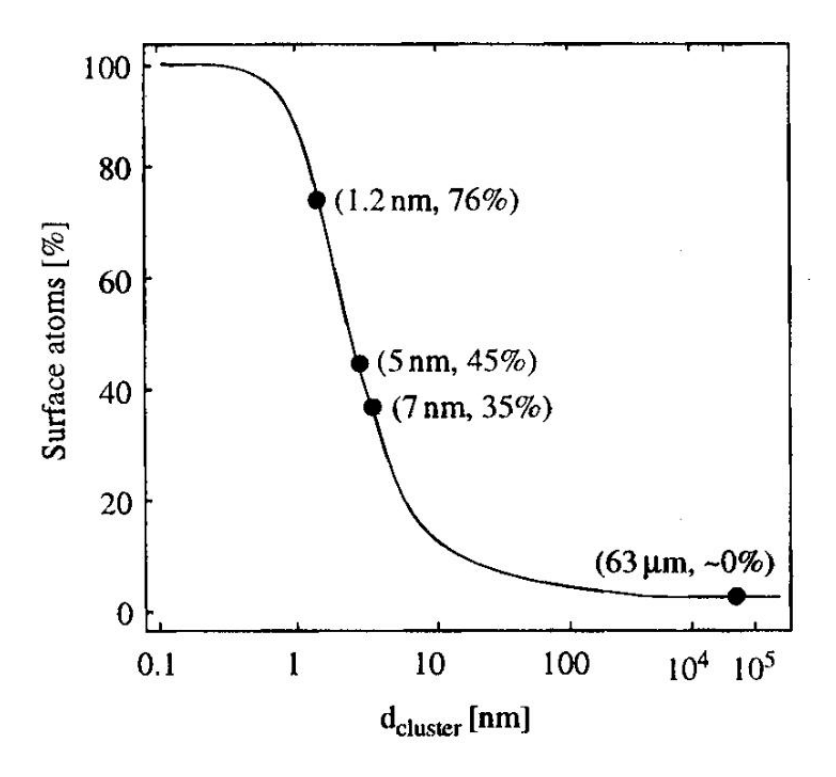


*Figure 1.1:* Depicts the percentage of surface atoms with respect to the diameter of cluster [2].

useful in daily life. For example, nanoscale films are used in eyeglasses, computer screens, glass windows, etc. as self cleaner, dust repellent, anti-reflection, scratch resistant, protection from UV radiation, water repellent etc.. The control over the size in nanoscale, thus, has a key role in modifying physical and chemical properties of materials. The advent of electron microscopes, electron lithography system etc. eased the understanding and development of nanotechnology into a fast growing mode. The main reason behind the tremendous growth of nanotechnology is, without any doubt, the innumerable applications coming out from the hidden physical phenomena exposed in time as a result of the curiosity of the human kind to know the hidden truths and to miniaturize the utilities.

## 1.3 Nanomaterials

Nanomaterials are those materials which have atleast one dimension or constituent element in nanosize, i.e., less than 100 nm and they exhibit the size dependent properties generally below 50 nm [4]. In this regard, nanomaterials can be divided into four groups. They are:

- 1. Nanoclusters (0 Dimensional(0D))
- 2. Nanotubes and rods (1D)
- 3. Nanolayers (2D)
- 4. Nanostructures (3D)

Figure 1.2 shows the classification of nanomaterials in general. In the representation of mDn, m represents the dimension of the system and n represents the dimension of the constituent element. This thesis mainly focuses on the 2D0 structures (nanogranular and nanocluster films) and 2D2 structures (magnetic tunnel junctions).

In terms of the type of constituent materials nanomaterials are classified into organic nanomaterials, inorganic nanomaterials and carbon based nanomaterials [6]. Polymeric and lipid based nanomaterials comes under organic nanomaterials. Metal, metal oxide, ceramics and semiconductor nanomaterials are inorganic nanomaterials and fullerenes, carbon nanotubes, carbon nanofibres and graphene constitute carbon based nanomaterials.

Atoms on the surface have a great role in the properties of nanomaterials since the percentage of surface atoms increases with reduced size as shown in figure

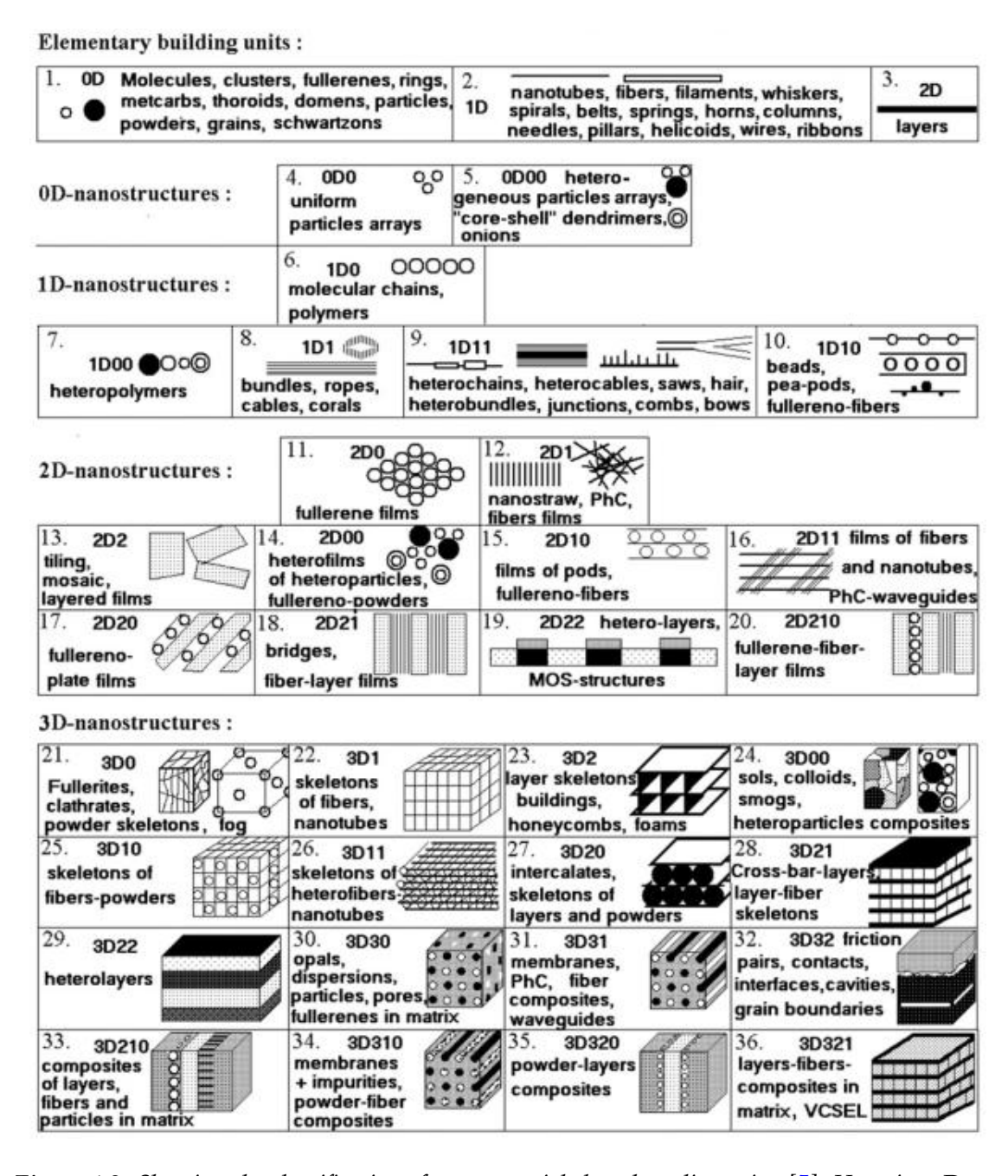


*Figure 1.2:* Showing the classification of nanomaterials based on dimension [5]. Here, in mDn, n represents the dimension of constituent element and m, dimension of the overall structure.

1.1. The surface atoms do not have all bonds as the neighbouring atoms are less. In such a case, they either form new bond with other atoms adsorbed or create bonds mutually. This process is known as reconstruction as shown in the figure 1.3. The enhanced surface atoms and the reconstruction of these atoms have a role on the properties of nanomaterials.

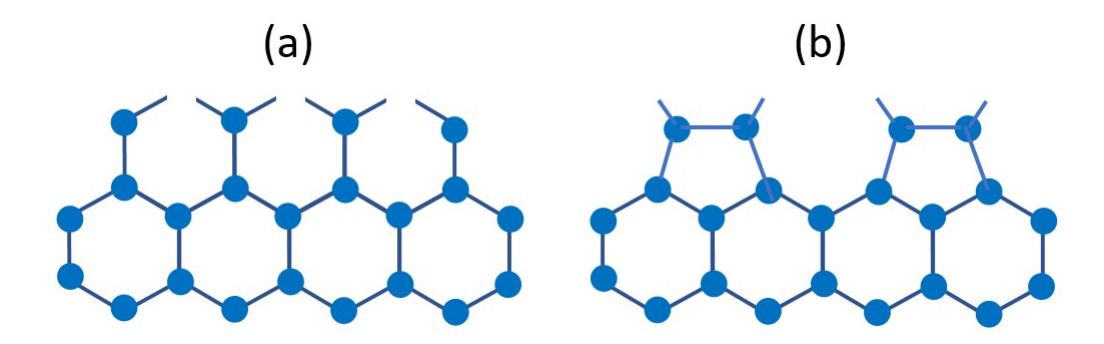


Figure 1.3: (a) Before and (b) after reconstruction of unbonded surface atoms.

## 1.3.1 Synthesis of nanomaterials

Genarally, there are two methods for the synthesis of nanomaterials. They are top-down and bottom-up approaches. A good analogy to top-down and bottom up methods are carving the sculpture from stone and building the sculpture using clay respectively: Making the structure by removing unwanted portions of a bigger material is the former method, whereas, making the structure by adding atom by atom or molecule by molecule is the later method. While attrition or milling is an appropriate example for top-down approach, colloidal dispersion is an example for bottom-up approach.

The top-down approach uses lithography techniques and etching processes to

make nanomaterials. Advantage of this method is that we have a control over the arrangements of nanoparticles. However, etching processes and lithography can damage the crystal structure and create imperfections on the surface of nanostructures. Such imperfections have huge impact on nanomaterials as the physical properties of these materials largely depend on the surface atoms due to the increased surface to volume ratio. For example, surface imperfection in nanostructures reduces thermal conductivity because of the inelastic surface scattering, which in turn produces excessive heat causing challenges to the device design.

The bottom-up approach of making nanostructures is building it atom by atom or molecule by molecule. This method guarantees less imperfection, short and long range ordering of the clusters and homogeneity in chemical ordering. These advantages of bottom-up are mainly due to the reduction of Gibbs free energy which leads to a thermal equilibrium against the internal stress, imperfections and contamination occurring in the top-down approach. In the present work, nanogranular films, nanocluster films and magnetic tunnel junctions have been prepared through bottom-up approach.

## 1.3.2 Properties of nanomaterials

Nanomaterials are used in diverse applications because of the tunable nature of electronic, optical and catalytic properties originating from the size and the arrangement of the constituent elements. Melting point and phase transition temperature reduces as the size of the nanomaterial comes down. This is due to the increase in surface energy with more number of surface atoms [7]. Nanomaterials are found to have higher mechanical strength in comparison to its bulk counter-

part. For example, graphene is treated as the strongest material in the world. This quality of the nanomaterial is ascribed to crystalline nature of its constituent elements. Energy level spacing increases as the size of the structure reduces to nanoscale. Similar to the particle in a box experiment, the electrons are spacially confined as the size of the nanoparticle reduce to the De-Broglie wavelength. Expression for the energy of  $n^{th}$  level is

$$E_n = \frac{n^2 \pi^2 \hbar^2}{8ML^2} \tag{1.1}$$

where, M is the mass of electron and L is the diameter of nanoparticle. As the size of the particle decreases, the energy increases which result in increased energy level spacing.

Different optical properties associated with the nanostructures results from the enhanced energy level spacing and surface plasmon resonance. The surface plasmon resonance is the coherent excitation of free electrons in the conduction band induced by the incident light. The incident light polarizes the negatively charged electrons and positively charged lattice. The restoring force creates oscillation at a particular frequency of electrons and thereby the characteristic surface plasmon resonance [7].

## 1.3.3 Electron transport in nanomaterials

The electron transport in bulk metals has been well established with the Boltzman transport equation and related kinetic equations. These theories have its roots in the following assumptions. Scattering occurs in space locally and at a single point, they are weak and fields are low such that they can be treated as separate

perturbations and time scale of events are slow compared to the mean free path of electrons in these systems [8]. In short, potential varies slowly in both spatial and temporal scales of scattering events.

Nanomaterials are another class of materials whilst electron transport is the measure. Most of the physical phenomenon associated with these systems are revealed by transport mechanism as interactions play crucial role in these systems. The assumptions of Boltzman transport equations are broken in the case of nanomaterials as the length scale of material constituents comes down to the mean free path of electrons in the system. The different mechanisms associated with the transport mechanism in these structures are surface scattering, grain boundary scattering, quantized transport (ballistic conduction), tunneling due to coulomb charging [7].

#### 1.3.3.1 Quantum transport

There are three different ways in which size effect in nanostructure can result in conduction. In 1980s scientists observed that mean free path of electrons in GaAs/AlGaAs grows as large as of the order of 100  $\mu$ m at low temperature. The structures below this size can show strange electronic properties due to the ballistic electron transport, i.e., electrons tunneling between the structures experiences very little or no scattering and results in interference of electrons [8]. In ballistic conduction, there is no elastic scattering involved and thus no reduction in conduction and a quantized conduction is observed [7].

The electron tunneling across charged grains can occur when the contact resistance between the grains are larger than the resistance within the grain and the

capacitance of the grain is small such that adding a single electron needs significant charging energy. In such grains, when sufficient voltage is applied, electron can tunnel one at a time. This leads to the mechanism called coulomb staircase [7]. The nanomaterials showing this property is a good candidate for single electron transistor.

The tunneling transport is another mechanism when the nanograins are separated by 1-2 nanometers of insulator. When the insulator is very thin, the electronic wave function overlaps within the insulator which leads to tunneling of electrons through the insulating/dielectric medium while electric field is applied [7]. In general, the tunneling transport exponentially decay as the thickness of the insulator barrier is increased.

Further, a weak coupling between grains can modify the tunneling of the electrons in nanomaterials. Therefore, electron transport in nanomaterials has a great significance in understanding quantum mechanical effects played by the electrons in these systems. Thus, electron transport, here, is controlled by the interplay of various scattering mechanisms such as interaction between grains, surface scattering, scattering of electrons by phonon and other electrons. Though, a qualitative understanding of electron transport in metallic granular system has been achieved, a quantitative measurement of such a mechanism is still lacking [9]. Further, the transport in 2-D granular films have not been studied enough.

## 1.4 Nanogranular films

Nanogranular films consist of granules of nanosize distributed in another material. Generally, there are two ways in which granular films are prepared and they are metal-insulator granular films and magnetic-non-magnetic metal/insulator granular films. The only condition to form metal insulator granular system is that they should be immiscible. Here, one acts as the grain growth controller of the other. Magnetic granular films have been widely studied since the magnetic moment of the metal granule is enhanced with reduced size. The reason for the enhancement of magnetic moment is the unpaired surface atoms of the magnetic nanograins. As the size of the ferromagnetic material is reduced, the favorable low energy state of the system comes to single domain and further reduction leads the system to a superparamagnetic state, where the spins of the atoms flip randomly. Therefore, the limitation of magnetic granules is that the ferromagnetic property is lost beyond a reduced size of the granule. The magnetocrystalline energy is directly proportional to both anisotropy constant and volume of granule. Therefore, as the anisotropy constant of the material is bigger, the size of the single domain granules becomes smaller. Hard magnetic materials becomes hardest with largest single domain grain of that and the soft magnetic material become softer as the grain size reduces [10]. It can be seen that intensive research has been taking place around the world to reduce size of single domain granule to utilize them for data storage applications [11].

Though electron transport in granular films is a well discussed area [12–17], it has not been completely understood. Different transport mechanisms such as hopping, fluctuation induced tunneling, percolation, etc. have been observed

in different granular systems with various volume percentage of metal grains in metal insulator composition. However, the origin of different transport phenomenon has not been experimentally understood. Therefore, it is an interesting field to study observing the possibility of utilizing them in electric field controlled devices.

#### 1.5 Nanocluster films

Nanoclusters are aggregates of atoms from a few to several thousands in number which can come upto a cluster size of a few 10 nanometers [18]. The size of them can be at maximum a few 10 nanometers. In contrast to the nanogranular films, nanoclusters do not require a matrix material in its formation. Therefore, there is a direct control over the size of the nanoclusters in comparison to the nanogranular films. This flexibility in size control offer a wide variety of applications arising from the modification of geometrical, optical, electronic and magnetic properties of the material compared to its bulk counterpart [19]. Clusters are sourced using different methods. They are seeded superzonic nozzle source, gas aggregation cluster source, laser vaporization cluster source, sputtering source and liquid metal ion source [20]. All these methods basically condense the metal vapours or allow the vapours to collide with each other in a pressurized inert gas atmosphere and these are generally called as the physical vapour deposition methods. There are sevaral other methods such as chemical vapour deposition, liquid phase deposition technique such as spin coating, electrochemical deposition, etc. The nanocluster deposition of Ag in the present research is based on the modified form of gas aggregation technique. The aggregated nanoclusters are flown on to the substrate kept in a chamber at a lower pressure through the nozzle.

Electron transport in nanocluster films has been an interesting topic considering the tunability of the cluster size, distribution and inter cluster separation over the surface [21–28]. A definite control of size and structure of nanoclusters makes it to tune the electron transport very efficiently in order to use in electronic devices. Further, nanoclusters are potential materials for single electron transistors which can replace semiconductor electronic technology. Hall effect measurements in the cluster films have shown strange scaling behaviour. According to the expected hall effect mechanisms the scaling law can give an exponent between 1 and 2. However, nanocluster films have shown the exponent far greater than this. Therefore, nanocluster has to be further understood in terms of electron transport.

## 1.6 Magnetic tunnel junctions

Over the last three decades, Magnetic Tunnel Junction (MTJ) has been an intensive topic of research because of its applications in magnetic field sensor, random access memory, read head for hard disk drive etc. [29,30]. MTJ is a sandwich of a thin insulator layer separated by two ferromagnetic layers. The resistance across this system varies depending on the relative spin orientation of the ferromagnetic layers, which can be controlled with external magnetic field. Variation of resistance is due to the spin dependent scattering of carrier electrons. In the absence of external field, spins of ferromagnetic layers on either sides of spacer layer are antiparallel and thus resistance is high, whereas, when a field is applied all the spins are oriented along that direction and scattering is less, i.e. less resistance. This

kind of systems can be manipulated either for a linear response or a bistable state switching according to the demands of application. With the amorphous  $Al_2O_3$  junction layer a tunneling magnetoresistance (TMR) of up to 70% was observed. Later, a TMR of a few thousand percentage was predicted by taking crystalline MgO as insulating layer: Currently, a TMR of about 600 % was observed for this system at room temperature and as high as 1100 % at 4.2 K [31]. However, the fabrication techniques are quite expensive with the requirements of material selective ion etching. Optimization and manipulation of these properties are still under serious consideration.

#### 1.7 Motivation

Electron transport in nanostructures is a quite fascinating area as the tunable nature of these structures are useful in various device applications. Though, the physics behind the transport in these systems is diverse, the research carried out in this area is very less. An enormous amount of research problems are open to research in these structures which can bring in new multi-functional nanomaterials based devices. In such a scenario, it is a humble effort to understand the physics behind the electron transport in metallic nanostructures of very thin form in order to utilize them in device applications.

#### 1.8 Plan of the thesis

This thesis is organized to six chapters. First chapter -this chapter- aims at giving the foundation to the research works detailed in this thesis. Starting from materials in general, this chapter describes the class of materials called nanomaterials, classifies them according to the dimension of the system and dimension of constituent elements of the system. Further, this chapter discusses over the two dimensional nanostructures (nanomaterials) containing constituent elements of zero dimension and the electron transport properties pertaining to them. Finally, a brief overview of the nanamaterials discussed in this thesis such as nanogranular films, nanocluster films and magnetic tunnel junctions have been established.

Experimental techniques utilized to achieve the experimental results have been elaborated in chapter 2. This chapter constitutes three sections; sample preparation, characterization and analysis. First section describes the different experimental techniques conducted to prepare FePt nanogranular films, Ag nanocluster films and magnetic tunnel junctions and they are magnetron sputtering, inert gas expansion based nanocluster deposition system, e-beam lithography and optical lithography. In the second section, i.e., characterization, different methods to understand the morphology and transport mechanism of the samples have been elaborated. The techniques used in this regard are transmission electron microscopy (TEM), scanning electron microscopy (SEM) and resistivity and hall measurements using four probe and two probe methods in cryogenic magnetic probe stations and vibration sample magnetometry using physical property measurement system. In the last section, the methods used for analysis have been briefly discussed. The program built for curve fitting based on the gradient search

algorithm has been explained in this section.

Electron transport in FePt-C nanogranular films is explained in chapter 3. Samples are prepared by two different ways. They are co-sputtering and sputtering FePt and C serially at a heated substrate holder. Intergranular distance of the samples has been modified by varying sputtering power and substrate temperature. TEM image shows the morphology of 6 different samples. Sample preparation and TEM were carried out from NIMS Japan. Resistivity of all the films have been measured between 6 K to 300 K. The result shows different conduction mechanisms such as Mott variable range hopping and Efros-Shklovskii variable range hopping. A metal insulator transition was observed at around 21 K and the hopping mechanisms were active only above 25 K. Further, resistivity measurement at a saturated magnetic field was conducted. The result shows that variation in conductivity at low temperature is due to intergranular interaction. The chapter concludes possible engineering and use of these films as spin channel in field effect transistors as the conductivity is tunable.

Chapter 4 deals with the electron transport in Ag nanocluster films. The films have been prepared by using nanocluster deposition system in which clusters are formed by gas aggregation technique. A set of films have been prepared by varying the deposition time such that the films are in between continuous and discontinuous forms. SEM image shows that the clusters form to interconnected chains as the deposition time reduces. Resistivity measurement shows metallic resistivity. As the deposition time reduces, an upturn in resistivity is emerged and the minimum in resistivity moves up in temperature. Resistivity above 45 K fits well to the modified Bloch-Gruneisen equation (modified to include scattering from carrier-carrier interaction). In the low temperature region an additional  $\sqrt{T}$  de-

pendence in resistivity matches with the data. This is due to electron - electron interaction in these systems. The additional term is found dominating as the deposition time reduces. Hall effect measurement in one of the films show that hall coefficient does not change much but it increases towards low temperature and saturates.

A simple and cost effective technique of fabricating magnetic tunnel junction (CoFe/MgO/CoFe polycrystalline trilayer) using optical lithography has been presented in chapter 5. Growth of MgO (001) underlayer over thermally oxidized silicon has been studied. Uni-directional pinning of reference layer has been optimized by the study of exchange bias varying the thickness of IrMn/FeCo bilayer. Further, microfabrication steps have been explained. Current density - Voltage curves have been fitted to Simmon's relation for tunneling current and obtained barrier potential and thickness. Magnetoresistance measurement on microfabricated tunnel junction revealed a TMR of upto 7 %. A circuit has been designed to utilize these MTJs for sensing low magnetic fields by keeping two MTJs as components of bridge circuit and amplifying the output using op-amp. The MTJs were microfabricated only using optical lithography.

Chapter 6 concludes the results obtained in the research work and presents future perspectives that can be carried out further in this research. A large number of research problems are open to understand the transport in nanostructures by controlling the size and dimensions and make use of them in modern technology.

### References

- [1] J. Z. Zhang, Z.-l. Wang, J. Liu, S. Chen, and G.-y. Liu, *Self Assembled Nanostructures*. Nanostructure Science and Technology, New York: Kluwer Academic Publishers, 2004.
- [2] C. Niitzenadel, A. Ziittel, D. Chartouni, G. Schmid, and L. Schlapbach, *Eur. Phys. J. DS*, Vol. 245, 2000.
- [3] J. Gribbin and M. Gribbin, Richard Feynman: A Life in Science. 1997.
- [4] N. A. Mahmood Aliofkhazraei, *Two-dimensional Nanostructures*. Taylor & Francis, 2012.
- [5] V. V. Pokropivny and V. V. Skorokhod, *Materials Science and Engineering: C*, vol. 27, pp. 990–993, 2007.
- [6] L. K. Foong, M. M. Foroughi, A. F. Mirhosseini, M. Safaei, S. Jahani, M. Mostafavi, N. Ebrahimpoor, M. Sharifi, R. S. Varma, and M. Khatami, RSC Adv., vol. 10, pp. 15430–15460, 2020.
- [7] G. Cao, Nanostructures & nanomaterials: synthesis, properties & applications. London: Imperial College Press, reprinted ed., 2006.
- [8] D. K. Ferry, S. M. Goodnick, and J. Bird, *Transport in Nanostructures*. Cambridge University Press, 2 ed., 2009.
- [9] A. Glatz, ed., Theory of quantum transport in metallic and hybrid nanostructures: proceedings of the NATO Advanced Research Workshop on Theory of Quantum Transport in Metallic and Hybrid Nanostructures, St. Petersburg, Russia, 25 29

- *August* 2003. No. 230 in NATO science series Series 2, Mathematics, physics and chemistry, Dordrecht: Springer, 2006.
- [10] S. A. Majetich, J. H. Scott, E. M. Kirkpatrick, K. Chowdary, K. Gallagher, and M. E. McHenry, *Nanostructured Materials*, vol. 9, pp. 291–300, 1997.
- [11] D. Sellmyer, ed., *Advanced magnetic nanostructures*. New York, NY: Springer, 2006.
- [12] I. S. Beloborodov, A. V. Lopatin, V. M. Vinokur, and K. B. Efetov, *Rev. Mod. Phys.*, vol. 79, pp. 469–518, 2007.
- [13] C. Grimaldi, *Phys. Rev. B*, vol. 89, p. 214201, 2014.
- [14] M. Reghu, K. Vakiparta, C. O. Yoon, Y. Cao, D. Moses, and A. J. Heeger, *Synthetic Metals*, vol. 65, pp. 167–171, 1994.
- [15] V. V. Bazarov, V. Y. Petukhov, V. A. Zhikharev, and I. B. Khaibullin, *MRS Online Proceedings Library Archive*, vol. 388, 1995.
- [16] S. Bose, R. Banerjee, A. Genc, P. Raychaudhuri, H. L. Fraser, and P. Ayyub, *J. Phys.: Condens. Matter*, vol. 18, pp. 4553–4566, 2006.
- [17] S. Sergeenkov, L. Cichetto, J. C. C. A. Diaz, W. B. Bastos, E. Longo, and F. M. Araújo-Moreira, *Journal of Physics and Chemistry of Solids*, vol. 98, pp. 38–42, 2016.
- [18] T. Lee, J. Liu, N.-P. Chen, R. P. Andres, D. B. Janes, and R. Reifenberger, J. Nanopart. Res., Vol. 2, p. 345, 2000.

- [19] C. A. Grimes, E. C. Dickey, and M. V. Pishko, eds., *Encyclopedia of sensors. Vol.* 6: *Me N.* Stevenson Ranch, Calif: ASP, American Scientific Publ, 2006.
- [20] W. A. de Heer, Rev. Mod. Phys., vol. 65, pp. 611–676, 1993.
- [21] L. V. Lutsev, S. V. Yakovlev, and V. I. Siklitskii, *Phys. Solid State*, vol. 42, pp. 1139–1146, 2000.
- [22] S. G. Praveen, C. Bansal, and D. J. Nagar, *Scientific Reports*, vol. 9, p. 7513, 2019.
- [23] C. Bansal, S. G. Praveen, J. T. T. Kumaran, and A. Chatterjee, *Scientific Reports*, vol. 5, p. 7685, 2015.
- [24] T. Abraham and C. Bansal, J. Phys. Commun., vol. 1, p. 015008, 2017.
- [25] J. Joseph, J. Wang, B. S. D. C. S. Varaprasad, Y. K. Takahashi, K. Hono, and A. Rajanikanth, *Mater. Res. Express*, vol. 7, p. 046405, 2020.
- [26] T. Abraham, C. Bansal, J. T. T. Kumaran, and A. Chatterjee, *Journal of Applied Physics*, vol. 111, p. 104318, 2012.
- [27] V. I. Kozub, V. M. Kozhevin, D. A. Yavsin, and S. A. Gurevich, *Jetp Lett.*, vol. 81, pp. 226–230, 2005.
- [28] E. Barborini, G. Corbelli, G. Bertolini, P. Repetto, M. Leccardi, S. Vinati, and P. Milani, *New J. Phys.*, vol. 12, p. 073001, 2010.
- [29] S. Z. Peng, Y. Zhang, M. X. Wang, Y. G. Zhang, and W. Zhao, "Magnetic Tunnel Junctions for Spintronics: Principles and Applications," in Wiley Encyclopedia of Electrical and Electronics Engineering, pp. 1–16, American Cancer Society, 2014.

- [30] J.-G. J. Zhu and C. Park, *Materials Today*, vol. 9, pp. 36–45, 2006.
- [31] S. Ikeda, J. Hayakawa, Y. Ashizawa, Y. M. Lee, K. Miura, H. Hasegawa, M. Tsunoda, F. Matsukura, and H. Ohno, Appl. Phys. Lett., vol. 93, p. 082508, 2008.

# Chapter 2

# **Experimental Techniques**

In this chapter, different experimental methods and instruments used to accomplish this work are explained in detail. Thin film deposition and characterization of the samples were done using magnetron sputtering system, nanocluster deposition system, electron beam lithography, photolithography, transmission electron microscope, scanning electron microscope, cryogenic probe station, cryogenic magnetic probe station and physical property measurement system. Finally, the analysis tools have been briefly discussed and the algorithm of curve fitting coding has been explained.

### 2.1 Sample preparation

The integral part of thin film preparation is sample cleaning. The substrates were cleaned with ultra-sonication in Acetone, iso-propyl alcohol (IPA) and distilled water for 5 minutes each and then blown using Nitrogen gas. The reason behind such a sequential sonication is that Acetone dissolves organic impurities,

IPA removes inorganic impurities and water is the universal solvent. Utmost care has been taken to avoid any contamination on the surface of the substrate. FePt-C nanogranular films were deposited by sputtering and nanoclusters were produced using nanocluster deposition system which works based on the nucleation of sputtered atoms with inert gas aggregation.

### 2.1.1 Sputtering

Sputtering is the removal of atoms from the surface of the required material by bombarding incident atoms or ions onto the material. The sputtered atoms are deposited on substrates facing the target. A schematic of sputtering chamber is shown in figure 2.1. The advantage of sputtering over evaporation methods is the control of deposition rate which improves the quality of the film. The most significant parameter in Sputtering is Sputtering yield which is defined as the number of atoms ejected per incident atom or ion [1]. In order to emit atoms from the surface of the material, there exists a minimum energy which is called as sputtering threshold and above this energy, sputtering yield increases proportionally until it reaches a broad maximum beyond which the yield is reduced. Sputtering yield varies from material to material. It varies with the angle incident particle makes with the normal of the target surface, target crystallinity, target temperature, surface topography, electric/magnetic field at the surface and gas pressure.

Inert gases are generally used for sputtering. A continuous flow of inert gas is set to flush out impurities desorbed from the walls during sputtering. Self sustained glow discharge can be obtained when a dc voltage is applied between electrodes at gas pressure from about a few mTorr to 10 Torr. At this gas pressure,

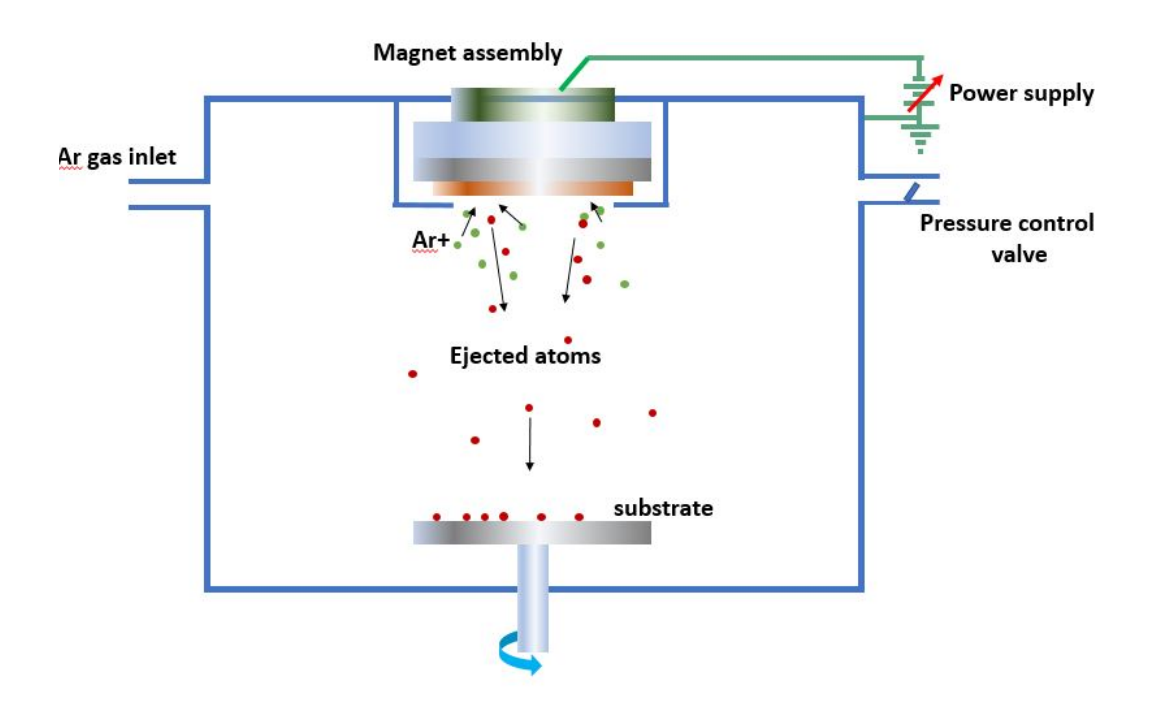


*Figure* **2.1**: *A schematic diagram of sputtering chamber.* 

as the voltage is increased from zero, initially a current of the order of pico Ampere is measured because of the ionization of gas due to cosmic radiation. As the voltage is increased further, gas collision increases ionization and current and this region is called Townsend discharge. When the voltage is increased again, the current increases rapidly and voltage reduces and glow discharge is seen. The minimum voltage required to produce glow discharge is called 'cathode drop' which is unique for every gas-cathode combination. If either power or gas pressure is increased further, cathode glow increases in size with cathode current and voltage remains constant until the glow covers the cathode. Further increase in power or gas pressure increases the voltage and current density and this region (called as 'abnormal glow') is used for film deposition [2]. A magnet on the back

of the target can direct ions towards the target to increase sputtering yield. This method is called as 'magnetron sputtering'.

Insulators cannot be sputtered using direct current plasma discharge (DC sputtering), as positive ions are accumulated on the surface which stops further ion bombardment. Therefore, a radio frequency alternating current is supplied (RF sputtering). Positive ions accumulated on the target in one half cycle is discharged by electron bombardment in the other half cycle. Therefore, sputtering happens only in half of the cycle which reduces the sputter yield in RF sputtering.

### 2.1.2 Nanocluster deposition

Nanocluster films produced in this work are using Oxford Applied Research (UK) make Nanocluster deposition system which functions by the method of inert gas expansion. A schematic and an image of the nanocluster deposition system are shown in figure 2.2 and figure 2.3 respectively.

The deposition system consists of two chambers; gas aggregation chamber (A) and deposition chamber (B) which are separated by a manually controlled valve and a couple of apertures. The chambers are maintained at differential pressure by evacuating the aggregation and deposition chambers 500 l/s (C) and 1000 l/s (D) respectively. This is achieved with two Pfeiffer make turbo pumps having respective capacity and supported by Varian rotary scroll pump. Magnetron sputtering source (E) is kept at the back end of the aggregation chamber and inert gas is fed into it for sputtering. Water cooling has been fed to both the turbo pumps and magnetron to reduce heating. The higher pressure in the aggregation chamber helps nanocluster film formation in two ways. First, in the gas aggregation

chamber atoms are ejected out from the target by dc sputtering at a higher pressure and this leads higher sputter yield and frequent collision between sputtered atoms forming clusters and second, these clusters are directed through a small hole to the deposition chamber since the deposition chamber is at a lower pressure. Clusters are landed on the substrates over the substrate holder (F) kept on the way of the clusters carried by the gas flow through the deposition chamber. If the pressure has to be further raised in aggregation chamber just to enhance the flow of cluster beams to deposition chamber there is an option to supply Helium in a controlled flow rate into the aggregation chamber.

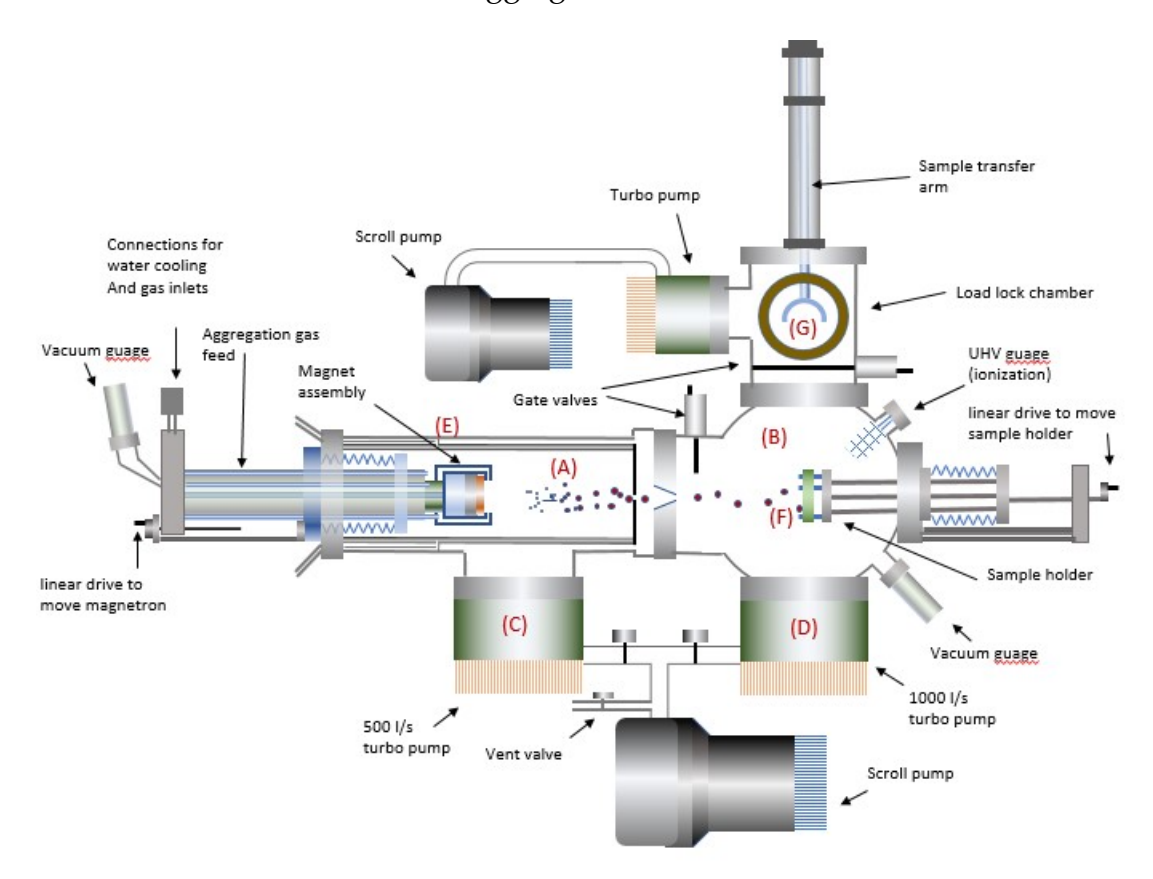


Figure 2.2: Schematic diagram of Nanocluster depostion system.

The valve between two chambers consists of two apertures to shape the cluster beams so that it is focused on the substrate. Length of the aggregation chamber decides average cluster size as the collision time increases with the length. Aggregation length can be adjusted between 6.5 cm to 20.5 cm. Substrate holder can be moved in the direction of cluster beam and substrate rotation is enabled for uniform film deposition. The substrate can be heated using strip heater or give bias so that the clusters can sit on the substrate properly.

The equipment consists of a load lock chamber (G) with sample transfer arms to avoid contamination of main chamber by frequent exposure to atmosphere.



Figure 2.3: An image of nanocluster deposition system (Nanodep60).

### 2.1.3 Electron beam lithography

Photomasks to pattern the magnetic tunnel junctions have been fabricated using electron-beam lithography system shown (CABL 9000C) within the clean room (Class 100) of Center for Nanotechnology, University of Hyderabad as shown in figure 2.4. By using e-beam lithography, electron beam can be properly focussed on the suitable resist to produce a pattern resolution of upto a few nanometers. For commonly used resist, such as PMMA, the polymer chain breaks while the electron energetically incident on the resist which becomes soluble in certain chemical called developer.

Electron beam can be exposed to a maximum area of 2 mm and this is called as field. There are different dots options. As the number of dots increases the scanning takes more time. The resolution of the pattern is determined by the ratio of field to dot. E-beam lithography over a bigger area is done by dividing the total area into different fields and moving the substrate after the exposure of each field. The substrate has to be moved precisely, so that the fields are attached precisely. This is called as stitching of fields. Two different ways the electron beam can be scanned over the resist; raster scan and vector scan. In raster, the beam pass through all the dots in the field horizontally or vertically and exposes only to the required dots, whereas, in vector scan, the e-beam passes through the partitioned features and hops to the next by skipping the unwanted region. Hence, the time is saved in vector scan.

Though, the wavelength of electrons are about 0.005 nm for a 50 keV e-beam exposure, the resolution is larger due to forward and backward scattering. Forward scattering widens the beam width within the resist, whereas electrons scat-



*Figure 2.4:* Showing the electron beam lithography system used to make MTJ photomasks.

tering from the substrate (back scattering electrons) can scatter at random direction and thus to a wider area. Thus, the resolution of the pattern can be affected by these scattering and this is called as proximity effect. At the center of the square feature, the exposure occurs due to scattering from all around but at an edge the exposure is lesser and at a corner it is further reduced since the scattering is from about 1/4th of the surrounding regions. Therefore, proximity effect can be resolved by exposing different areas at different dose. This is done by converting the pattern design into different layers and exposing at different dose using a software. The dose and variation in the dose depends on the resist and the substrate.

The dose is initially estimated by exposing e-beam through a test design of

parallel lines with feature size lesser than the smallest feature size of the original design to be transferred. A matrix of the test designs are exposed at a set of different doses and observed after developing to choose the the best one.

For the mask fabrication of MTJs, The PMMA 495B resist was spin coated over the mask plate at 4500 rpm for 1 minute. This is then heated at  $150^{0}C$  for 3 minutes. After cooling the mask is transferred to the e-beam sample stage. The field size was 60  $\mu$ m and dots are 60000. The scanning was by vector method and the beam width of e-beam was 100 pA. The optimized dose was 0.11  $\mu$ sec/dot. After e-beam exposure, the mask is developed in MiBK developer for 90 seconds and stopped developing by keeping it in 2-propanol for 1 minute. The exposed resist was then washes off and the required pattern is obtained.

### 2.1.4 Optical lithography

Magnetic tunnel junctions have been patterned using optical lithography. Optical lithography is a technique of patterning thin films upto a few hundred nanometer resolution. This is achieved by directing monochromatic UV-ray on to the photoresist (light sensitive polymer) coated substrate through a photomask. The monochromatic light passes through the transparent regions of the photomask and incident on the photoresist coated wafer. The UV-ray either harden or soften the photoresist . The softer portion of the photoresist is removed by treating in a chemical called developer. In the process of MTJ fabrication, the different device layers have been sputter deposited over the patterned substrate. After the deposition, the resist is washed off in a chemical and this process is called as lift-off since the film deposited over the resist is lifted off during this step.

The magnetic tunnel junctions were patterned in SUSS MicroTech make MJB4 mask aligner (figure 2.5) within the clean room of Center for Nanotechnology, University of Hyderabad. In the mask aligner, the substrate is in direct contact with the mask before the exposure of UV-ray which gives a resolution of about 1  $\mu$ m.

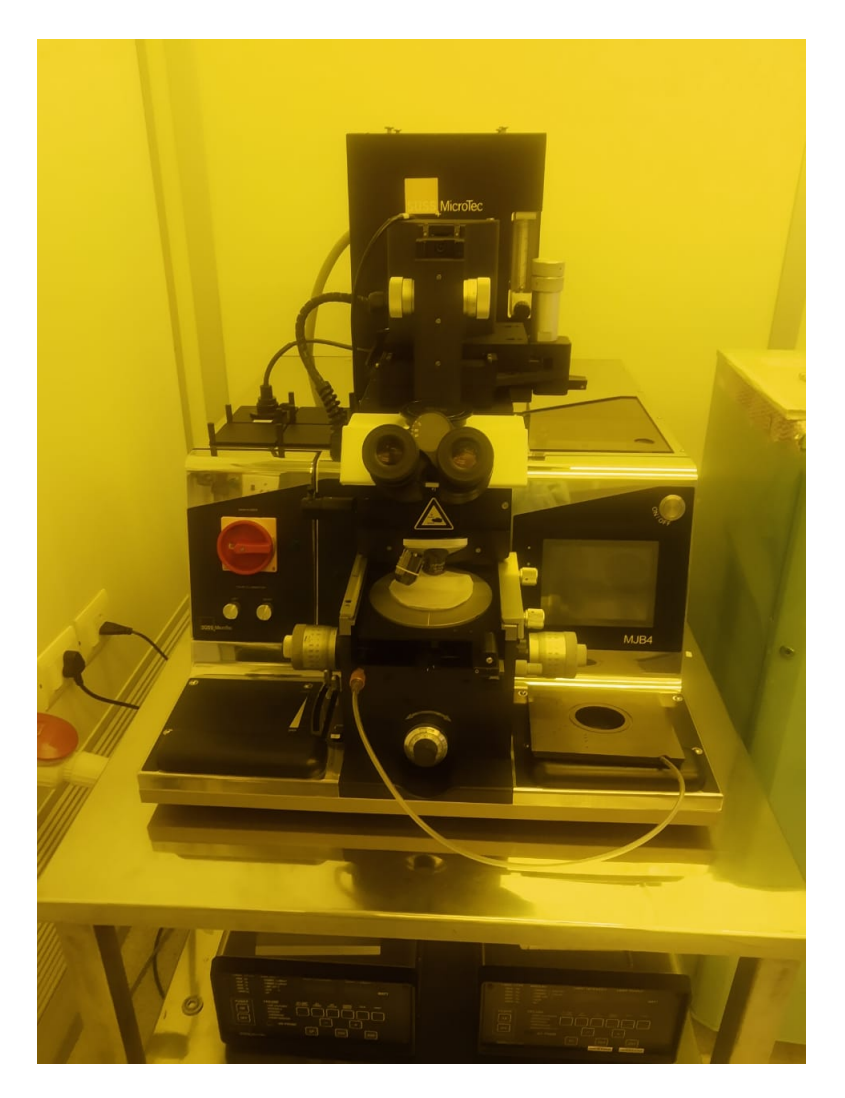


*Figure 2.5: Shows the photolithography unit used to pattern the MTJ.* 

### 2.2 Characterization

### 2.2.1 Transmission electron eicroscopy

Nanoscale features of the materials can be best observed by using transmission electron microscope. Basic principle of TEM is imaging electron beams transmitted through a thin section of the sample on a photographic sheet. Crystal structure of materials can also be identified with it as the resolution of the images can be obtained upto atomic scales [3]. A schematic of transmission electron microscope is shown in figure 2.6. Operation of TEM is illustrated as follows. Electron beam ejected from the source is focused and adjusted using metal apertures and electromagnetic lens onto the sample. Thickness of the sample should be 100 nm or less so that the electron should transmit through the sample. Transmission of electrons depend on factors such as composition and density. More electrons pass through the porous part of the material, whereas less through the denser part of the material. Transmitted electron beam is focused and magnified using electromagnetic lenses and is incident on a phosphour sheet to convert into image. Crystal structure of materials can also be acquired by transmitting parallel electron beams through the sample using condenser lens. The resolution of TEM can be further increased by accelerating the electron beams applying voltage as the following equation.

$$\lambda(nm) \approx \frac{1.23}{\sqrt{V}} \tag{2.1}$$

Images can be captured in bright field and dark field mode. In the bright field mode, the aperture behind the specimen allows the electron beam transmitted directly. Hence, the denser area of the film is darkened. In the dark field mode,

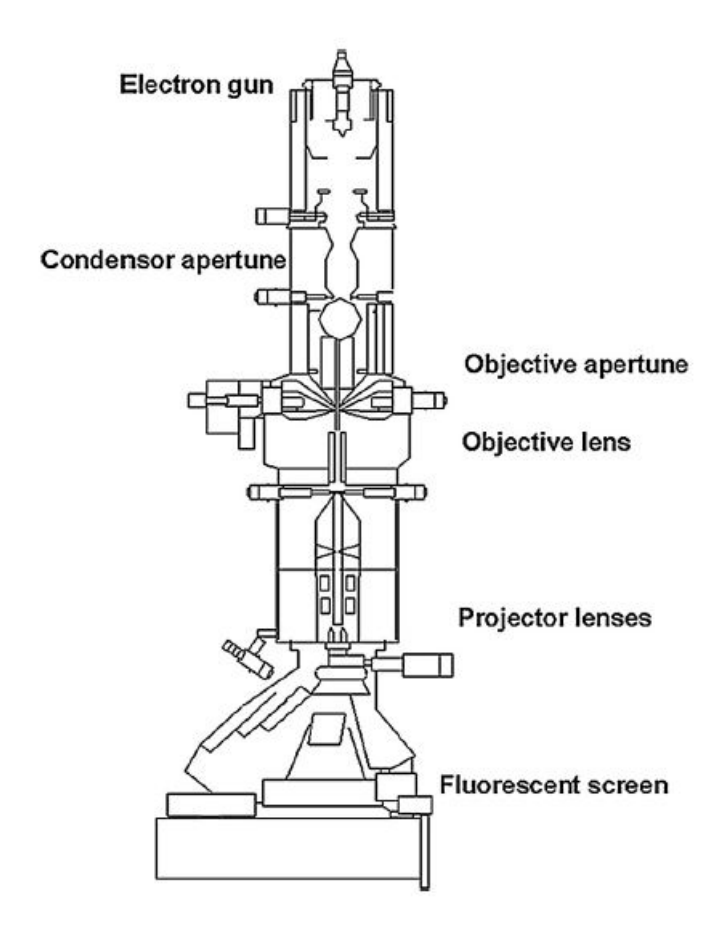


Figure 2.6: Schematic of a transmission electron microscope.

only the diffracted electrons pass through the aperture giving rise to a set of bright spots. These are the different lattice planes in the reciprocal space. Measuring the distance from each diffracted spot to the direct spot, the crystal structure is calculated.

### 2.2.2 Scanning electron microscopy

Surface morphology of Ag nanocluster films were captured using Carl Zeiss ultra55 field emission scanning electron microscope (SEM). In contrast to the transmitted beam used to image in TEM, scattered electrons are used for imaging and composition analysis in SEM. A probe scans the small portion of the image at a time and the probe move serially in a rectangular region of the sample and integrate the total image. A resolution of upto a few nm can be obtained using SEM. Generally, there are two different ways electron beams are produced; thermionic emission by heating the target and field emission by applying electric field. A better resolution is obtained with a field emission gun. A schematic of SEM is shown in figure 2.7.

Electron beam emitted from the gun is focussed using two condenser lenses to reduce the beam width to a spot size of 1 nm. Condenser lenses are electromagnetic coils. Magnetic field generated from the current carrying coil controls the beam width. Scanning coils arranged at the objective lens moves the lens in linear or raster fashion and collects the image. Another set of electromagnetic coil arrangement called stigmator is used to correct the irregularities in the x-y deflection and to make the beam perfectly round. Electrons in the beam impinging on the sample loose energy inelastically to the atomic electrons and lattice. The scattered primary electrons spread into a teardrop shaped volume with a multitude of electron excitation. In addition to that, x-ray, light, heat and specimen currents are produced. They are detected using different techniques. Other than the primary electrons, electrons are ejected from the surface of the material and they are called as secondary electrons. These low energy signals are widely used to capture the

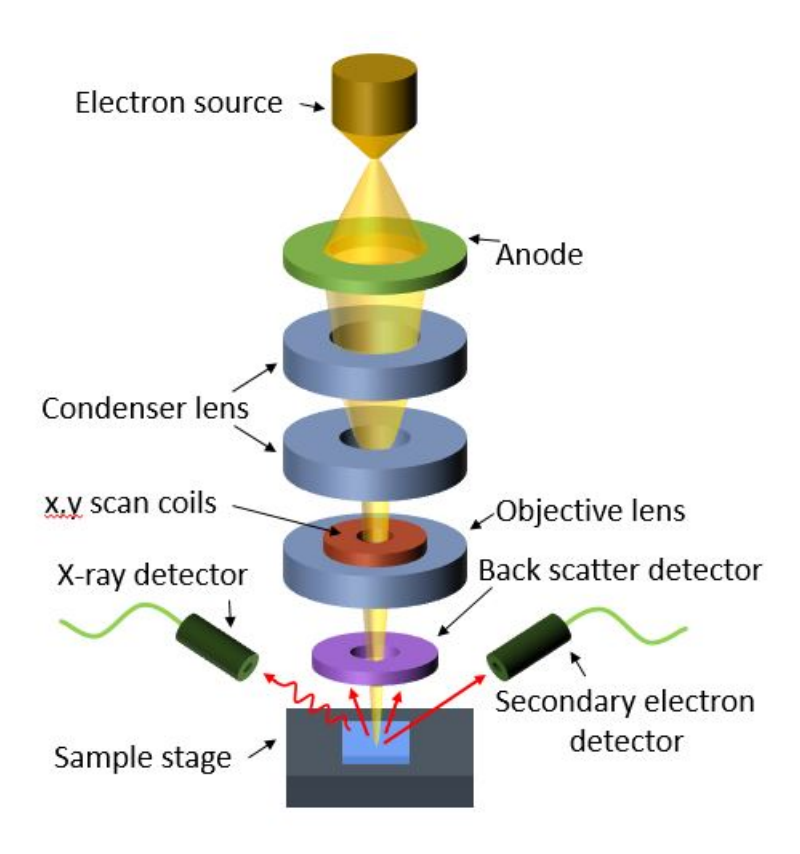


*Figure 2.7: Schematic image of Scanning electron microscope.* 

surface image. In the slope surfaces or the edges, more secondary electrons are produced at a specific area compared to the same in a horizontal surface. In this mode, 3d images can be captured using secondary electrons. An amount of electrons are scattered right back, called as back scattering electrons, with the same energy. Back scattering electrons are proportional to the atomic number of the specimen, even if this is not so exact. Though these electrons are not sufficient for elemental identification, a contrast can be obtained when there is a wide difference in atomic number. Further, x-ray characteristics of the sample is produced from the specimen surface, which is used for elemental identification and concentration

of them by finding the energy and amount of corresponding x-rays respectively.

### 2.2.3 Cryogenic probe station

Low temperature resistivity measurements down to 6K were done in Lakeshore-4K cryogenic probe station along with the measuring instruments such as Keithley 6221 current source, Keithley 2700 data acquisition system, Keithley 2635 source measurement system and Keithley 181 nanovoltmeter.

The probe station consists of a vacuum chamber having sample stage with a heat shield around it to avoid thermal radiation from the outside wall. The chamber is evacuated upto  $5\times10^{-4}$  Torr by turbo pump prior to cooling. Sumitomo closed cycle refrigerator (CCR) is used to cool the sample stage down to 6 K. Working principle of this CCR is based on Gifford-McMohan (GM) refrigeration [4]. The GM cycle is shown in figure 2.8.

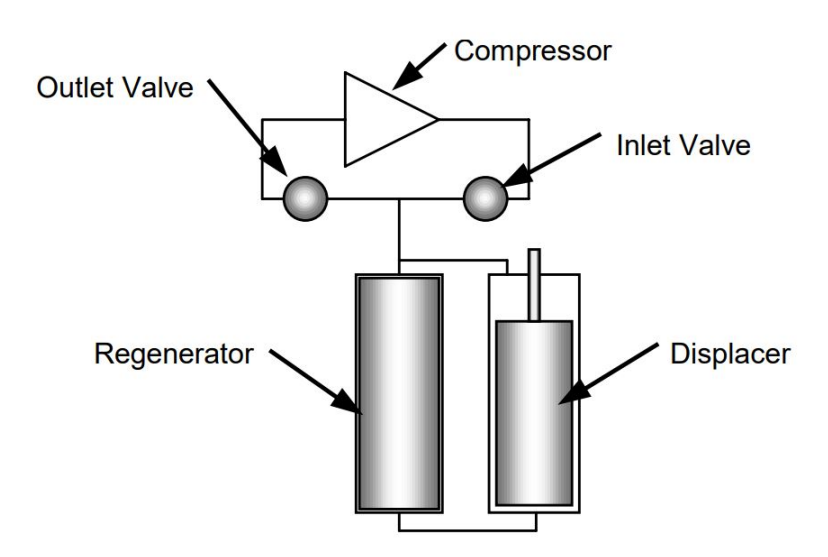


Figure 2.8: Schematic diagram of Gifford Mcmahon refrigeration cycle. Courtesy: Sumitomo.

The refrigerator consists of a displacer, regenerator, gas compressor and inlet and outlet valves. The displacer is kept in a cylinder and it is three quarter of the cylinder. The displacer can be freely moved in the cylinder but the lateral surface is sealed so that gas cannot translate across it. Pressure in the system is controlled by the inlet and outlet valves. The valves are connected with a rotary drive mechanism and is syncronized with the position of the displacer. The regenerator cools the gas moving down to cold space and warm the gas flowing upward from the cold space. Operation of the refrigerator can be divided into four stages.

- 1. **Pressure build-up:** Displacer moves down, inlet valve opens and outlet valve closes. Fluid is filled in the regenerator and the space above the displacer. Pressure is increased.
- 2. **Intake stroke:** The displacer moves up. This displaces the gas above the displacer to below the displacer through the regenerator. While moving from top to bottom of regenerator, the gas is cooled, which reduces the pressure. More gas enters through the inlet to maintain the pressure.
- 3. Pressure release and expansion: Inlet valve closes and outlet valve opens with the displacer remains at the top. Fluid passes out through outlet and pressure decreases. The drop in pressure causes the reduction in temperature at the bottom of the displacer.
- 4. Exhaust stroke: The displacer moves to bottom. This displaces fluid from bottom to top of the displacer through regenerator. the fluid flowing to top of the regenerator heats the cold fluid to ambient temperature for the further cycle.



**Figure 2.9:** Showing the cryogenic probe station along with its accessories such as temperature controller, microscope unit, vacuum pump and closed cycle refrigerator.

Heated CCR is cooled using a locally made chiller unit. The probe station can accomodate a maximum of 4 probes. Temperature of the sample stage can be controlled using a heater and associated Lakeshore 336 temperature controller in 2 modes; PID control and auto-tune. The probe stations along with the assessories for controlled cooling of sample stage is shown in figure 2.9. Probe station can accommodate a maximum of 6 probes and as many wire contacts. Two probe resistivity measurements have been done in this system using Keithley 2635 source measurement system. The measurements have been conducted using labview automation. The system is cooled to below 6 K prior to measurement. The measurement was taken after the temperature of the sample stages reaches to the set temperature with a standard deviation of < 0.01 K. IV characteristics of the sam-

ples are taken at different set temperatures. The resistance was calculated from the slope of IV data.

### 2.2.4 Cryogenic magnetic probe station

Microxact make cryogenic magnetic probe station is equipped with in plane magnetic field upto 0.5 Tesla produced by electromagnet, out of plane magnetic field upto 3.5 Tesla by superconducting magnet and sample cooling facility using Helium refrigerent CCR of Sumitomo. The probe station is shown in figure 2.10.

Prior to cooling, the chamber is evacuated using Pfeiffer make turbo Pump and oil pump. The maximum speed of the Turbo pump is 90000 rotation per minute. A pressure of  $2\times10^{-5}$  Torr is achieved with these units. The sample stage and superconducting magnet are cooled using two Sumitomo make CCRs. This is to cool enormous mass which takes 13 hrs to cool the magnet to the working temperature of superconducting magnet, i.e. below 9 K. The cooling line from cryohead to the sample stage and the magnet are covered using Copper sheet which works as thermal shield from the outer wall. The superconducting magnet sits vertically around the sample holder. It is having two rectangular holes in the middle of the lateral surfaces. This is to pass the probes to the sample stage. There are options for six probes. The sample stage is attached on a thermal switch so that the stage can be isolated from the cooling line to do measurement at various temperatures keeping the superconducting magnet at the lowest temperature. The electromagnet is attached outside the chamber setting the center of the poles at the sample stage in order to achieve maximum field at the sample. A couple of crains are set to put down or lift up and position. The electromagnet and CCRs are cooled using



*Figure 2.10:* showing cryogenic magnetic probe station.

a Fluid Chillers Inc. (USA) make chiller unit.

Different labview programs have been set to measure Hall effect and magnetoresistance of the films interfacing with keithley 6221 current source, Keithley 181 nanovoltmeter and 2700 multimeter.

# 2.2.5 Physical Property Measurement System - Vibrating Sample Magnetometry

Magnetic and magnetoresistance measurements were done in Physical Property Measurement System equipped with a maximum possible applied magnetic field of 9 Tesla and a temperature range between 2 K and 400 K.

The instrument is specially designed to minimize the evaporation of liquid He-

lium as its production is very expensive and evaporation rate is much higher than that of liquid Nitrogen. Sample is inserted into a narrow column which is surrounded by the sample and Helium liquid chamber which cools both the super conducting magnet surrounding the sample. The sample is in a Helium vapour bath and the temperature of the sample is maintained using a heater. The liquid Helium is surrounded by an outer column of liquid Nitrogen. The principle of vibrating sample magnetometry is the following. The sample is vibrated at a frequency of 50 Hz and the oscillating magnetic field due to the sample induces emf in the detection coil surrounding the sample. Since magnetic moment of the sample is a linear function of the induced emf, measured voltage can be easily converted to magnetic moment. This voltage is amplified using a lock-in amplifier taking the reference signal from the oscillating frequency of the sample and this process remove the noice in the signal and make the system capable of measuring smaller moments. Magnetic moment of up to a minimum  $1 \times 10^{-6}$  e. m. u. can be measured in this system.

### 2.3 Analysis

Octave, Matlab and Fortran are the different softwares used to analyse the data. The results were plotted in Origin software.

### 2.3.1 Curve fitting

Most of the data fittings have been carried out using a self made curve fitting program. The program has been made using Gradient-search algorithm. Given a set

of initial parameters and steps, the program calculates chi-square of each parameter and their steps in positive and negative steps. Chi-square of each parameter is then compared with that of step added and substracted. All the parameters are modified to those having minimum chi-square value. The process is repeated until the chi-square minimum of all the parameters settles to the parameters without adding or substracting any steps. These are the fitting parameters. The goodness of fit is checked by calculating adjusted R-square value

$$adj.R - sq. = 1 - \frac{SSR}{SST} \tag{2.2}$$

where, SSR is the sum of the squares of residuals and SSE is the sum of the squares of the data value. The residual is the difference of the data value to the fit value. If the adjusted R-square is above 0.99, the fit is acceptable.

### 2.4 Conclusion

Various techniques used to achieve the results have been explained. Nanocluster, nanogranular films and thin film deposition for MTJs have been fundamentally resourced by using sputtering. Further, to create nanogranular films, multiple targets have been sputtered either by co-sputtering or by sequential sputtering mode at a raised substrate temperature. Nanocluster films were prepared by the method of inert gas expansion. The patterning of MTJs were done using photolithography. Therefore, sputtering, nanocluster deposition, e-beam lithography and photolithography have been explained in the section of sample fabrication. Further, working principle of measurement systems used to characterize such as FESEM, TEM, Probe Station, Cryogenic Magnetic Probe Station and PPMS-VSM

has been elaborated. Finally, the analysis method has been briefly covered.

### References

- [1] M. Ohring, Material Science of Thin Films: Deposition & Structure. New York: Academic Press, 2002.
- [2] G. L. Weissler and R. W. Carlson, eds., *Methods of Experimental Physics*, vol. 14, 1979. New York: Academic Press, 1979.
- [3] C. Tang and Z. Yang, "Transmission Electron Microscopy (TEM)," in *Membrane Characterization*, pp. 145–159, Elsevier, 2017.
- [4] W. E. Gifford, "The Gifford-McMahon Cycle," in Advances in Cryogenic Engineering (K. D. Timmerhaus, ed.), Advances in Cryogenic Engineering, (Boston, MA), pp. 152–159, Springer US, 1966.

# Chapter 3

# Electron Transport in FePt-C nanogranular films

In this chapter, dependence of intergranular distance on electron transport of FePt-C granular films is explained. Sample preparation, microstructure using TEM, M-H measurement, resistivity measurement and its analysis are elaborated.

### 3.1 Introduction

Metal-nonmetal granular films are well-known materials [1] for its tunability in size, separation between granules, dimensions and thereby different conduction mechanisms. Percentage of nonmetal (or metal) in the film decides whether it is metallic or insulating [2]. In the insulating region, since the amount of metal is lesser than insulator, the metal forms to grains and is distributed in the insulating matrix. As we increase the percentage of metal in the insulating region of the

film, granules comes closer and further addition connects the granules making percolation of electrons showing metallic conductivity. The boundary between the metalic and insulating nature of the film is called as percolation threshold. Percolation threshold varies depending on the material compostion. In the metallic regime, at low temperature upturn in resistivity was observed occuring from quantum mechanical phenomena such as weak localization or electron-electron interaction. In the insulating region, electron transport mechanism is explained with tunneling or hopping mechanism [3]. Hopping was first attributed in doped semiconductors and later the same mechanism was observed in many granular systems.

FePt granular films produce huge perpendicular magnetic anisotropy [4] of about  $7 \times 10^{-6}$  J/m<sup>3</sup> arising from the  $L1_0$  ordering. As deposited FePt films are cubic with A1 order. While annealing at above 600 K FePt forms to tetragonal structure with  $L1_0$  ordering as shown in figure 3.1. This particular condition leads the system to be of great interest as the coersive field is about 3 Tesla and the critical grain size for super paramagnetism at room temperature is only 3 nm [5]. The  $L1_0$  ordering decreases with decrease in granular size upto a critical size below which it forms to the cubical structure [6].

A large number of studies on magnetic properties of FePt granular films are available in the literture over the optimization of FePt granular films varying the matrix material [7–10], annealing temperature [11] and substrates to avoid the diffusion of the matrix material and to raise the columnar growth of FePt as a potential magnetic recording media [5,12–16]

A large number of study have been conducted on the magnetism of FePt-C

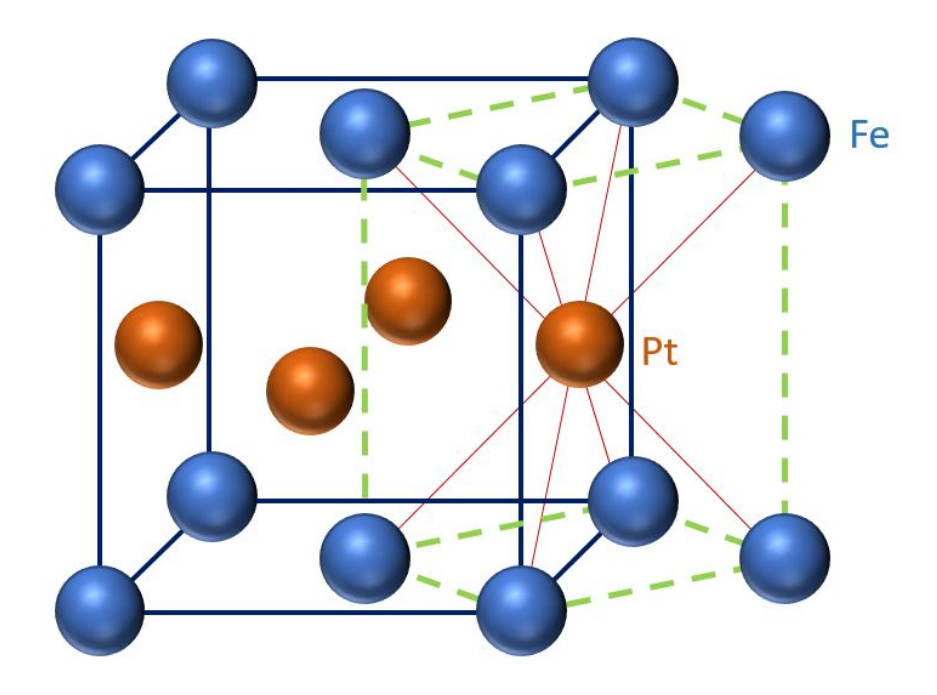


*Figure 3.1: Schematic of*  $L1_0$  *ordering in* FePt.

granular films observing the applications in hard disk media. Whereas, its electrical properties have not been examined enough. Allia et.al. have observed a dip in resistance in FePt-Ag multilayered granular films at about 11 K [17] and below this temperature, a positive magnetoresistance was found at low fields. Recently, Electric field induced spin control in the perpendicular magnetic anisotropy films [18–22] has become an intensive topic of research in spintronics. The advantage of voltage controlled device is the limited power consumption and reduction in joule heating in comparison with the current controlled devices. However, electron transport in such a granular film has not been studied enough to utilize them in device applications.

FePt granular films might be a potential material for electric field controlled electron transport, because it has perpendicular magnetic anisotropy and this is retained upto a granular size as low as 7 nm. It requires only a little amount of electrical energy to align moment from perpendicular to in-plane in comparison with the orientation from in-plane to perpendicular to the plane. Further, electron transport can be conveniently controlled in granular films. Therefore, FePt granular films are suitable candidates for electric field controlled spin channel.

Comparing with different segragant materials such as B, SiO<sub>2</sub>, TiO<sub>2</sub>, etc. for FePt granular films, Carbon is found to be the best, as it retains higher coercivity, smaller grain size distribution and enhanced columnar growth [8]. Hence, FePt-C has been taken as the suitable material for the research.

### 3.2 Sample preparation

FePt-C granular films were prepared by two different methods. One is by cosputtering FePt and C and the other is by sputtering FePt first and then Carbon as capping over it. All the films were deposited at substrate temperatures of 600°C, 750°C or 850°C. The films were grown on MgO (001) substrate which was fount to be the most suitable for the ordering of FePt films [8]. Six different samples were used for this study. The details of samples are tabulated in Table 3.1.

sample name	volume %	Substrate	method of	thickness
	of Carbon	temperature ( ${}^{0}C$ )	preparation	(nm)
FePtC-20850	20	850	Co-sputtering	8
FePtC-20750	20	750	Co-sputtering	8
FePtC-15750	15	750	Co-sputtering	8
FePtC-12600	12.5	600	Co-sputtering	8
FePtCcap-600	_	600	C capping	FePt-8, C-5
FePtCcap-600b	_	600	C capping	FePt-20, C-5

**Table 3.1:** depicts specifications of the samples used for the present study. FePtCcap-600 and FePtCcap-600b are FePt films of 8nm and 20 nm respectively capped with 5 nm of Carbon. All the other samples are of 8 nm thick.

### 3.3 Characterization and analysis

#### 3.3.1 TEM microstrucure

Microstructure of the films were examined using TEM. The image is shown in figure 3.2. Figure 3.2 (a) shows the granules well distributed, whereas in figure 3.2 (b) granules are closer with some of them connected and in figure 3.2 (c) the granules are distributed randomly with many of them connected. Granules are well connected in Figure 3.2 (d), even though they were well distributed. It can be summarized that from figure 3.2(a) to (d) the granular sizes are comparable and the distance between granules gradually decreases. Higher volume % of Carbon (30 %) and annealing temperature (850°C) made the FePtC20850 film well distributed. In figure 3.2 (e) (the image scales of (e) and (f) are four times higher than the other images) granular distance and granular size are higher and in fig-

ure 3.2(f) there are grains of the order of 100 nms and nanograins are distributed in the gap of them. Thus, the image gives the impression that in the films which were prepared by capping Carbon, the granules are bigger and as the thickness of the film is increased, the bigger grains are formed.

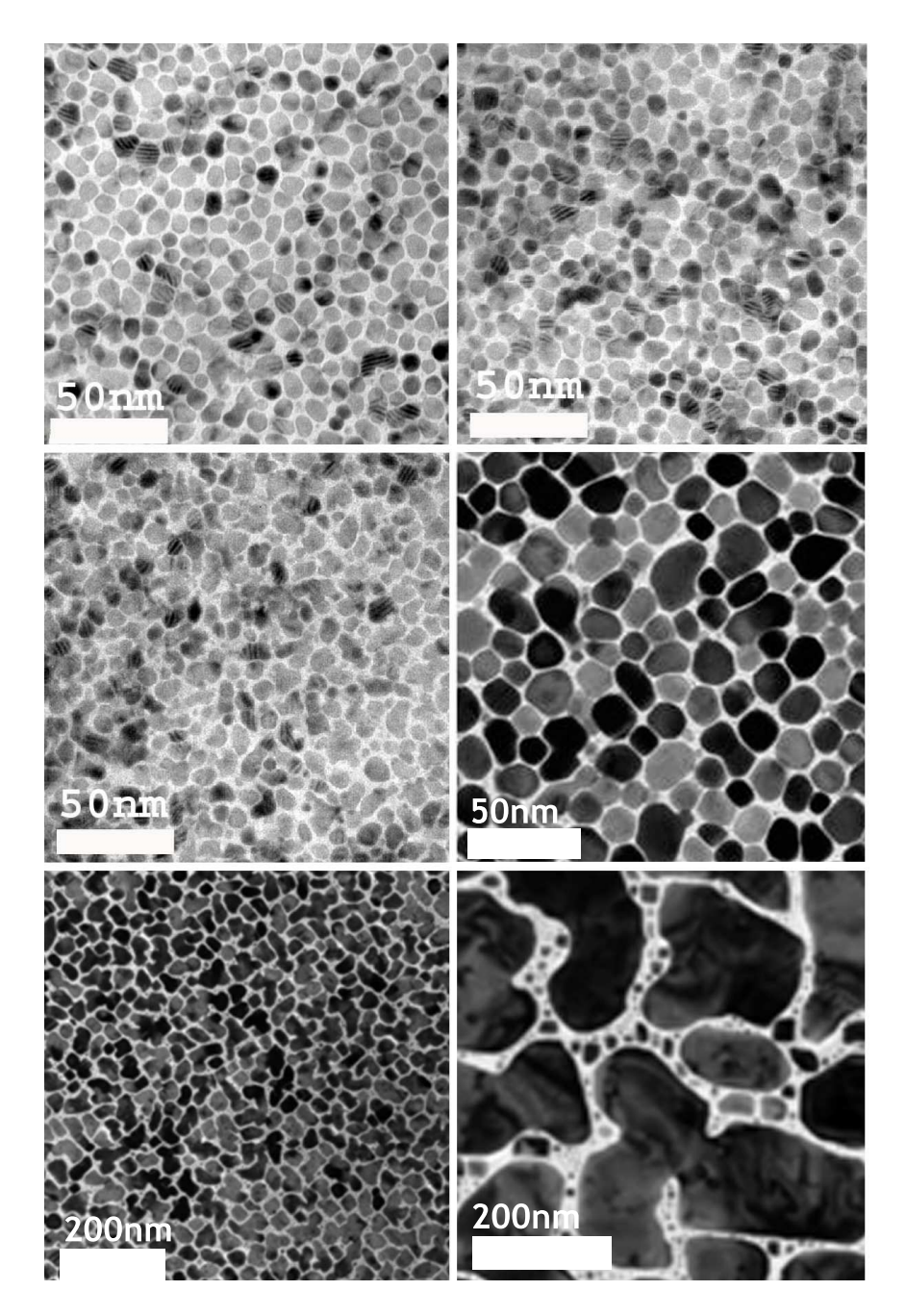


**Figure 3.2:** TEM bright field images of FePt-C granular films having (a) 20 volume % of Carbon annealed at  $850^{\circ}$ C, (b) 20 volume % of Carbon deposited at  $750^{\circ}$ C, (c) 15 volume% of Carbon deposited at  $750^{\circ}$ C(d)12.5 volume % of Carbon deposited at  $600^{\circ}$ C, FePt film capped with carbon deposited at  $600^{\circ}$ C having thickness (e) 8 nm and (f) 20 nm.

### 3.3.2 Magnetization versus field

Magnetization of the FePt-C film as seen in figure 3.3, shows that the film is having perpendicular magnetic anisotropy with coersivity of about 3 Tesla. Perpendicular magnetic anisotropy exhibited by these films are due to the  $L1_0$  ordering. The loop in the inplane measurement indicates that a complete  $L1_0$  ordering has not been attained. In FePt granular films, granular sizes of above 7 nm gives a complete ordering and that of less than 3 nm gives a complete disorder [23]. In partial ordering, the core remains ordered and the near surface becomes disordered until a threshold is reached where the granule is completely in disordered cubial structure [6]. It is evident from the TEM image that though most of the granules are of above 7 nm in size, there are granules with size less than 7 nm. This confirms the absence of a complete  $L1_0$  order in the film [24].

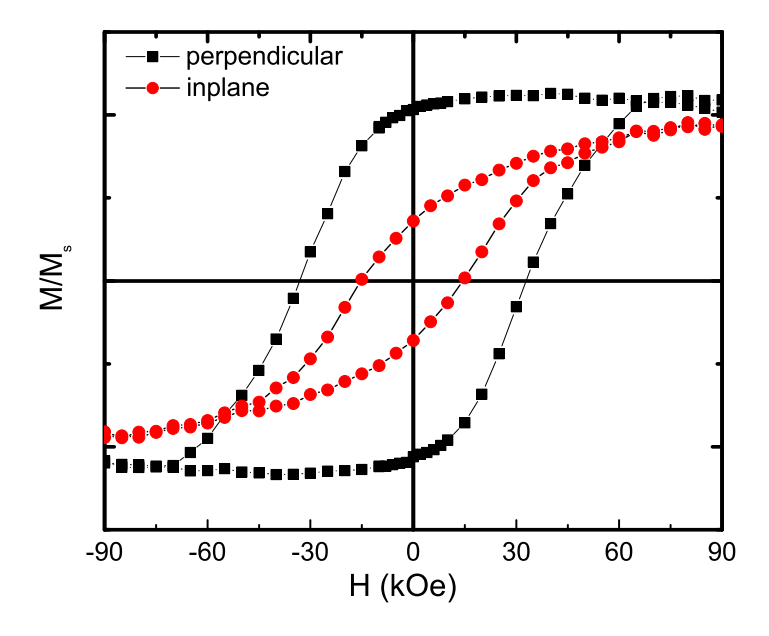
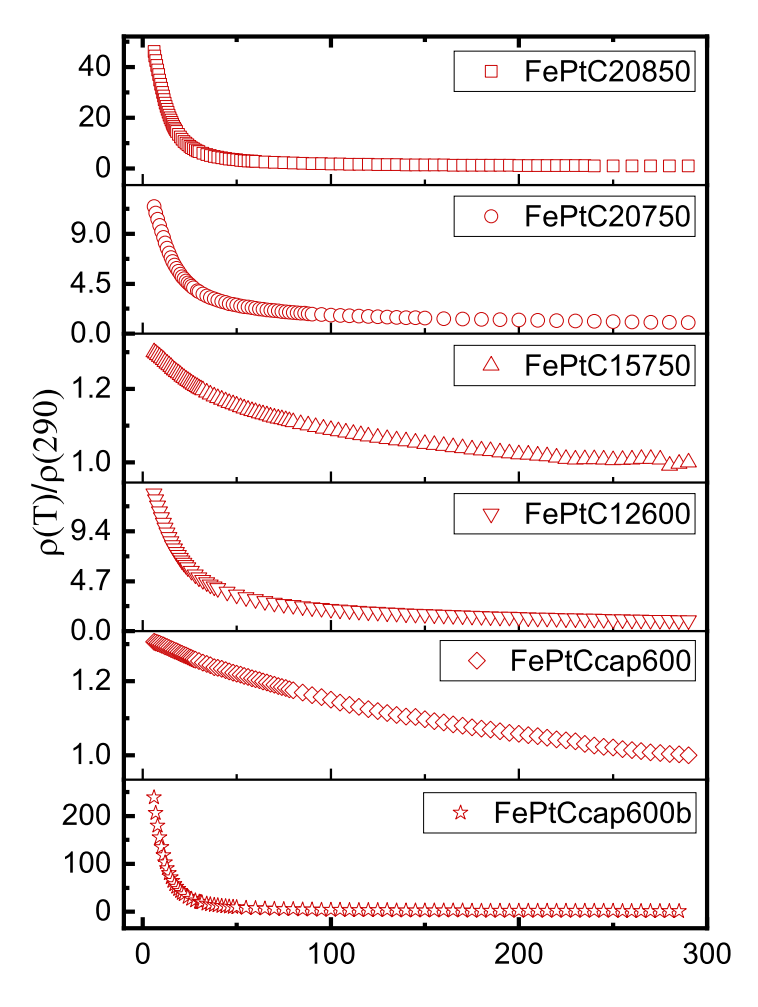


Figure 3.3: M-H curve of FePt-C granular film (FePtC20850).

# 3.3.3 Resistivity versus temperature

The resistivity of the films is shown in figure 3.4. All the samples show negative temperature coefficient of resistance throughout the temperatures measured (  $6\,\mathrm{K}$  to  $300\,\mathrm{K}$  ).



*Figure 3.4:* Resistivity of fePt films of FePtC20850, FePtC20750, FePtC15750, FePtC12600, FePtCcap600, FePtCcap600b

Electron transport in metals is explained using diffusion of electrons and scattering of them by the interaction of lattice vibration and magnetic impurity. Diffusion of electrons leads to a finite resistance of metals at T = 0, whereas, in noncrystalline media, a finite resistance is not observed as temperature tends to zero. A large number of studies have shown that metal-insulator granular films exhibit hopping mechanism in the insulating regime at low temperatures [25]. Moreover, this is debated over decades over two well known mechanisms; Mott variable range hopping and Efros-Shklovskii variable range hopping [26]. Both of these mechanism have its origin in the picture of localization of electrons.

### 3.3.3.1 Anderson localization

In 1958, P W Anderson introduced the concept of localization [27] to explain the electron transport in non-crystalline media. He considered a crystalline array of random potential wells having depth at a range of  $'V_0'$ . At a certain value of  $V_0$ , electron wave function is localized with the absence of wave function overlap and conductivity vanishes at zero temperature when the states at the fermi energy are localized. Electron transport from one localized state to another can occur at the cost of thermal energy, Miller and Abrahams first pointed out [28], and this process is widely called as hopping or thermally activated tunneling. Though electron can tunnel far away finding states having same energy and activation energy reduces as temperature comes down, on an ensemble average the system behaves as insulator. In other words, an insulator with finite density of states at Fermi level is possible. Here, Mott came up with the concept of mobility edge. He stated that in the localization regime, the conduction band can have a band tail with electrons trapped in it and a sharp energy level exists, called mobility edge, which separates

the localized states from the non-localized states in the conduction band.

If fermi energy ( $E_F$ ) lies below the mobility edge ( $E_C$ ), conduction can happen in two ways. One is by excitation of electron to mobility edge as a result of phonon collision or auger process and the second is by thermally activated hopping. There are three different ways hopping can occur; Nearest neighbour hopping, Mottvariable range hopping and Efros-Shklovskii variable range hopping.

### 3.3.3.2 Nearest neighbour hopping

When thermal energy is higher than the average energy difference between adjacent sites, electron with energy less than  $E_F$  can hop to the nearby states having energy greater than  $E_F$  receiving energy from phonon. This transport mechanism is also called as activated type of hopping. Probability of electron transport in such a case can be expressed using Boltzman equation and this is proportional to conductivity of electrons as can be stated below,

$$\sigma_N = \sigma_o exp(-\Delta E/k_B T) \tag{3.1}$$

where,  $\sigma_N$  is the conductivity by nearest neighbour hopping,  $\sigma_0$  is the proportionality constant,  $\Delta E$  is the average energy difference between adjacent sites,  $k_B$  is the Boltzmann constant and T is the temperature. If  $\Delta E$  is greater than thermal energy ( $k_BT$ ), electron cannot hop to nearest neighbour. Possible mechanism in such a case are Mott variable range hopping and Efros-Shklowskii variable range hopping.

### 3.3.3.3 Mott variable range hopping

In 1968, Mott first argued that at low temperatures the hopping process is not between nearest neighbours. Assuming density of states around fermi energy as constant, total number of states per unit energy within a range R of the site can be expressed as

$$n(E_F) = (4/3)\pi R^3 N(E_F)$$
(3.2)

where,  $N(E_F)$  is the density of states around fermi level. Thus lowest activation energy required to occur hopping process through a distance R is

$$\Delta E = 1/n(E_F) = 1/(4/3)\pi R^3 N(E_F)$$
(3.3)

Thus, as the range increases activation energy reduces. However, as the process is ultimately tunneling of electrons, hopping probability should exponentialy decay when hopping length increases. Therefore, hopping probability or conductivity contains an additional term to the equation 3.1 in this case.

$$\sigma_{VRH} = \sigma_0 exp(-2\alpha R) exp(-\Delta E/k_B T)$$
 (3.4)

where,  $\alpha^{-1}$  is the attenuation length of the localized electron wave function. First exponential in the expression reduces with R and the second one increases with R. Therefore, optimum hopping length is the one where probability is maximum. The value of R when the probability is maximum is

$$R = [1/8\pi N(E_F)\alpha k_B T]^{1/4}$$
(3.5)

Substituting the range R in equation 3.4 gives the expression for conductivity as

$$\sigma_M = \sigma_0 exp[(-T_M/T)^{1/4}] \tag{3.6}$$

In general, for a D dimensional system the expression is of the form

$$\sigma_M = \sigma_0 exp[(-T_M/T)^{1/(D+1)}] \tag{3.7}$$

Therefore, for a 3 dimensional system, the exponent is 1/4 and for a 2 dimensional system it is 1/3. Mott's derivation is based on the assumption that hopping energy is inversely related to the cube of hopping distance. Apsley and Hughes succeeded in deriving the same expression [29] by combining hopping distance and hopping energy into a single parameter as they are independent parameters. Mott assumed a constant density of states around fermi energy. However, electron-electron interaction in disordered systems can result in a reduction in the density of states at fermi level.

### 3.3.3.4 Efros-Shklovskii variable range hopping

Accounting the electron electron interaction, A. L. Efros and B. I. Shklovskii argued that density of states can vanish around fermi energy at sufficiently low temperature. If  $E_i$  and  $E_j$  are the states just above and below fermi level, energy required to jump an electron from the state below to above is

$$\Delta E = E_j - E_i \tag{3.8}$$

But, in the presence of a hole, electron-electron interaction reduces the energy to

$$\Delta E = E_j - (E_i + e^2/4\pi\epsilon r_{ij}) \tag{3.9}$$

where,  $\epsilon$  is the permittivity of the medium and  $r_{ij}$  is the distance between electronhole pair. Now, since  $\Delta E$  should always be positive, there exists a gap of width  $e^2/4\pi\epsilon r_{ij}$ . In other words, no states exists within this gap. This gap in the density

of states is called as coulomb gap. Therefore, minimum activation energy to jump from a state below fermi level to that of above fermi level is

$$\Delta E = e^2 / 4\pi \epsilon R \tag{3.10}$$

Applying this activation energy into equation 3.4 and maximizing the expression gives

$$R = \left[e^2/(4\pi\epsilon\alpha k_B T)\right]^{1/2} \tag{3.11}$$

Substituting this R in equation 3.4 gives the expression for conductivity as

$$\sigma_{ES} = \sigma_0 exp[(-T_{ES}/T)^{1/2}] \tag{3.12}$$

irrespective of the dimensions.

### 3.3.3.5 Analysis of resistivity data

Resistivity of the FePt film having 20 volume % of Carbon deposited at  $850^{0}$ C, 20 volume % of Carbon deposited at  $750^{0}$ C and Carbon capped and deposited at  $600^{0}$ C with thickness 20 nm (figure 3.5 (b),(c) and (f) respectively) fit to general expression for hopping mechanism,  $\rho = \rho_0 exp((T_0/T)^x)$ , above 25 K. The data do not fit to the above expression at low temperatures. Other samples do not fit to the expression at any range of temperature. Fitting parameters are tabulated in table 3.2. The exponent values from the fit are 0.576, 0.313 and 0.221 for samples FePtC20850, FePtC20750 and FePtCcap600b respectively. Thus, the first of these sample which is well separated with 1 to 2 nanometers separation thus shows ESVRH indicating that the electron-electron interaction dominates in it. The granules which are closer show 2d-MVRH and 3d-MVRH mechanisms for 8 nm and 20 nm thick samples respectively. Noticeably, a change in thickness of the film from

8 nm to 20 nm modifies electron conduction from 2d to 3d in connection with the exponent values of 2d and 3d MVRH while fitting to VRH expression. The exponent from the fit to ES-VRH is rather in agreement with the value, 0.55 deduced by Mobius and Ritcher [30] by means of computer in contrast to the analytical result (0.5) of Efros and Shklovskii.

The cross over between MVRH and ES-VRH has been reported [31], [32]. There, MVRH cross over to long range electron electron interaction dominant ES-VRH towards low temperatures. In a similar note, controlling the intergranular distance electron transport can be tuned to different regimes. Correlating the microstructure and the resistivity graph, it we show that the gap between the granules play the role of modifying the electron transport to different hopping mechanisms.

The fit to hopping mechanism was extrapolated to low temperatures as shown in figure 3.5 to know how the resistivity behaves at temperatures below 25 K. The resistivity was found decreasing from the extrapolated curve. Paolo Allia et.al. [17, 33] and Paolo Tiberto et.al. [34] also have shown that FePt-Ag multilayered granular films have a drop in resistivity below 11 K. Those films were metallic continuous films with positive temperature coefficient of resistance throughout the temperature regimes, whereas, the films in the present study are granular and have negative temperature coefficient of resistance. Moreover, the deviation in the granular films studied here, occurs at a higher temperature (25 K) and it is a gradual change rather than a sudden change. But the striking similarity in the enhanced conduction at low temperature indicates that the effect emanate from the FePt granules.

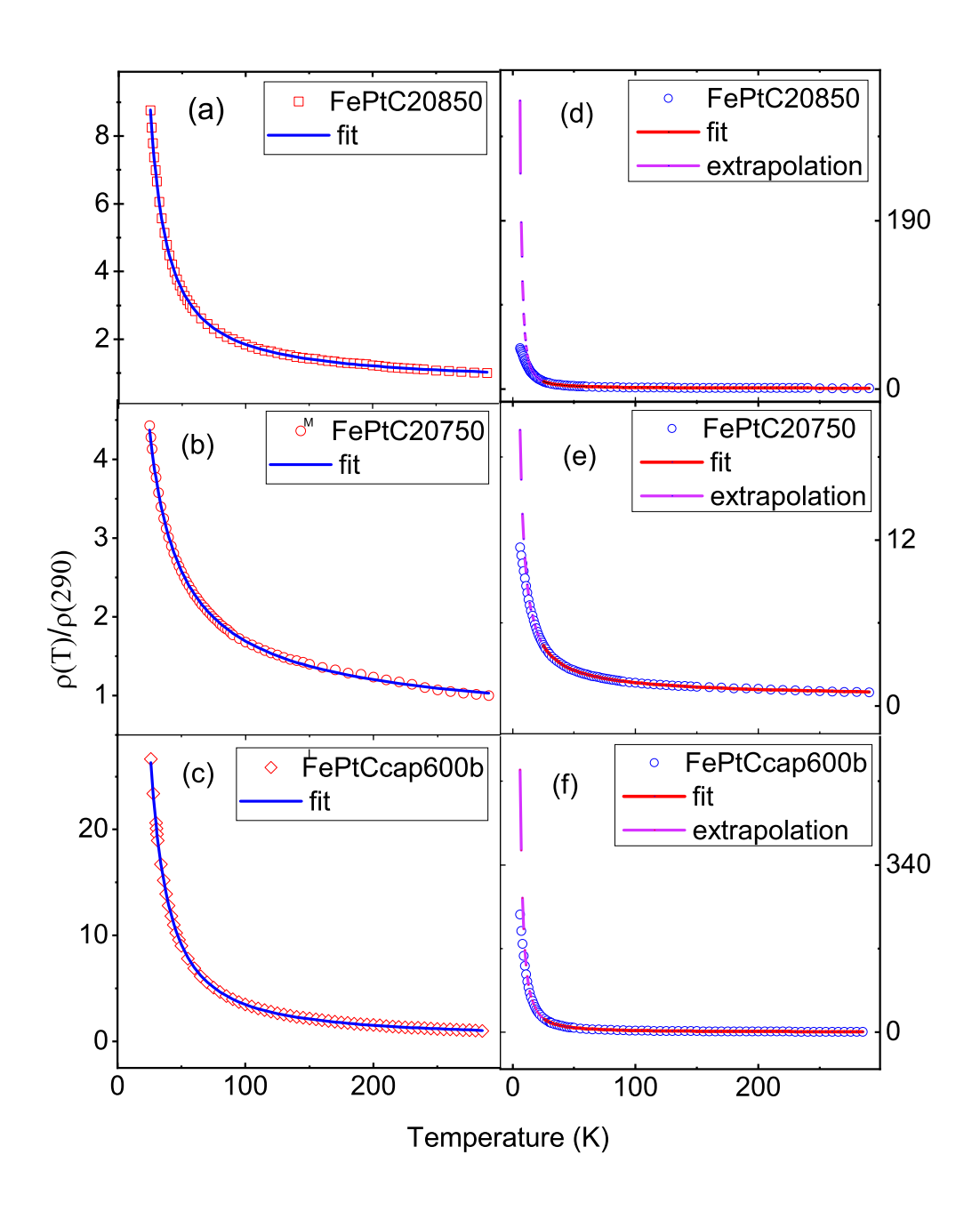


**Figure 3.5:** Resistivity of fePt films of FePtC20850, FePtC20750, FePtC15750, FePtC15600, FePtCcap600, FePtCcap600b, with fit to general hopping expression. The dashed line is the extrapolation of fit to lower temperatures.

Sample	$T_0(K)$	x	R – square
FePtC20850	152.48	0.576	0.9999
FePtC20750	597.44	0.313	0.9998
FePtCcap600b	2.83E+5	0.221	0.9998

**Table 3.2:** Shows relevant fitting parameters of the samples which fit to expression for hopping mechanism.

Extrapolation of the resistivity fits towards temperatures below 25 K shows that the resistivity deviates to a lower value compared to the extrapolation of fit. In other words, the conductivity of the sample has been enhanced from the expected mechanism at low temperatures. The exponent of hopping at every temperature can be found out by calculating reduced activation energy.

# 3.3.4 Reduced activation energy

Metals generally show positive temperature coefficient of resistance. Metals have finite conductivity as temperature tends to zero in contrary to insulators. Disordered metals can show negative temperature coefficient of resistance as well as finite conductivity towards low temperature [35]. According to Anderson criteria, around the critical regime of metal-insulator transition of a disordered system, resistivity follows a power law behaviour [36], i.e.,  $\rho \propto T^{-\beta}$ , with  $\beta$  to be independent of temperature. Reduced activation energy [37,38] (W) is defined as

$$W(T) = -\frac{\mathrm{d}ln(\rho)}{\mathrm{d}ln(T)} \tag{3.13}$$

Subsequently, deriving the W(T) of power-law expression yields  $W(T) = \beta$ ,

i.e, slope of W is zero in the critical regime and therefore, metal-insulator transition is nothing but a sign conversion in the slope of W. If the slope of W is negative, the material is insulating and if the slope is positive it is metallic. Figure 3.6 show W versus T plots of FePt films . In Figure 3.6 (a), (b) and (f), there is a slope change from positive to negative at 21 K and in 3.6 (c) and (e) at 32 K indicating metal-insulator transition. It shows that the hopping transport suppresses the metallicity and reduces the critical region to a lower temperature. A linear fit was shown with red lines to the linear portion of the W versus T graph in Figure 3.6. The fit gives the slopes, -0.56, -0.35, 0.09, -0.13, -0.28, respectively from Figure 3.6 (a), (b), (c), (e) and (f). There is no slope change in (f). The negative values of the slopes of figures (a), (b) and (f) are found comparable to the exponents of the hopping mechanisms seen from the resistivity fit. The slope change above critical regime is found deviating depending on the intergranular separation. Therefore, electron transport mechanism in these films can be tuned by varying the intergranular separation at temperatures above critical region.

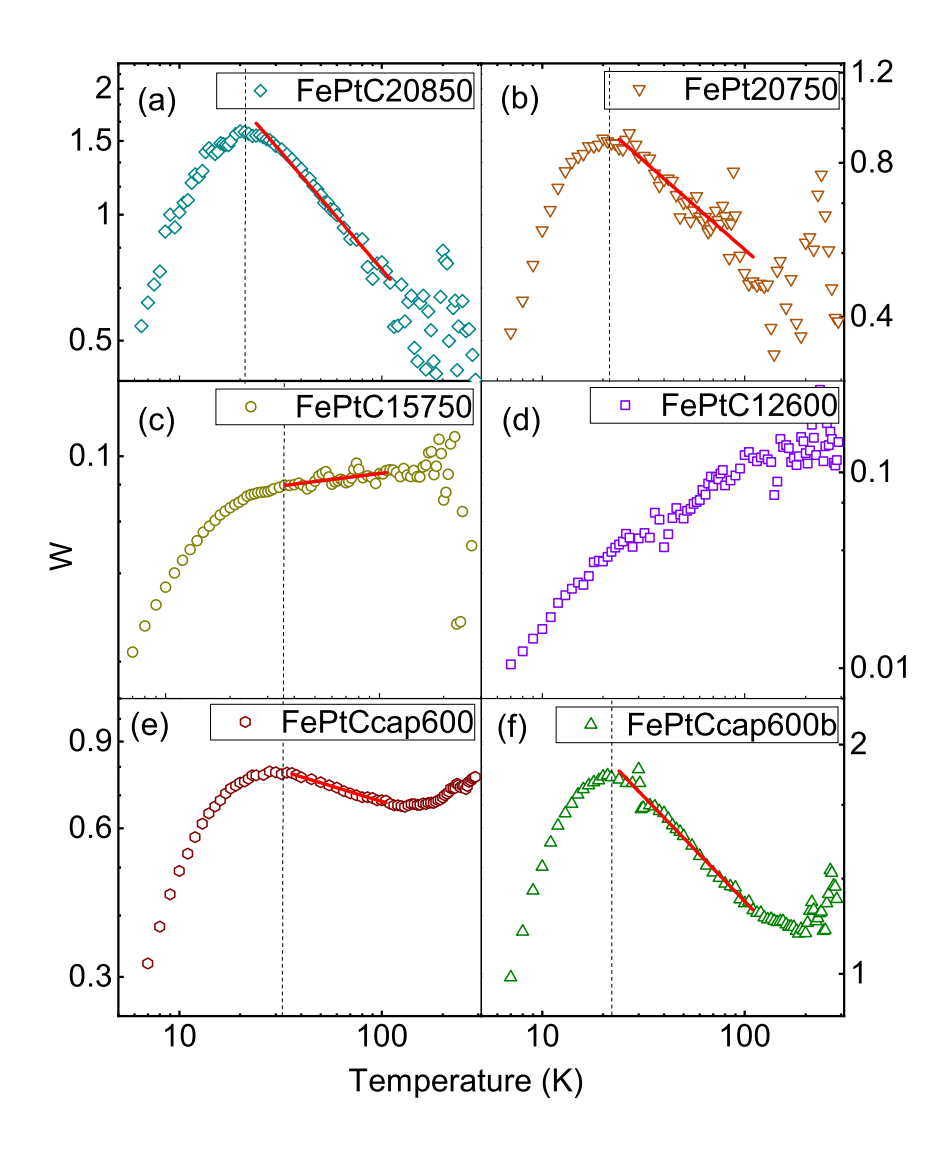
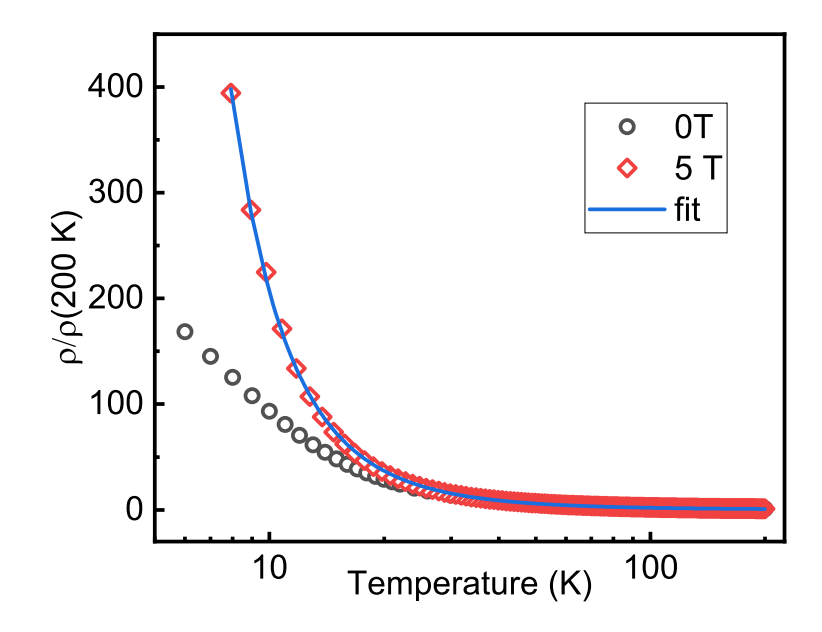


Figure 3.6: The image shows plots of reduced activation energy (W) versus temperature of FePt-C granular films of (a)FePtC20850, (b)FePtC20750, (c)FePtC15750, (d)FePtC12600,(e)FePtCcap600, (e)FePtCcap600b, . The transition temperature is marked with a vertical dashed line. Positive slope indicates metallic behaviour and negative slope after the peak indicates insulating nature of film. The line in the curves are the linear fits.

# 3.3.5 Model for spin dependent electron transport

From the resistivity data analysis (figure 3.5), an enhanced conductance was observed at lower temperatures with respect to the fit. This enhancement at lower temperatures can be attributed to the spin-dependent electron transport through the magnetic intergranular interaction of ferromagnetic type. This has been investigated from the resistivity measurement of one of the sample (FePtCcap600b) at a saturating magnetic field of 5 Tesla. The resistivity at zero field and 5 T field are shown in figure 3.7. The resistivity at 5 T fits to the VRH throughout the temperature regimes. The exponent obtained from the fit, 0.27, matches to the 3D-MVRH. This result strengthens the assumption that the enhanced conduction in the zero field resistivity data is due to spin dependent electron transport.



*Figure 3.7:* Resistivity of FePtCcap600b at zero field and 5 T field. The resistivity at 5 T fits to the VRH throughout the temperature regions.

Lee et. al. attributed the huge magnetoresistance observed in FePt-C granular films to the spin dependent electron transport between the grains. The granular film consists of an enseble of granule- insulator- granule sandwiches similar to the multilayer magnetic tunnel junctions acting as tunnel barriers where the granules are single domain ferromagnetic structures [39]. Spin dependent transport in Co-SiO<sub>2</sub> has been systematically investigated by Sankar et. al. [40]. It was found that spin dependent transport is prevalent in the insulating region of the film, i.e., below the percolation threshold and in the region of hopping or tunneling transport. The total conductivity of spin dependent transport of electrons across the granular insulator granular channel as a function of temperature can be expressed as [41–43]

$$G = G_0(1 + B < \cos\alpha >) \tag{3.14}$$

where, B is a constant,  $G_0$  is the conductivity independent of spin orientation (here, it is the hopping mechanism) and the fraction ( $G/G_0$ ) is decided by the angle between spin orientation of adjacent granules, i.e.  $\alpha$ .  $G/G_0$  versus temperature of the sample having 20 volume % of Carbon annealed at 850 $^{0}$ C has been shown in figure 3.8(a). The data is obtained by dividing the measured conductance (G(T)) with the VRH fit extrapolated to low temperature ( $G_0(T)$ ).

For a homogeneous system,  $< cos\alpha >$  can be assumed from the model for superparamagnetic particle ensemble as reported to calculate temperature dependent magnetoresistance in magnetic granular films with perpendicular magnetic anisotropy [43]. If  $\theta_1$  and  $\theta_2$  represent polar angles and  $\phi_1$  and  $\phi_2$  represent azimuthal angles of spin orientation of adjacent granules, then  $cos\alpha$  can be expressed as

$$\cos\alpha = \cos\theta_1 \cos\theta_2 + \sin\theta_1 \sin\theta_2 \cos(\phi_1 - \phi_2) \tag{3.15}$$

Magnetic energy of the pair of granules can be written as

$$U = -KV(\cos^2\theta_1 + \cos^2\theta_2) - J\cos\alpha \tag{3.16}$$

where, K, V and J are anisotropy constant, volume of granule and exchange integral respectively. The first term in the above expression is the anisotropy energy and the second term is the energy due to intergranular interaction.  $< cos\alpha >$  can be calculated by taking Boltzmann average of  $cos\alpha$ .

$$\langle \cos \alpha \rangle = \frac{\int_{\theta_1} \int_{\theta_2} \int_{\phi_1} \int_{\phi_2} \cos \alpha e^{-U/K_B T} \sin \theta_1 \sin \theta_2 \, d\phi_2 \, d\phi_1 \, d\theta_2 \, d\theta_1}{\int_{\theta_1} \int_{\theta_2} \int_{\phi_1} \int_{\phi_2} e^{-U/K_B T} \sin \theta_1 \sin \theta_2 \, d\phi_2 \, d\phi_1 \, d\theta_2 \, d\theta_1}$$
(3.17)

Figure 3.8(b) shows numerical simulation of the temperature dependence in  $< cos \alpha >$  at different exchange integral (*J*) values. The exchange integral, as seen

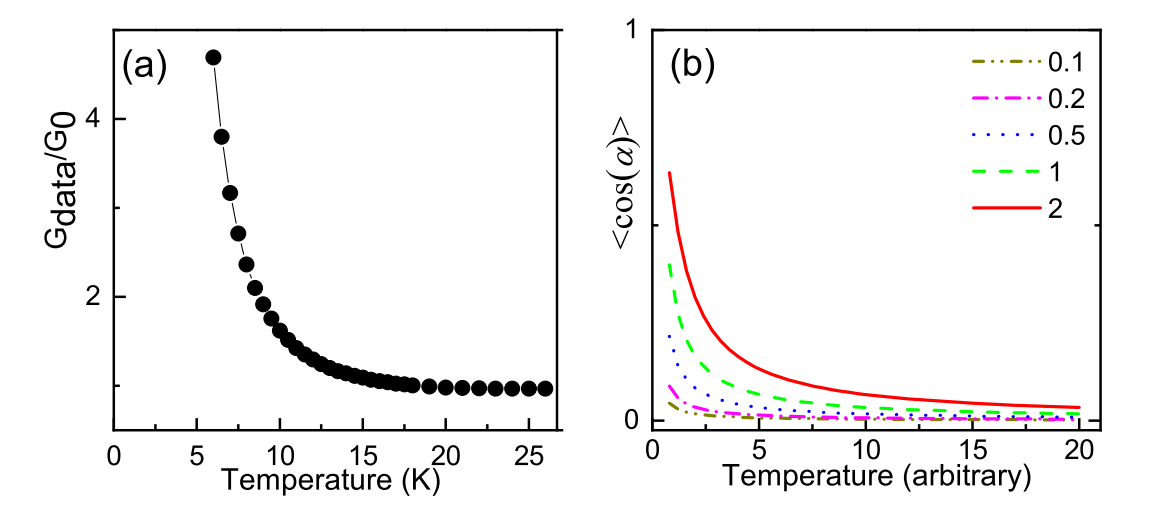


**Figure 3.8:** Depicting (a) the fractional increase in conductivity obtained from the resistance data of the sample having 20 vol % of Carbon annealed at  $850^{\circ}$ C divided by the VRH fit extrapolated to low temperature and (b) simulation of the model showing  $<\cos\alpha>$  as a function of temperature at different values of exchange integral.

in the figure, enhances the conductance at low temperature. Hence, intergranular

interaction can be a key factor in modifying the conductance as thermal energy reduces.

# 3.4 Conclusion

FePt-C granular films have been studied by varying intergranular separation. A mutual correlation was observed between the microstructure and resistivity of the films. It was observed that the resistivity can be tuned between different hopping mechanisms such as Mott VRH, ES-VRH and extended critical regime in these films above 25 K depending on the average intergranular separation. In contrast, at temperatures below 25 K all the films showed metallic nature from the reduced activation energy calculation. The resistivity at a saturating magnetic field was fitted to the hopping mechanism throughout the lowest temperatures measured indicating the enhanced transport in comparison with the resistivity of these films at zero field in temperatures below 25 K. Further, the enhanced conductance at low temperature was explained using the model for spin dependent electron transport across the FePt granules having ferromagnetic exchange interaction.

# References

- [1] I. S. Beloborodov, A. V. Lopatin, V. M. Vinokur, and K. B. Efetov, *Rev. Mod. Phys.*, vol. 79, pp. 469–518, 2007.
- [2] C. Grimaldi, *Phys. Rev. B*, vol. 89, p. 214201, 2014.
- [3] G. Dumpich, A. Carl, and P. Mikitisin, *Materials Science and Engineering: A*, vol. 217-218, pp. 353–357, 1996.
- [4] D. V. A. Ivanov O. A., Solina L. V. and M. L. M., vol. 35, p. 81, 1973.
- [5] Y. K. Takahashi, T. Koyama, M. Ohnuma, T. Ohkubo, and K. Hono, *Journal of Applied Physics*, vol. 95, pp. 2690–2696, 2004.
- [6] Y. Zhang, A. Kalitsov, J. Ciston, O. Mryasov, B. Ozdol, J. Zhu, S. Jain, B. Zhang, B. Livshitz, A. Chernyshov, A. Ajan, P. Dorsey, G. Bertero, R. Acharya, A. Greene, and S. Myers, AIP Advances, vol. 8, p. 125018, 2018.
- [7] T. Ono, T. Moriya, M. Hatayama, K. Tsumura, N. Kikuchi, S. Okamoto, O. Kitakami, and T. Shimatsu, *Appl. Phys. Lett.*, vol. 110, p. 022402, 2017.
- [8] T. Shiroyama, B. S. D. C. S. Varaprasad, Y. K. Takahashi, and K. Hono, *AIP Advances*, vol. 6, p. 105105, 2016.
- [9] L. Zhang, L. Liu, K. Hayasaka, and S. Ishio, *Journal of Alloys and Compounds*, vol. 651, pp. 389–392, 2015.
- [10] M. Matsumoto, A. Morisako, and N. Katayama, *Journal of Applied Physics*, vol. 93, pp. 7169–7171, 2003.

- [11] Y. K. Takahashi and K. Hono, Scripta Materialia, vol. 53, pp. 403–409, 2005.
- [12] E. Yang, D. E. Laughlin, and J. Zhu, *IEEE Transactions on Magnetics*, vol. 46, pp. 2446–2449, 2010.
- [13] L. Zhang, S.-X. Xue, Z.-G. Li, Y.-P. Liu, and W.-P. Chen, Appl. Phys. A, vol. 116, pp. 1257–1260, 2014.
- [14] A. Perumal, Y. K. Takahashi, and K. Hono, *Appl. Phys. Express*, vol. 1, p. 101301, 2008.
- [15] Y. K. Takahashi, T. Ohkubo, M. Ohnuma, and K. Hono, *Journal of Applied Physics*, vol. 93, pp. 7166–7168, 2003.
- [16] D. Weller, G. Parker, O. Mosendz, A. Lyberatos, D. Mitin, N. Y. Safonova, and M. Albrecht, *Journal of Vacuum Science & Technology B*, vol. 34, p. 060801, 2016.
- [17] P. Allia, F. Celegato, M. Coïsson, P. Tiberto, F. Vinai, F. Albertini, and F. Casoli, *Journal of Applied Physics*, vol. 103, p. 073905, 2008.
- [18] A. Rajanikanth, T. Hauet, F. Montaigne, S. Mangin, and S. Andrieu, *Appl. Phys. Lett.*, vol. 103, p. 062402, 2013.
- [19] Z. Wen, H. Sukegawa, T. Seki, T. Kubota, K. Takanashi, and S. Mitani, *Sci Rep*, vol. 7, 2017.
- [20] T. Nozaki, T. Yamamoto, S. Tamaru, H. Kubota, A. Fukushima, Y. Suzuki, and S. Yuasa, APL Materials, vol. 6, p. 026101, 2018.
- [21] S. Miwa, M. Suzuki, M. Tsujikawa, K. Matsuda, T. Nozaki, K. Tanaka, T. Tsukahara, K. Nawaoka, M. Goto, Y. Kotani, T. Ohkubo, F. Bonell,

- E. Tamura, K. Hono, T. Nakamura, M. Shirai, S. Yuasa, and Y. Suzuki, *Nature Communications*, vol. 8, p. 15848, 2017.
- [22] X. Zhang, C. Wang, Y. Liu, Z. Zhang, Q. Y. Jin, and C.-G. Duan, *Scientific Reports*, vol. 6, p. 18719, 2016.
- [23] Y. K. Takahashi, T. Koyama, M. Ohnuma, T. Ohkubo, and K. Hono, *Journal of Applied Physics*, vol. 95, pp. 2690–2696, 2004.
- [24] J. Wang, H. Sepehri-Amin, H. Tajiri, T. Nakamura, K. Masuda, Y. K. Takahashi, T. Ina, T. Uruga, I. Suzuki, Y. Miura, and K. Hono, *Acta Materialia*, vol. 166, pp. 413–423, 2019.
- [25] E. Šimánek, Solid State Communications, vol. 40, pp. 1021–1023, 1981.
- [26] N. F. Mott, J. Phys. C: Solid State Phys., vol. 8, p. L239, 1975.
- [27] P. W. Anderson, Phys. Rev., vol. 109, pp. 1492–1505, 1958.
- [28] A. Miller and E. Abrahams, *Phys. Rev.*, vol. 120, pp. 745–755, 1960.
- [29] N. Apsley and H. P. Hughes, *Philosophical Magazine*, vol. 30, pp. 963–972, 1974.
- [30] A. Möbius and M. Richter, *Journal of Non-Crystalline Solids*, vol. 97-98, pp. 483–486, 1987.
- [31] R. Rosenbaum, *Phys. Rev. B*, vol. 44, pp. 3599–3603, 1991.
- [32] M. Ghosh, A. Barman, S. K. De, and S. Chatterjee, *Synthetic Metals*, vol. 97, pp. 23–29, 1998.

- [33] P. Allia, F. Celegato, M. Coïsson, P. Tiberto, F. Vinai, F. Albertini, and F. Casoli, *J. Phys. D: Appl. Phys.*, vol. 41, p. 134016, 2008.
- [34] P. Tiberto, P. Allia, F. Celegato, M. Coïsson, F. Vinai, F. Albertini, F. Casoli, S. Fabbrici, L. Nasi, and F. Bolzoni, *Journal of Magnetism and Magnetic Materials*, vol. 310, pp. 2231–2233, 2007.
- [35] R. Bhatia, K. Kumari, R. Rani, A. Suri, U. Pahuja, and D. Singh, *Reviews in Physics*, vol. 3, pp. 15–25, 2018.
- [36] M. Reghu, K. Vakiparta, C. O. Yoon, Y. Cao, D. Moses, and A. J. Heeger, *Synthetic Metals*, vol. 65, pp. 167–171, 1994.
- [37] A. G. Zabrodskii, *Phys.-Usp.*, vol. 41, no. 7, p. 722, 1998.
- [38] Z. W. Fan, P. Li, E. Y. Jiang, and H. L. Bai, J. Phys. D: Appl. Phys., vol. 46, p. 065002, 2013.
- [39] Y. H. Lee, M. S. Guo, C. S. Wur, P. C. Lin, and W. H. Li, *Journal of Magnetism and Magnetic Materials*, vol. 286, pp. 113–118, 2005.
- [40] S. Sankar, A. E. Berkowitz, and D. J. Smith, *Phys. Rev. B*, vol. 62, pp. 14273–14278, 2000.
- [41] J. Inoue and S. Maekawa, *Phys. Rev. B*, vol. 53, pp. R11927–R11929, 1996.
- [42] J. C. Slonczewski, Phys. Rev. B, vol. 39, pp. 6995–7002, 1989.
- [43] V. M. Kalita, A. A. Timopheev, A. F. Lozenko, S. M. Ryabchenko, A. V. Los, O. V. Stognei, and A. V. Sitnikov, *Journal of Applied Physics*, vol. 110, p. 113918, 2011.

# Chapter 4

# Electron Transport in Ag nanocluster films

In this chapter, the electron transport of very thin Ag nanocluster films is discussed. The films were deposited with various cluster coverages on the surface by varying the deposition time. The resistivity measurement shows metallic resistivity with the emergence of an upturn at low temperature. The data is analyzed by considering the possible scattering mechanisms. Further, the Hall effect of the film is discussed.

# 4.1 Introduction

Metal nanoclusters are quite fascinating entities as they exhibit strange electronic properties owing to the emergence of quantum phenomenon associated with the reduced size [1]. When the cluster size is comparable to the characteristic wave length of electron, they show a discrete spectrum of energy similar to atomic spec-

trum due to quantum confinement. Energy level separation in a nanocluster consisting of number of atoms, N and fermi energy,  $E_F$  is  $\delta = 4E_F/N$ . Therefore, energy level spacing increases as the cluster volume is reduced [2]. Metal nanoclusters offer a large variety of phenomenon as the synthesis of these structures are controllable in size and distribution.

The electron transport in metal nanoclusters is a widely discussed area as the wave nature of electrons becomes prominent in such a narrow scale. Electron scattering in nanoscale metal interconnects has been well discussed by Josell et. al. [3]. Electron scattering in these structures can arise from intrinsic contributions such as bulk resistivity, electron-phonon interaction, electron-electron interaction, localization and quantization, grain boundary scattering and surface scattering. Metal-insulator transition in 2-dimensional layered Ag nanoparticles has been previously reported [4], in which the upturn in resistivity was fitted to logarithmic dependence of temperature. Though the authors explains this with 2D Mott-Hubbard model, they do not exclude the possible mechanism of hopping in this region. In contrast, Muller et. al. theoretically explained [5] that in Au nanoclusters, the minimum in resistivity observed is due to coulomb blockade energy and thermal expansion. By varying intercluster distance of Ag in 2 dimensional film, Bansal et. al. [6] studied electron transport and showed that the resistivity can be tuned between metal to insulator as the intercluster separation is increased and at a particular separation the resistivity is independent of temperature. With such a background, electron transport around metal-insulator transition in nanoclusters are an area that has to be further explored in various dimensions. Here, a set of nanoclusters with different deposition times were prepared at the boundary of monolayer cluster film. As the deposition time is decreased at this region,

the clusters form to connected chains since the deposition is random.

# 4.2 Sample preparation and Measurements

The Ag nanoclusters were deposited on commercially available Si/SiO<sub>2</sub> substrates in Nanodep60 Nanocluster deposition system. Aggregationation chamber distance was set to 18 cm for all the samples to obtain clusters of similar size. Base pressure, Sputtering power and Argon gas flow rate are common for the set of samples prepared. Deposition conditions are tabulated in table 4.1. Four different samples were prepared by depositing the clusters at various deposition times. The deposition times were set in such a range that the continuity in electron transport reduces drastically. After deposition, the films were kept in a glove box filled with Argon gas in order to avoid oxidation of the film.

sample name	Deposition time (second)	Common	parameters
Ag120s	120	Base Pressure	: 1 E-8 Torr
Ag90s	90	Sputtering power	: 85 Watts
Ag75s	75	Ar flow rate	: 100 sccm
Ag68s	68	Aggregation length	: 18 cm

*Table 4.1:* Details of the Ag nanocluser films deposited using Nanodep 60.

Inorder to measure the resistivity and Hall effect of Ag nanocluster films, the films were deposited using a shadow mask of six-contact Hall bar prepared by laser cutting on stainless steel sheet. The width of the Hall bar channel is 1.5 mm. The schematic of resistivity and Hall effect measurement connections are depicted

in figure 4.1.  $V_{xx}$  is the voltage measured in the direction of current and  $V_{xy}$  is the voltage measured in the direction perpendicular to the current direction. For Hall effect measurement, a magnetic field was applied in the direction perpendicular to the plane of the film. It is not possible to judge the thickness of these films, because, the film primarily consists of one or two layers of clusters. Therefore, resistance of these films can be found out at maximum rather than resistivity. Longitudinal resistance,

$$R_{xx} = \frac{V_{xx}}{I} \tag{4.1}$$

Current was applied in opposite directions to remove contribution of voltage from thermal gradient. Hall resistance,

$$R_{xy} = \frac{V_{xy}}{I} \tag{4.2}$$

Current and magnetic field were applied in both the directions to remove contributions to voltage from magnetoresistance, thermal gradient and misalignment.

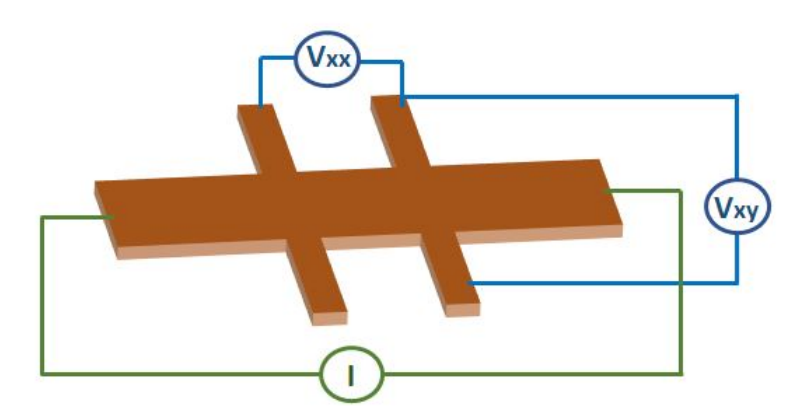


*Figure 4.1:* Hall bar sample measurement scheme for resistivity and Hall effect on similar sample.

# 4.3 Characterization and Analysis

### 4.3.1 FESEM characterization

The Ag nanocluster films were observed using FESEM. Images of the samples are shown in figure 4.2. The size of the clusters are about 20 nm. It can be seen that as the deposition time decreases the voids increase. The clusters are quite random in comparison with the films deposited previously by Bansal et, al [6]. They obtained uniformly distributed cluster films with the help of Trichlorocyclohexile Silance as underlayer. The random clusters obtained in the films under the current study are due to the absence of any restructuring of the clusters after landing it on the substrate. This process clearly depends on the kinetic energy of the clusters arriving on the substrate and the kind of surface of the substrate. As the deposition time reduces, the clusters are not enough to fill the whole substrate. The clusters are not distributed uniformily and it appears that they have been randomly connected.

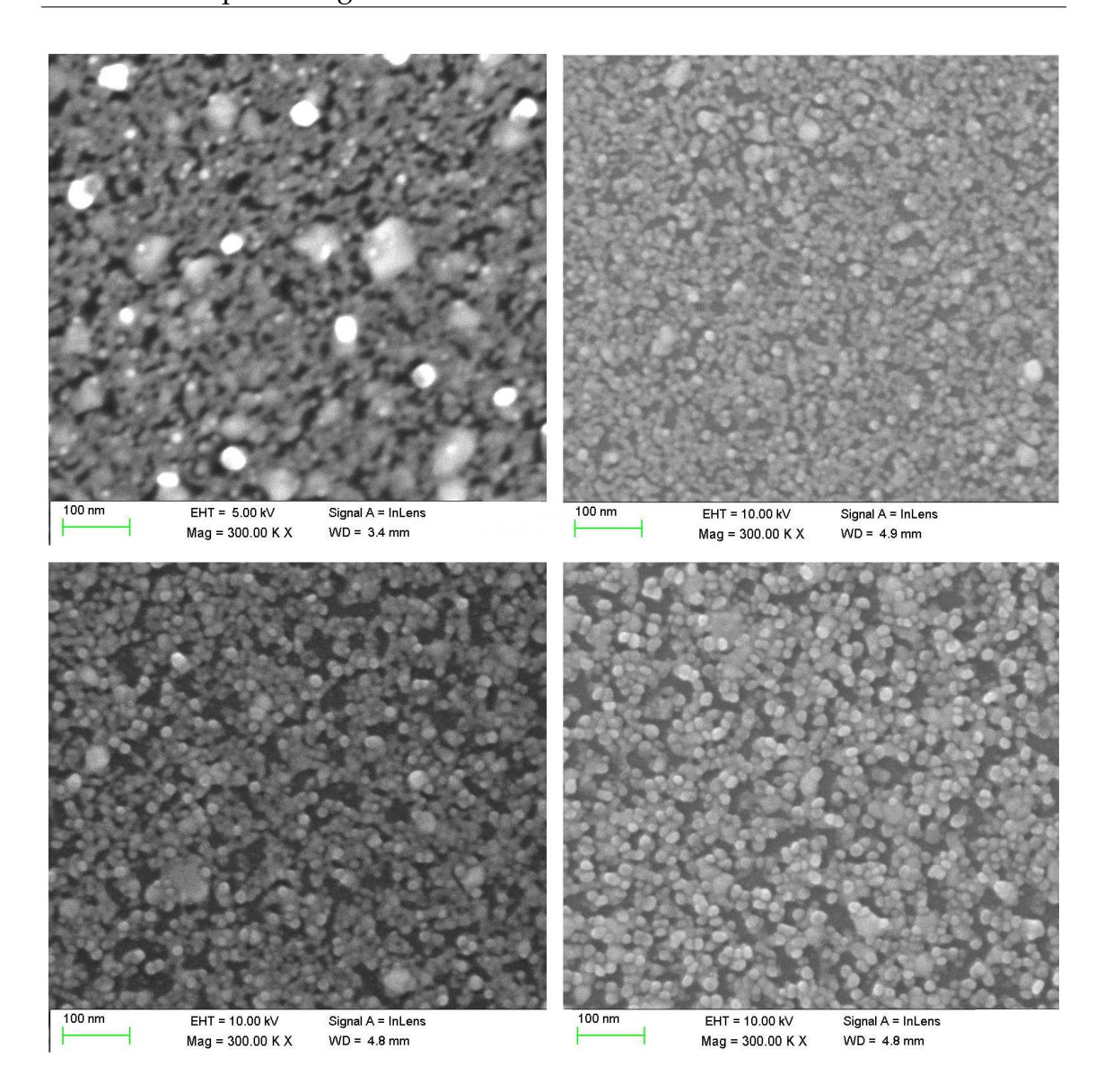


Figure 4.2: FESEM images of Ag nanocluster films deposited at (a) 120 seconds, (b) 90 seconds, (c) 75 seconds and (d) 68 seconds. A random deposition with increase in voids is observed as the deposition time reduces.

## 4.3.2 Resistivity of Ag nanoclusters

Resistance data of Ag nanoclusters are shown in figure 4.3. All the films are found showing metallic resistance. The emergance of an upturn is visible in the resistance at low temperatures as the deposition time decreases. Bid et. al, have earlier studied the applicability of Bloch-Gruneisen formula in Ag and Cu nanowires of 15 to 200 nm diameter [7]. It was shown there that the data fits well to the given model with significantly less Debye temperature which was attributed to the softening of phonon modes occuring in disordered systems from surfaces, interfaces and impurities.

### 4.3.2.1 Resistivity of Metals

In a perfectly crystalline matal, at 0 K electrons are expected to flow without any resistance and this mechanism is called as diffusive transport. But, at a non zero temperature, lattice vibration (phonon) creates scattering of electrons (electron-phonon interaction). In an impure metal or disordered substance there can be other contributions to resistivity. In summary, the resistivity of a metal originates from diffusion and scattering of electrons in the material. According to Matthiesen's rule contribution to resistivity from different scattering mechanisms are independent and hence, they are additive [8]. Therefore, for a perfect crystalline material, resistivity

$$\rho(c,T) = \rho_0(c) + \rho_i(T) \tag{4.3}$$

where,  $\rho_0(c)$  is the contribution to resistivity from impurity scattering, which depends on the concentration of impurity in the material and is independent of

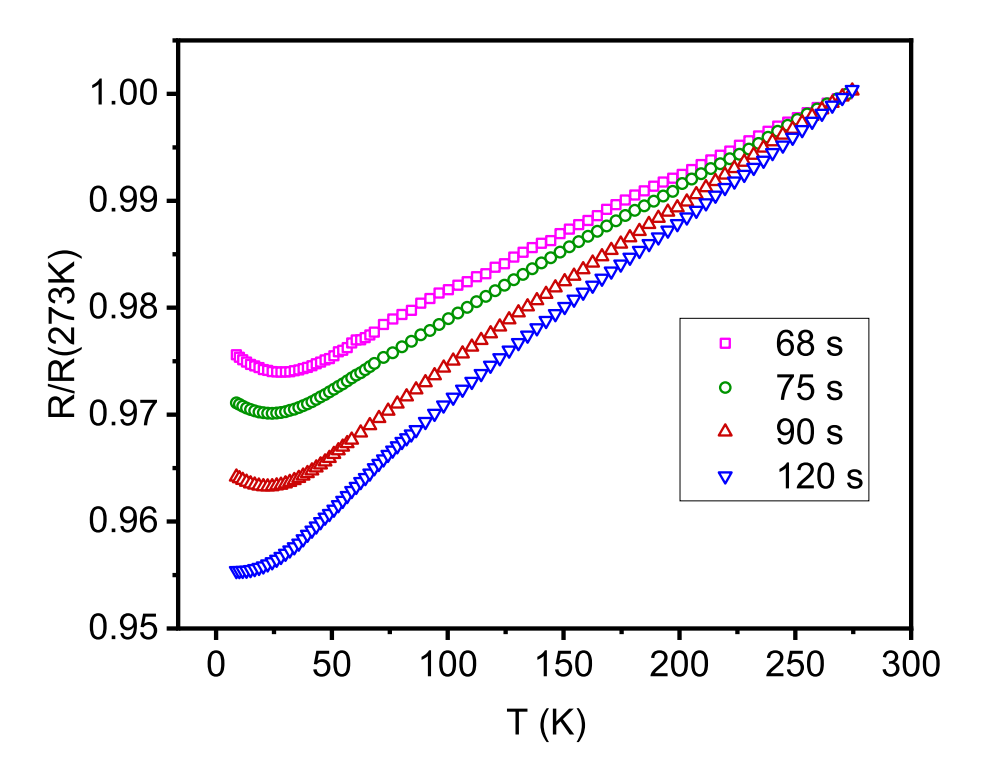


**Figure 4.3:** Resistance measurement of Ag nanocluster films at different deposition times. An upturn towards low temperatures is emerged as the deposition time is reduced.

temperature and the second term is the contribution from the intrinsic scattering mechanisms such as electron-phonon interaction, electron-electron interaction etc. Intrinsic contribution to resistivity,  $\rho_i$ , matches to the theoretical expression called as Bloch-Gruneisen formula,

$$\rho_i(T) = A \left(\frac{T}{\theta}\right)^5 \int_0^{\theta/T} \frac{z^5}{(e^z - 1)^2} dz$$
 (4.4)

where, T is the temperature,  $\theta$  is Debye temperature of electrical resistivity and A is a constant which depends on the material. This model was originally derived for monovalent metals having spherical fermi surface and Debye phonon

spectrum. However, this model was found valid for a large range of metals and metallic compound.

One can notice that at low temperature the resistivity is proportional to the fifth power of temperature ( $\rho_i \propto T^5$ ) and as temperature tends to infinity, resistivity follows a linear behaviour with temperature ( $\rho_i \propto T$ ). However interactions at low temperatures such as carrier interaction can reduce the power over temperature to as low as 2. Including this, the resistivity expression can be modified as [8]

$$\rho(T) = \rho_0 + A \left[ 1 + B \left( \frac{\theta}{T} \right)^p \right] \left( \frac{T}{\theta} \right)^5 \int_0^{\theta/T} \frac{z^5}{(e^z - 1)^2} dz \tag{4.5}$$

where, B and p are constants. When the value of p is positive, the added term is sufficiently high at low temperature and the resistivity becomes proportional to  $T^{(5-p)}$ . The integration covers the whole phonon spectrum upto the Debye temperature of the material. Whereas, the maximum phonon wavelength is limited by the size of the nanocluster. This may introduce a non zero lower limit to the ingegral part of the equation since

$$\theta_{min}/T = hc/\lambda_{max}k_BT \tag{4.6}$$

where, h is the planck's constant, c is the average velocity of acoustic phonon modes,  $\lambda$  is the phonon wavelength and  $k_B$  is Boltzmann constant. However, this does not have a pronounced effect for a cluster diameter of 15 nm in the fit or parameter values as observed in Ag nanowires of 15 nm diameter [7]. Therefore, the lower limit has been retained to zero in the model.

Resistivity of the films show emergence of an upturn in the resistivity at low temperatures as the deposition time comes down. In those films the data fits to the equation 4.5 from 45 K to the whole temperatures above that. The film deposited

for 120 seconds does not show a minimum and the data fits to the resistivity model throughout the temperature range measured. The fits are shown in figure 4.4

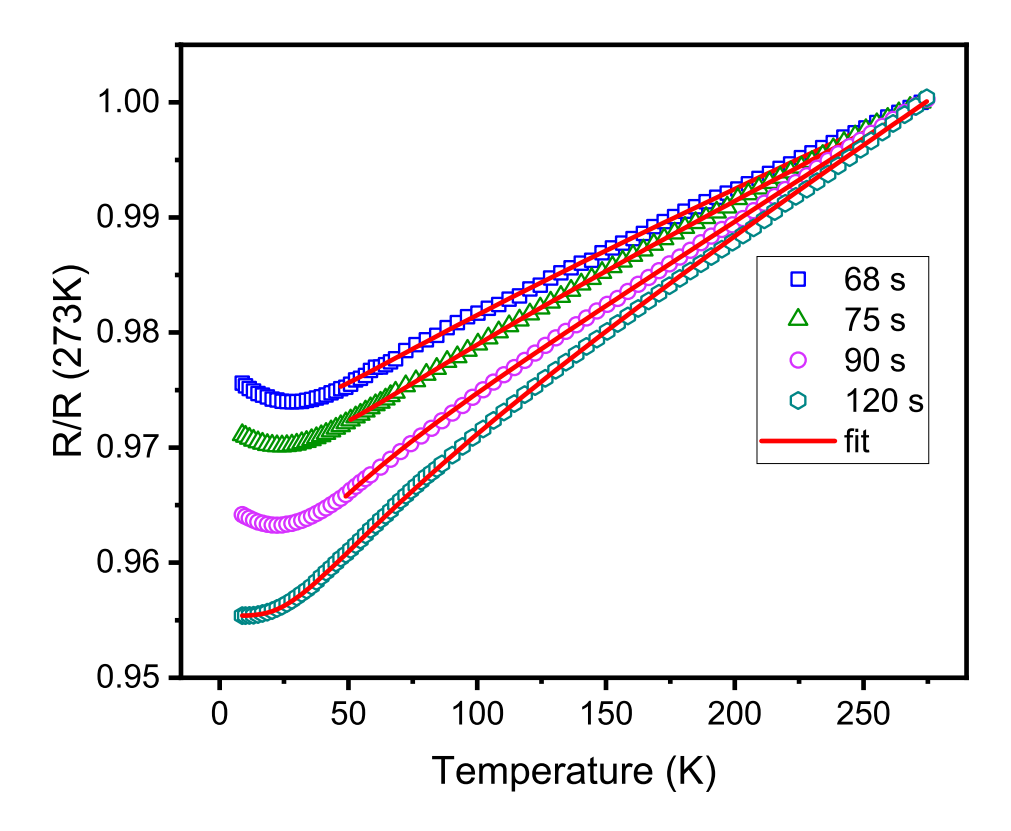


*Figure 4.4:* Fits to the resistivity data using the equation 4.5. clusters deposited for 120 seconds fits to the whole ranges of temperatures. Other data fit from 45 K to the temperatures above.

The fitting parameters are tabulated in table 4.2. Cheng et. al. observed that though the Debye temperature of bulk Silver is 235 K, for Silver nanowires with the Bloch-Gruneisen model it was found reduced to 151 K in comparison with the bulk counterpart [9] and this has been attributed to the softening of phonon modes at the surfaces, interfaces and impurities due to disorder. Ag120s which fits to the

whole ranges of temperatures gives the Debye temperature as 171 K. However, other films which have been fitted from 45 K to above, results in a higher values of Debye temperature compared to the result from Ag120s showing a reduction in Debye temperature as deposition time comes down. Ag90s has a Debye temperature of 231.8 K which is close to the bulk value and Ag75s and Ag68s have Debye temperatures 215 and 210 respectively. Over all, Debye temperature of these films has come down in comparison with the bulk Ag.

Sample	A	В	θ	р
Ag120s	$1.546 \times 10^{-2}$	$9.329 \times 10^{-1}$	171	0.2153
Ag90s	$3.356 \times 10^{-2}$	$7.332 \times 10^{-2}$	231.8	1.8051
Ag75s	$2.124 \times 10^{-2}$	$1.621 \times 10^{-1}$	215	0.0859
Ag68s	$2.118 \times 10^{-2}$	$1.570 \times 10^{-2}$	210	1.483

*Table 4.2:* Shows the fitting parameters of Ag nanocluster films in the metallic side.

#### 4.3.2.2 Minumum in the resistivity

In disordered metal, ocassionaly a minimum is observed in resistivity with a negative temperature coefficient of resistance at low temperatures [10–24] as we see in the resistivity data of Ag nanocluster films. In magnetic films, this has been explained with logrithmic temperature dependence attributing to Kondo effect, whereas, resistivity independent of magnetic field insisted others to prefer it to see a structural origin [22] as the cause. This minimum occurs at wide range of temperatures. It is independent of magnetic field and it is seen far below the magnetic curie temperature in case of magnetic materials. Because of these reasons appearance of a minimum at low temperature in these systems are different from kondo

effect [23]. Zhang et. al. observed [24] in Cobalt nanoclusters of different sizes of the order of 10nm and 1 $\mu$ m thick films, minimum in resistivity in broad ranges of temperatures and they fit to a combination of scattering terms such as fluctuation induced tunneling, electron-electron, electron-phonon and electron magnon interactions. However, the films prepared are very thin and further they does not make a complete surface coverage as the deposition time reduces.

Many amorphous alloys was found showing this  $T^{1/2}$  dependence in resistivity. However, they were contained either magnetic element or superconductivity. This hinder the generality of such a temperature dependence. To understand this, Cochrane and Strom-Olsane studied [22] this in Y-Al alloy glass which is neither magnetic nor supercoducting down to 60 mK. They found that the resistivity from 10 K to below shows  $T^{1/2}$  dependence. In the Ag nanocluster films studied here, the upturn in the resistivity is found to match with the additional  $T^{1/2}$  dependence along with the equation 4.5 as expressed below.

$$\rho(T) = \rho_0 + A \left[ 1 + B \left( \frac{\theta}{T} \right)^p \right] \left( \frac{T}{\theta} \right)^5 \int_0^{\theta/T} \frac{z^5}{(e^z - 1)^2} dz - CT^{1/2}$$
 (4.7)

where, C is a constant. The fit is shown in figure 4.5 and the fitting parameters are tabulated in table 4.3. A clear trend of dominance of  $T^{1/2}$  term is visible from the increase in the constant C as the deposition time reduces. Hence, instead of a logarithmic temperature dependence a power law dependence of 1/2 matches quite well at low temperatures and dominates as the films form into connected chains of clusters. The Debye temperatures obtained from the fit are lower than that of the bulk value. However, they are not as low as previously reported in Ag nanowires (151 K). It is observed that the minimum in the resistivity data is moving up in temperature as the deposition time decreases. The minimum value is taken from

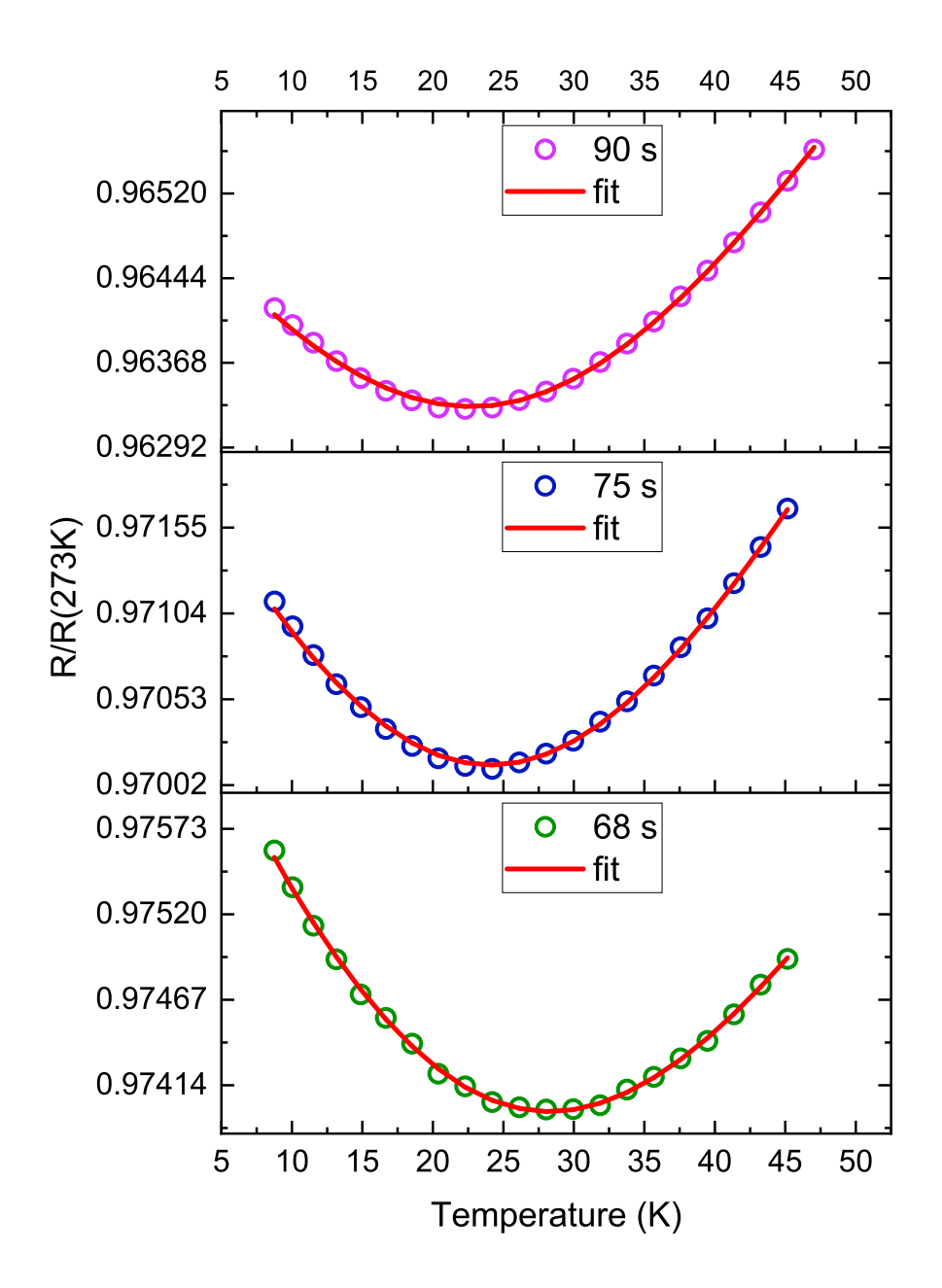


*Figure 4.5:* Resistivity minima at low temperature of the Ag nanocluster films deposited for 68, 75 and 90 seconds. The data is represented with open circle and the continuous lines over the data are the fits.

Sample	A	В	θ	р	С
Ag90s	$4.164 \times 10^{-2}$	$3.072 \times 10^{-2}$	221	1.5141	$6.912 \times 10^{-4}$
Ag75s	$3.334 \times 10^{-2}$	$5.963 \times 10^{-3}$	200	1.8171	$7.055 \times 10^{-4}$
Ag68s	$3.465 \times 10^{-2}$	$1.107 \times 10^{-2}$	210	1.1760	$9.342 \times 10^{-4}$

**Table 4.3:** shows the fitting parameters of resistivity of Ag nanocluster films in the region of upturn at low temperature.

the curve fitting to the corresponding region and is shown in figure 4.6. Therefore, it can be stated that the  $T^{1/2}$  dependent electron-electron interaction is enhanced as the cluster coverage on the surface reduces.

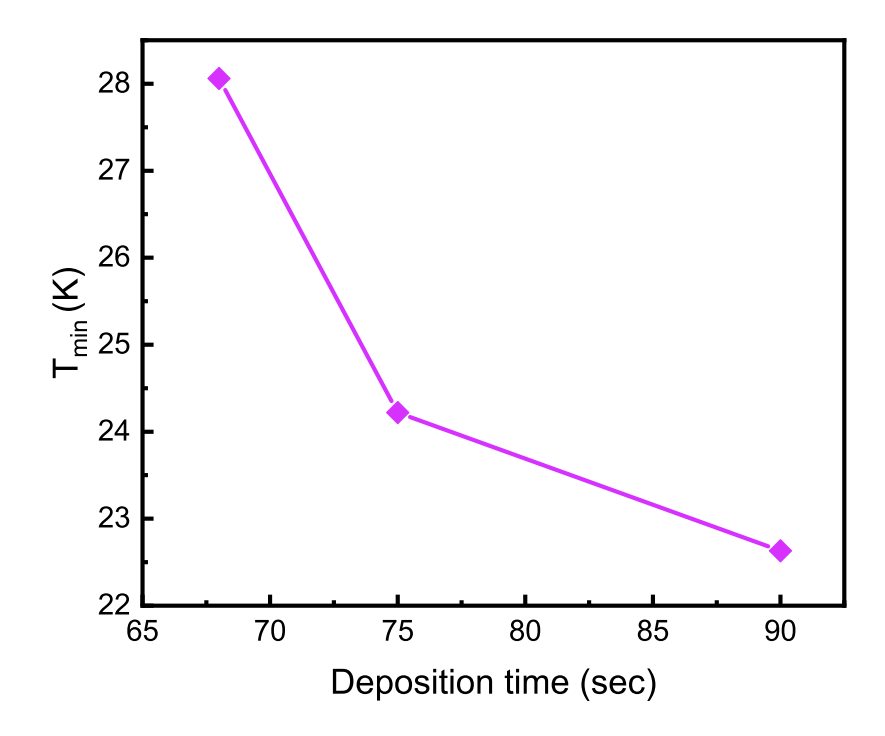


*Figure 4.6: Minimum in the resistivity as a function of deposition time.* 

## 4.3.3 Hall effect

Hall effect is the appearance of potential difference perpendicular to the flow of electrons when a constant magnetic field is applied perpendicular to the conductor as shown in the figure. This transverse potential difference is due to the Lorenz's force experienced by the moving electrons. If a current density  $j_x$  is ap-

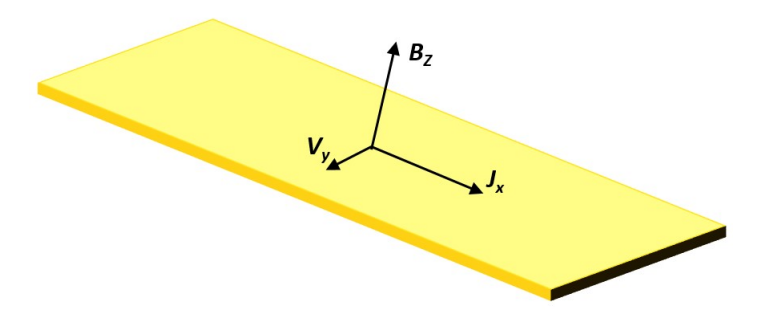


**Figure 4.7:** Showing the schematic of development of Hall voltage perpendicular to both current and magnetic field.

plied in- plane of a thin metal and a magnetic field  $B_Z$  is applied perpendicular to the plane, appearance of the transverse electric field due to Lorenz's force can be expressed as

$$E_y = v_x B_z \tag{4.8}$$

where,  $v_x$  is the velocity of electron in the direction of applied current and  $B_x$  is the external magnetic field normal to the conducting surface. For a conductor current density,  $J_x$  can be expressed as

$$J_x = nev_x \tag{4.9}$$

where, n is the density of electron. Applying  $v_x$  from equation 4.9 into equation 4.8 gives,

$$E_y = \frac{J_x B_z}{ne} \tag{4.10}$$

The transverse potential can be found as

$$V_y = E_y b = \frac{1}{ne} J_x B_z b = R_H \frac{I_x B_z}{t}$$

$$\tag{4.11}$$

where,  $R_H = 1/ne$  is the property of the system called Hall coefficient and t is the thickness of metal. There can be potential in y direction such as thermal emf ( $V_{th}$ ) arising from thermal gradient and magnetoresistance ( $V_m$ ): The former is independent of current direction and the later is independent of magnetic field direction. Current is applied both the directions and substracted to eliminate thermal emf. Hall resistance can be expressed as,

$$R(B) = \frac{R_H B}{t} + R_m \tag{4.12}$$

where,  $R_m$  is the magnetoresistance. The slop of the plot of Hall resistance(R(B)) versus B gives  $R_H/t$  from which Hall coefficient is obtained.

### 4.3.3.1 Hall effect of Ag nanocluster film

Hall effect of non-magnetic nanogranular or nanocluster films are quiet fascinating as a hall coeffeicent of 3 to 4 orders higher is observed around percolation threshold and this is generally called as giant Hall effect [25–27]. This effect has been understood as due to the interference of conduction electrons when the mean free path of electrons are higher than the length scales of nanogranules. Therefore, this is quantum mechanical in origin. The peak of Hall coefficient as a function of metal concentration is called as quantum percolation threshold. It was found that quantum percolation threshold is at a higher metallic concentration compared to the percolation threshold [25]. Ag nanoclusters deposited in this work should be

near the percolation threshold but in the metallic side as visible from the resistivity graph.

The Hall effect measurement of the Ag nanocluster film deposited at 120 second was measured in Cryogenic Magnetic Probe Station at different temperatures between 250 K and 25 K. The Hall resistance data have been taken applying current and magnetic field in either directions to remove misalignment contribution and magnetoresistance contribution. The data is shown in figure 4.8.

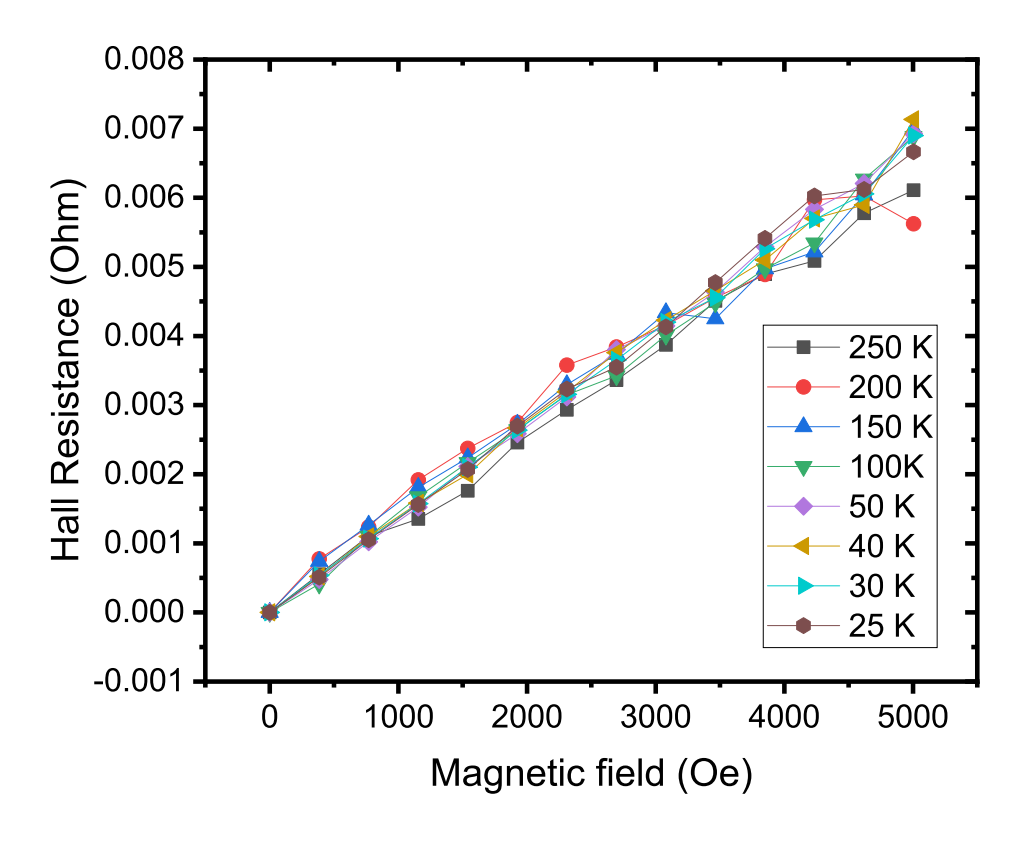


**Figure 4.8:** Hall resistance ( $R_{xy}$ ) of Ag120s as a function of magnetic field at different temperatures.

 $R_{xy}$  versus B in the figure 4.8 is a straight line passing through the origin. Therefore  $\frac{R_{xy}}{B}$  is the slope of the above curve. As the thickness of the film is of the order of 10 nm, taking this as the thickness of the sample, Hall coefficient versus temperature is shown in figure 4.9. Hall coefficient of noble metal Ag, reported in literature [28,29], is  $8.81 \times 10^{-11} m^3/As$ . Thickness of Ag120s should be a few 10 nm as the size of a single granule itself is about 20 nm. Therefore, it can be stated that the Hall coefficient in Ag120s is one order higher than that of a thick polycrystalline Ag film. The Hall coefficient is stable between 25 and 50 K but after that it was found reducing with temperature. A similar behaviour was found in polycrystalline Ag, where, the Hall coefficient is constant and then grows until about 30 K and then slightly reduces as temperature comes down further [29].

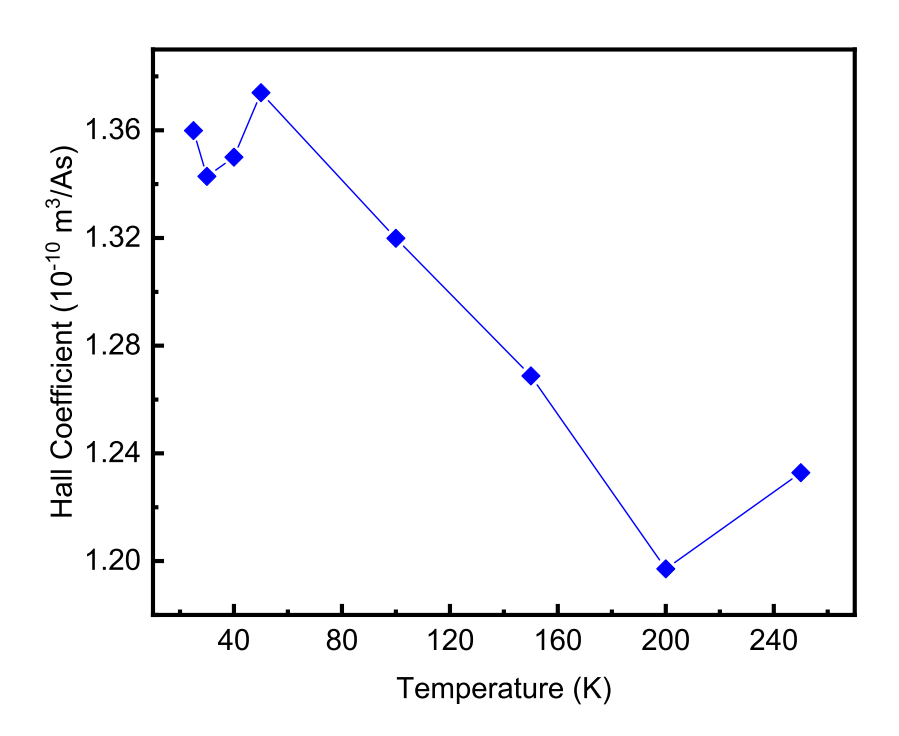


*Figure 4.9:* Hall coefficient as a function of temperature.

#### 4.4 Conclusion

The resistivity and Hall effect of Ag nanocluster films at the deposition times corresponding to a continuous to discontinuous transport were analyzed in this chapter. FESEM images show that the clusters form connected chains as the deposition time reduces. Resistivity measurement shows metallic nature in all the samples which fit to the modified Bloch-Gruneisen equation. An upturn in resistivity was found emerging which moves up in temperature as the deposition time reduces. An additional  $T^{1/2}$  dependence in resistivity was found fitting well in this region and this dependence shows a necessary connection with electron electron interaction. The coefficient of this additional term is found growing up as the deposition time reduces which is the result of dominance of electron electron interaction as the deposition time reduces. The Hall measurement of the Ag nanocluster film deposited for 120 seconds shows that the Hall coefficient is one order higher compared to the polycrystalline Ag film. Further, Hall coefficient is temperature independent though a trend of decrease in Hall coefficient is visible as temperature increases above 50 K.

# References

- [1] R. Rosenbaum, *Phys. Rev. B*, vol. 44, pp. 3599–3603, 1991.
- [2] A. Zabet-Khosousi and A.-A. Dhirani, *Chem. Rev.*, vol. 108, pp. 4072–4124, 2008.
- [3] D. Josell, S. H. Brongersma, and Z. Tőkei, *Annual Review of Materials Research*, vol. 39, no. 1, pp. 231–254, 2009.
- [4] Sampaio, K. C. Beverly, and J. R. Heath, J. Phys. Chem. B, vol. 105, pp. 8797–8800, 2001.
- [5] K.-H. Muller, J. Herrmann, G. Wei, B. Raguse, and L. Wieczorek, "Electron transport in nanoparticle assemblies," in 2010 International Conference on Nanoscience and Nanotechnology, (Sydney, Australia), pp. 316–318, IEEE, 2010.
- [6] C. Bansal, S. G. Praveen, J. T. T. Kumaran, and A. Chatterjee, *Scientific Reports*, vol. 5, p. 7685, 2015.
- [7] A. Bid, A. Bora, and A. K. Raychaudhuri, Physical Review B, vol. 74, 2006.
- [8] R. A. Matula, Journal of Physical and Chemical Reference Data, vol. 8, pp. 1147–1298, 1979.
- [9] Z. Cheng, L. Liu, S. Xu, M. Lu, and X. Wang, Scientific Reports, vol. 5, 2015.
- [10] S. Dhara, R. R. Chowdhury, and B. Bandyopadhyay, *Phys. Rev. B*, vol. 93, p. 214413, 2016.
- [11] R. W. Schmitt and M. D. Fiske, Phys. Rev., vol. 96, pp. 1445–1446, 1954.

- [12] T. Yoshiie, K. Yamakawa, and F. Eiichi Fujita, J. Phys. Soc. Jpn., vol. 37, pp. 572–572, 1974.
- [13] T. Endo, K. Sasaki, and T. Kino, *J. Phys. F: Met. Phys.*, vol. 15, pp. 1963–1974, 1985.
- [14] T. Siebold, F. Schuler, R. Huber, and P. Ziemann, Z. *Physik B Condensed Matter*, vol. 87, pp. 73–82, 1992.
- [15] C. Uher, D. C. Mundinger, and J. Bass, *Journal of Physics F: Metal Physics*, vol. 7, pp. 1691–1698, 1977.
- [16] U. M, I. H, and M. Y, *Phys Rev Lett*, vol. 108, pp. 066406–066406, 2012.
- [17] G. Bohnke, N. Croitoriu, M. Rosenberg, and M. Sostarich, *IEEE Transactions on Magnetics*, vol. 14, pp. 955–957, 1978.
- [18] T. Paramanik and I. Das, RSC Adv., vol. 5, pp. 78406–78413, 2015.
- [19] G. Knuyt, physica status solidi (b), vol. 123, pp. 763–771, 1984.
- [20] O. Touraghe, M. Khatami, A. Menny, H. Lassri, and K. Nouneh, *Physica B: Condensed Matter*, vol. 403, pp. 2093–2096, 2008.
- [21] G. Venkataiah, J. C. A. Huang, and P. Venugopal Reddy, *Journal of Magnetism and Magnetic Materials*, vol. 322, pp. 417–423, 2010.
- [22] R. W. Cochrane and J. O. Strom-Olsen, Phys. Rev. B, vol. 29, pp. 1088–1090, 1984.
- [23] B. L. Al'tshuler and A. G. Aronov, Sov. Phys. JEPT, vol. 50, no. 5, 1979.

- [24] Q. F. Zhang, X. Z. Wang, L. S. Wang, H. F. Zheng, L. Lin, J. Xie, X. Liu, Y. L. Qiu, Y. Z. Chen, and D. L. Peng, *Scientific Reports*, vol. 7, p. 11666, 2017.
- [25] C. Wan and P. Sheng, *Phys. Rev. B*, vol. 66, p. 075309, 2002.
- [26] Y.-N. Wu, Z.-Q. Li, and J.-J. Lin, Phys. Rev. B, vol. 82, p. 092202, 2010.
- [27] X. X. Zhang, C. Wan, H. Liu, Z. Q. Li, P. Sheng, and J. J. Lin, *Phys. Rev. Lett.*, vol. 86, pp. 5562–5565, 2001.
- [28] W. W. Schulz, P. B. Allen, and N. Trivedi, *Phys. Rev. B*, vol. 45, pp. 10886–10890, 1992.
- [29] C. M. Hurd, *Hall Effect in Metals and Alloys*. New York London: Plenum Press, 2002.

λ	/licro	fabrio	ration	of Mag	onetic	Tunnel	Junction	using	Photo	lithoe	rapl	ιv
T.A	TICIO	rabin	cauon	OI IVIA	gricuc	Iunici	Junction	usnig	111010	ուուսբ	upi	LУ

# Chapter 5

# Microfabrication of Magnetic Tunnel Junction using Photolithography

This chapter discusses the Microfabrication of MgO barrier Magnetic Tunnel Junction (MTJ) using photolithography. Optimization of MgO(001) growth on thermally oxidized silicon, Optimization of exchange bias in IrMn/FeCo bilayer, fabrication of MTJ, J-V Characteristics, Magnetoresistance (MR) measurement and circuit design and implimentation for low magnetic fields are elaborated here.

### 5.1 Introduction

When two ferromagnetic layers are separated by an insulator facilitating the tunneling conduction, electron transport is spin dependent, since the spin orientation of electrons are preserved in tunneling process. Probability of electron transport across the barrier is proportional to the product of the fermi level density of states

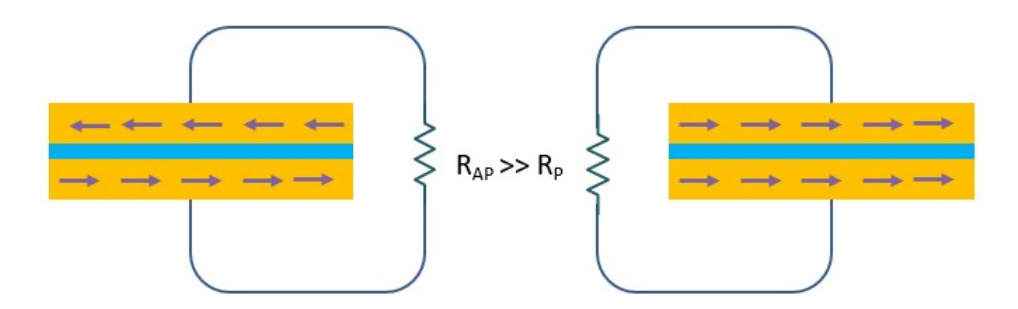


*Figure 5.1:* Schematic diagram showing the increased resistance when the moment of ferromagnetic layers are antiparallel in comparison with them parallel.

of spin up(spin down) electrons of both the electrodes. Therefore, when the spin orientations are opposite, resistance ( $R_{AP}$ ) is maximum and when the spin orientations of the electrodes are in similar direction, resistance ( $R_P$ ) is minimum as shown in figure 5.1. When the relative orientation of spin direction is  $\theta$  conductance in MTJ can be expressed as [1]

$$G(\theta) = \frac{1}{2}(G_P + G_{AP}) + \frac{1}{2}(G_P - G_{AP})\cos\theta$$
 (5.1)

where,  $G_P$  and  $G_{AP}$  are conductance when relative spin orientation is parallel and antiparallel respectively. Further, the tunneling magnetoresistance is defined as [1]

$$TMRratio = \frac{G_P - G_{AP}}{G_{AP}} = \frac{R_{AP} - R_P}{R_P}$$
 (5.2)

where,  $R_P$  and  $R_{AP}$  are the resistance when the spin of electrodes are parallel and antiparallel respectively. Compared to  $Al_2O_3$  amorphous layer, crystalline MgO exhibited huge TMR ratio which was explained as coherent tunneling of electrons occurring through crystalline MgO barrier [2].

Spin polarization of magnetic electrode can be written as

$$P = \frac{N \uparrow (E_F) - N \downarrow (E_F)}{N \uparrow (E_F) + N \downarrow (E_F)}$$
(5.3)

where,  $N \uparrow (E_F)$  ( $N \uparrow (E_F)$ ) is the density of states of spin up (down) electrons at fermi level. In terms of spin polarization, equation 5.2 can be written as

$$TMRratio = \frac{2P_1P_2}{1 - P_1P_2} \tag{5.4}$$

where,  $P_1$  and  $P_2$  are the spin polarization of electrodes at both sides of the tunnel barrier. This is an empirical relation obtained by Julliere and is called as Julliere model.

# 5.2 Optimization of the growth of MgO (001) over $Si/SiO_2$ substrate

Though MgO (001) substrate is the suitable candidate for the fabrication of MTJ with MgO as barrier while considering the lattice match of the device layers, it is very expensive. An alternative is to grow MgO (001) over some other substrates. The growth of MgO(001) over thermally oxidized Si(001) substrate has been studied. Base pressure of the sputtering chamber was  $6 \times 10^{-8}$  Torr. 20 nm of MgO has been sputter deposited over the substrate at 100 Watts power varying the Argon gas pressure, substrate temperature and post annealing temperature. From the X-ray diffraction images of the samples shown in figure 5.2, it is clear that when annealing temperature is above  $500^{0}$ C a broad peak is seen. MgO is still polycrystalline and it could be further optimized.

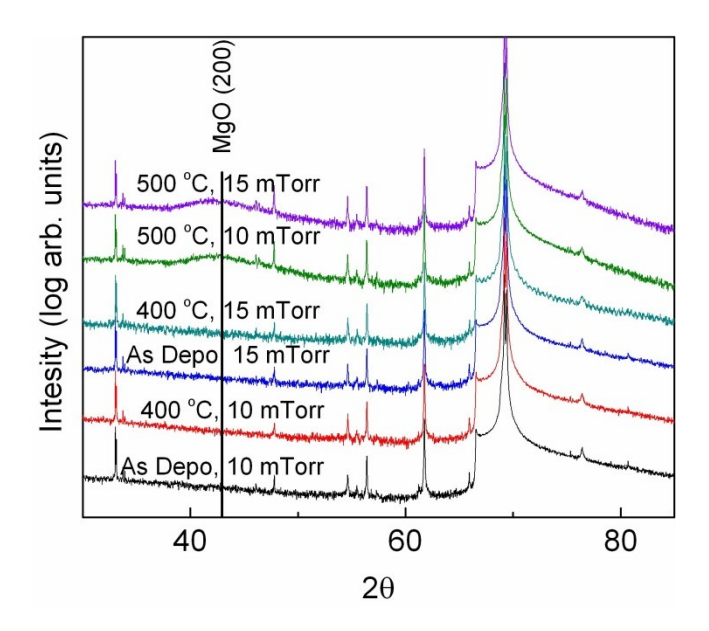


*Figure* 5.2: X-ray diffraction of MgO deposited over Si/SiO<sub>2</sub> at various deposition conditions.

# 5.3 Optimization of exchange bias in IrMn/FeCo bilayer

Pinning of the spin alignment of the reference layer to a single direction is achieved by exchange bias of ferromagnetic-antiferromagnetic bilayer. Exchange bias is an interface effect, where, the spins of antiferromagnetic layer is coupled with the spins of ferromagnetic layer at the interface [3,4]. This is the reason for the shift in the hysteresis loop to one side. Different theories have been established to explain the exchange bias phenomenon. However, it is hard to examine the interface effect experimentally to confirm any of the theories [3].

Exchange bias in IrMn/FeCo bilayer was studied by varying the thickness of both IrMn and FeCo. The films are annealed at  $250^{0}$ C for 1 hour applying 1 k Oe field using electromagnet in a vacuum furnace at a pressure below  $5 \times 10^{-6}$  Torr.

Coupling of interface layer to a single direction is achieved with this process.

Exchange bias has been studied at various antiferromagnetic thicknesses. The sequence of the multilayer is Ta(10)/Cu(15)/IrMn(x)/FeCo(5)/Ta(5), where the numbers in brackets are thickness in nanometers. The value of x are 4, 6, 8, 10 and 12. The M-H measurements of the films are shown in figure 5.3.

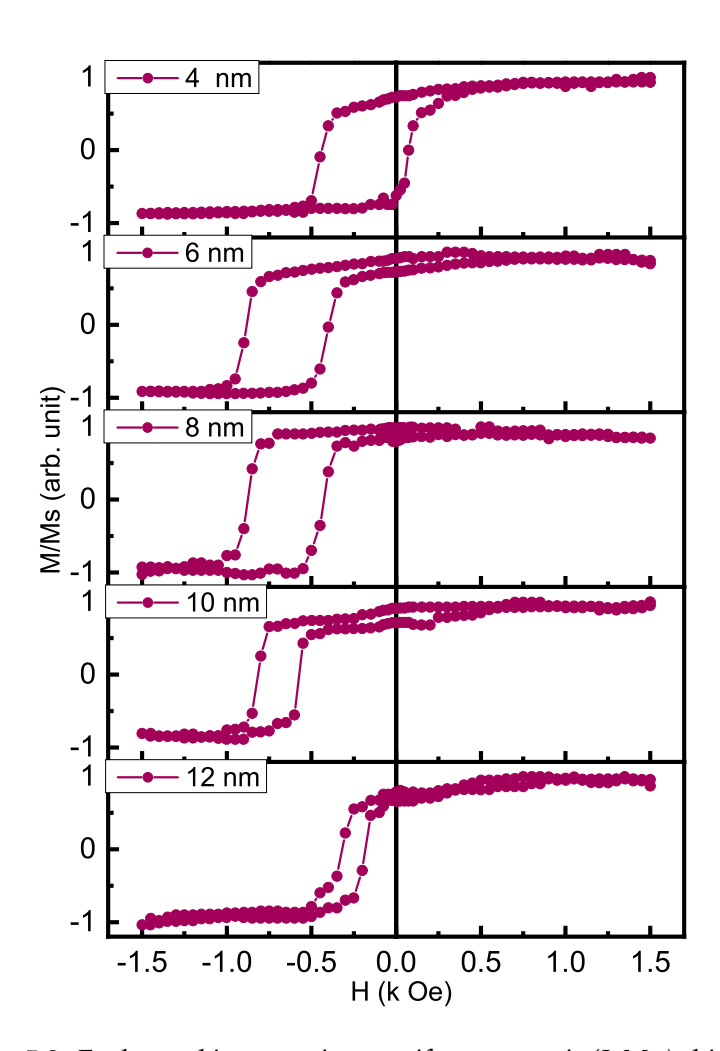
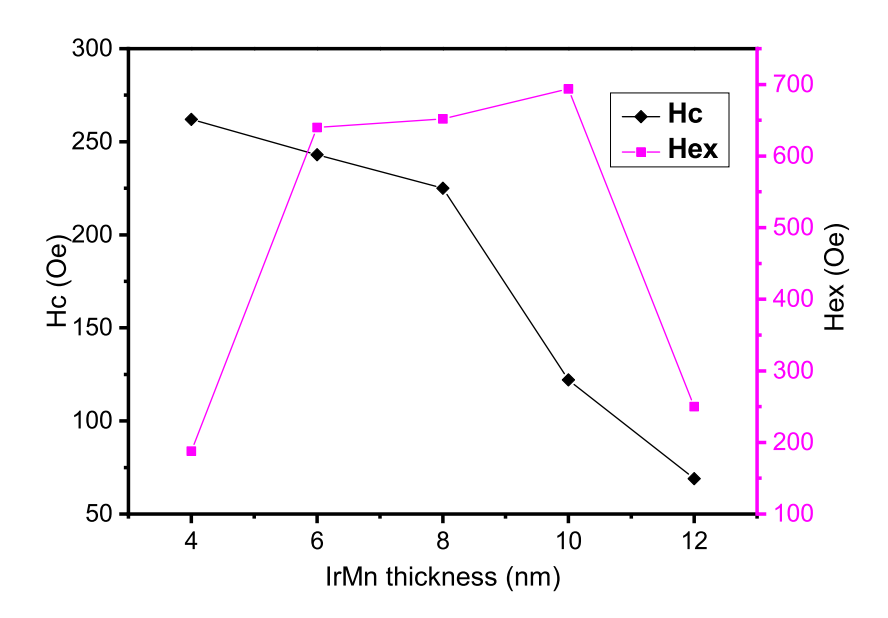


Figure 5.3: Exchange bias at various antiferromagnetic (IrMn) thicknesses.

It is seen that exchange bias reaches to a maximum as plotted separately in

figure 5.4. The maximum shift in the loop has been achieved with 10 nm of IrMn thickness. Further, fixing the IrMn layer thickness to 10 nm, thickness of FeCo layer has been varied (3, 5, 8 and 10 nms). M-H loop of them are shown in figure 5.5. The exchange bias and width of the hysteresis loop monotonically increases with decrease in FeCo thickness. This is shown in figure 5.6. However, the moment of FeCo decreases with the decrease in its thickness. Therefore, for the device fabrication, the thickness of the IrMn was set to 10 nm and FeCo thickness 5 nm.



**Figure 5.4:** Showing exchange field and coersive field as a function of thickness of antiferromagnetic layer.

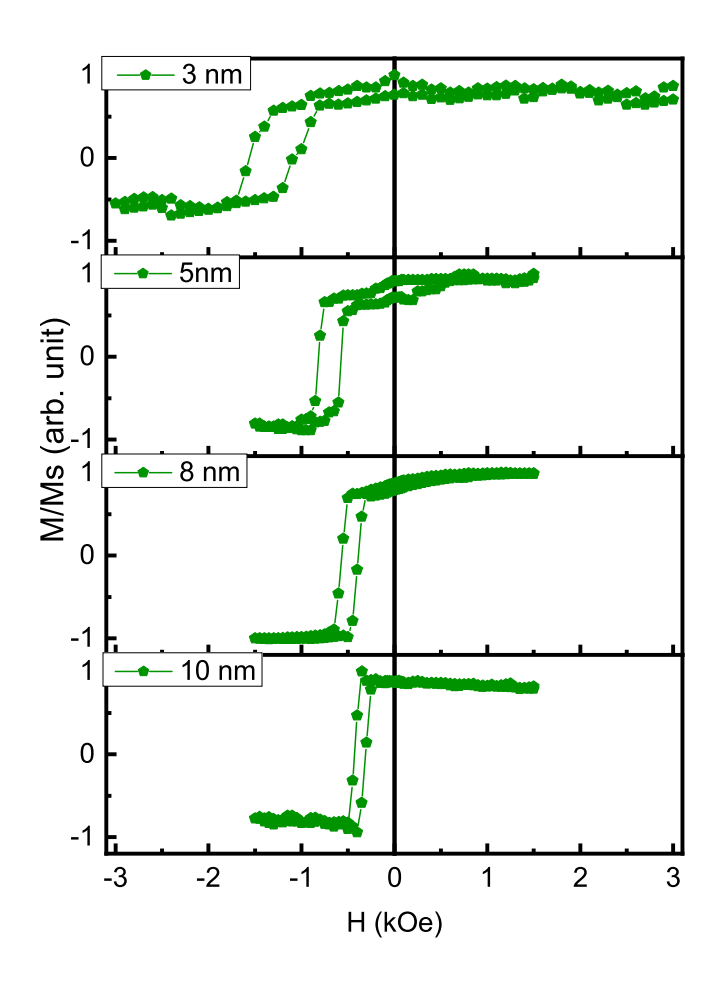
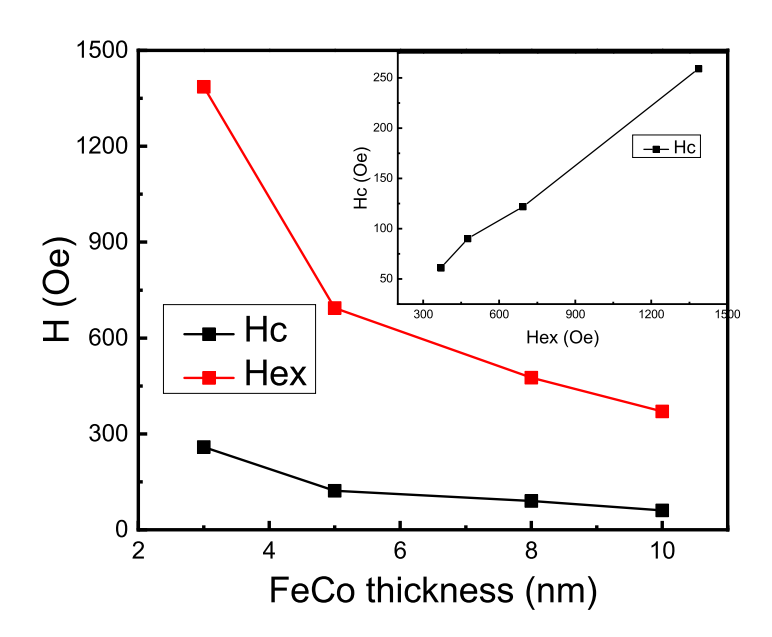


Figure 5.5: Exchange bias by varying the ferromagnetic layer thickness.



**Figure 5.6:** Coersive field and exchange bias field as a function of FeCo thickness with a fixed IrMn thickness of 10 nm.

# 5.4 Microfabrication of magnetic tunnel junction

A four set mask process of optical lithography patterning has been designed for the fabrication of MTJ. Designs were done in AutoCAD and the masks were prepared on a 5 sq.inch chrome coated quartz glass using e-beam lithography. A 1 sq. cm sample consists of 41 devices with 5 different dimensions. Each mask process consists of sample cleaning, photoresist deposition, patterning and film deposition.

Each mask process consists of the following. The sample is ultrasonically cleaned in acetone, iso-propanol and distilled water 5 minutes each. Afterwards, it is washed in running water and blown with Nitrogen gas. It is then annealed at  $105^{0}C$  for 10 minutes to remove water molecules over the surface. Photoresist is spin coated over this surface and baked at  $100^{0}C$  for 4 minutes. UV light is exposed through the mask over the sample and then wash out the exposed portion using developer and cleaned using distilled water. Sample is now ready for the deposition of required film with the desired portion free from photoresists. After the films are sputter deposited, remaining photoresists are removed from the sample along with the deposited films over the resist while washing in acetone. Now, a patterned film is obtained.

In the beginning, the lateral dimensions of the deposited device layers from the SEM image of the device have been compared with the designed dimensions. These are elliptical structures with five different dimensions as shown in figure 5.7. Table 5.1 shows the full length along the major and minor axis of the pillars measured from the FESEM image with designed dimensions in bracket. The measured values are found close to the designed dimensions.

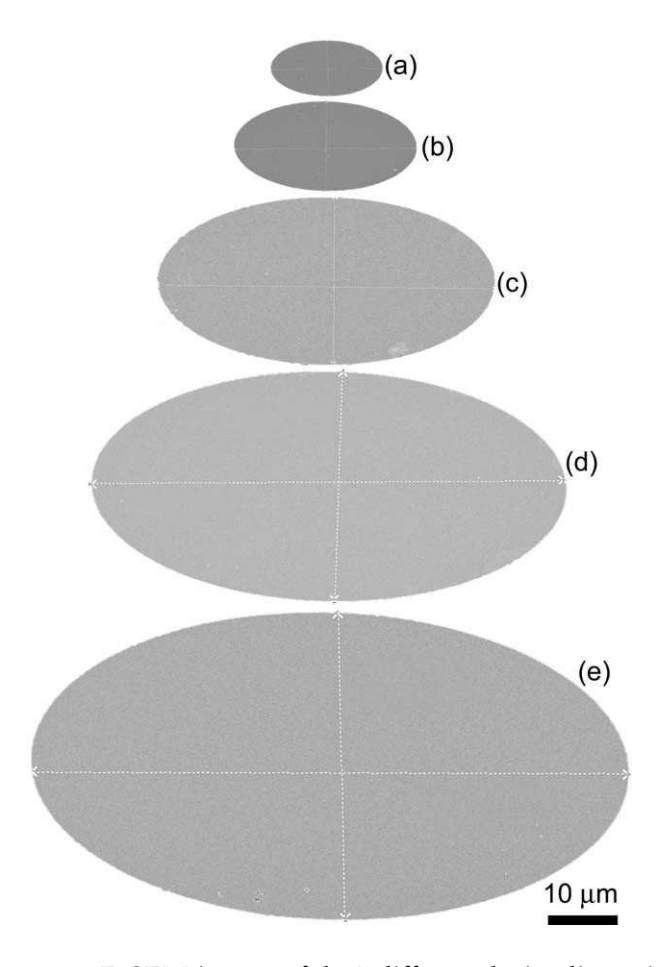


*Figure 5.7:* FeSEM images of the 5 different device dimensions.

MTJ device layers are deposited at a base pressure of  $5 \times 10^{-8}$  Torr and Argon pressure of  $2 \times 10^{-3}$  Torr. Each mask processes of MTJ Microfabrication is conducted as follows.

In the first mask process of the fabrication, bottom electrode is fabricated over the 1 sq. cm thermally oxidized Si(001) substrate. The layer sequence are Ta(10)/Cu(15). Optical micrograph after the process is shown in figure 5.8(a). Tandalum is a good adhesive and this set of underlayers have been optimized for

Sl.No.	length along the axis (µm)			
	Major axis	minor axis		
1.	8.15 (8)	16.54 (16)		
2.	13.27 (13)	26.90 (26)		
3.	24.50 (24)	49.92 (48)		
4.	34.71 (34)	70.34 (68)		
5.	44.98 (44)	87.78 (88)		

**Table 5.1:** The designed dimensions of Major and minor axis of elliptical junctions are depicted in the table. The length measured from the FeSEM image of the fabricated pillar are shown in bracket.

the exchange bias of IrMn/FeCo bilayer.

In the second mask process, the elliptical structures are transferred and the device layers are deposited with exchange bias at the bottom such as IrMn(10)/FeCo(5)/MgO(2,3)/FeCo(5). Micrograph of the device after the second mask process is shown in figure 5.8(b). The elliptical shape facilitates to orient the spins of electrodes towards the length of major axis by utilizing the shape anisotropy.

Third step is the deposition of insulating layer to avoid direct contact between top and bottom electrodes. 20 nm of MgO is deposited which is not observed from optical microscope since it is transparent. Therefore, micrograph shown in figure 5.8(c) is that taken just after patterning. Pillar is capped with resist to give top contact.

Last step is the deposition of top electrode, which comes over the MgO insulation layer deposited in the previous step and touches the top of the pillar. Top

layers are Ta(10)/Cu(15)/Ta(10)/Cu(15)/Ta(10)/Cu(15). After washing out the resist, the final image of a single device is shown in figure 5.8(d). A set of MTJs on a substrate is shown in figure 5.9(a) and a zoomed view of the pillar is shown in 5.9(b).

The sample is then annealed at  $250^{\circ}C$  for 1 hour in 1 k Oe magnetic field to pin the bottom electrode. Major axis of the pillar layer is aligned to the magnetic field to utilize the shape anisotropy.

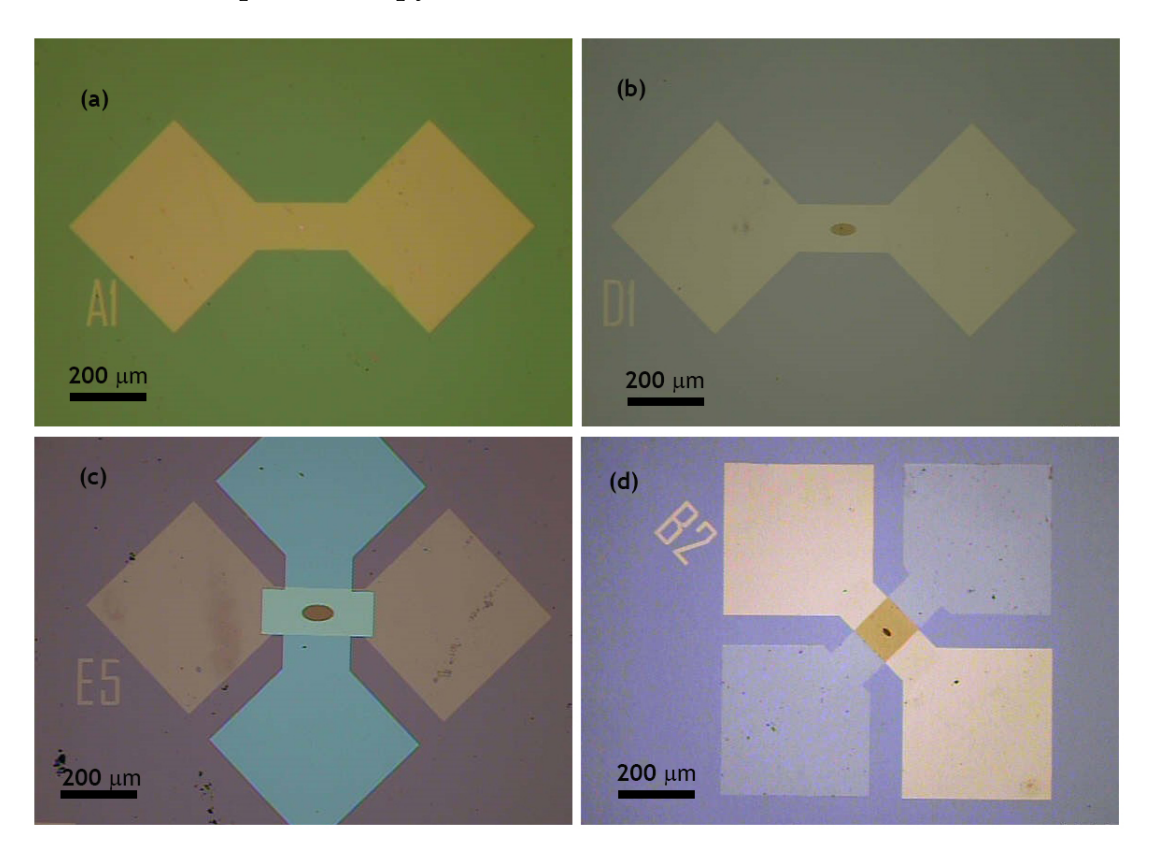


*Figure 5.8:* Optical image of the MTJ device after each step of lithography process.

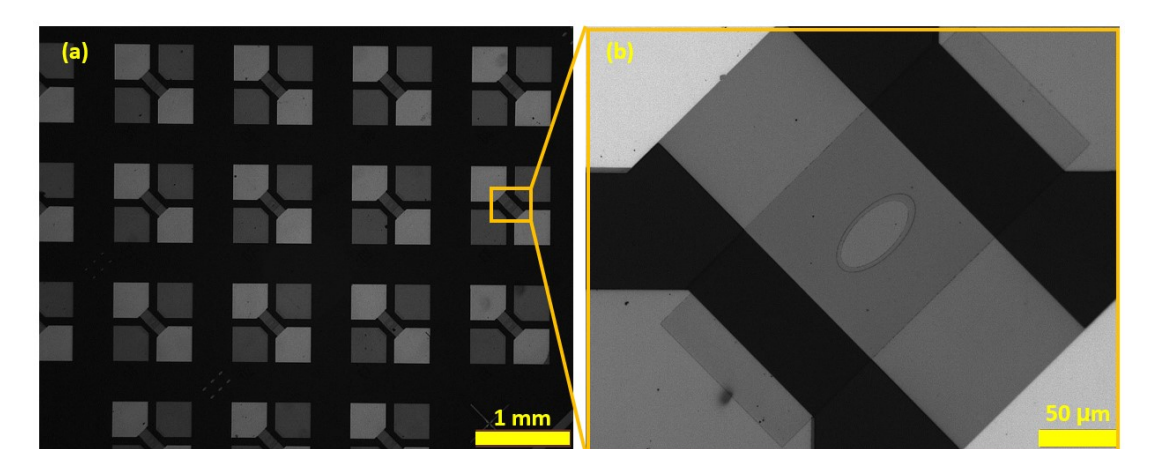


**Figure 5.9:** Optical image of (a) multiple MTJ devices on a substrate and (b) the zoomed view of elliptical device of a junction

# 5.5 J-V characteristics of MTJ

Current density - voltage (J-V) characteristics of the MTJs were measured in LakeShore make probe station using Agilent 1500B semiconductor device analyzer. The nonlinear curve obtained was fitted to Simmon's relation for tunneling current approximated to low voltages [5]. Current density, *J*, according to the above relation is,

$$J = \beta(V + \gamma V^3) \tag{5.5}$$

where,

$$\beta = \frac{3}{2} \frac{e^2 (2m\varphi)^{1/2}}{h^2 s} \exp\left(-A\varphi^{1/2}\right),\tag{5.6}$$

$$\gamma = \frac{(Ae)^2}{96\varphi} - \frac{Ae^2}{32\varphi^{1/2}} \tag{5.7}$$

and

$$A = 4\pi (2m)^{1/2} s/h \tag{5.8}$$

Here, V is the voltage applied across the junction,  $\varphi$  the barrier height, s the thickness of the barrier, e the charge of electron, m the mass of electron and h is the plank's constant.

The fits of Simmons relation to the J-V characteristics of 2 nm and 2nm junction MTJs at 300 K and 3 nm junction MTJ at 70 K are shown in figure 5.10, 5.11 and 5.12 respectively. The parameters  $\alpha$  and  $\beta$  were obtained by fitting the IV data with equation 5.5 using levenberg-marquardt algorithm in matlab. Equation 5.7 is a quadratic in A, which yields  $\beta$  in equation 5.6 as a function of  $\varphi$  alone. Bisection method is then used to find out the value of  $\varphi$  and from this, value of A and S are found.

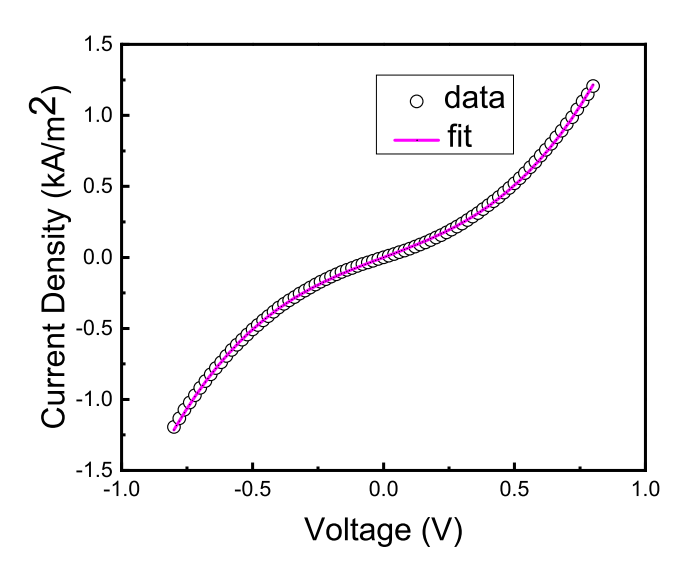


*Figure 5.10: IV characteristics of 2 nm MgO tunnel junction measured at 300 K fitted to Simmon's relation for tunnel current.* 

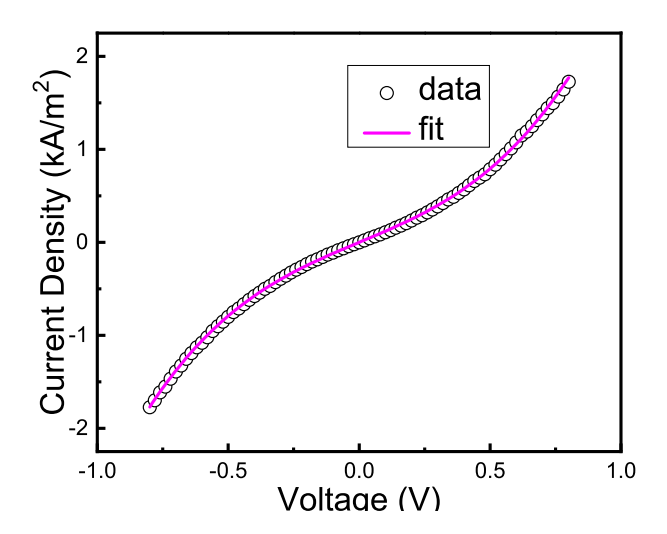
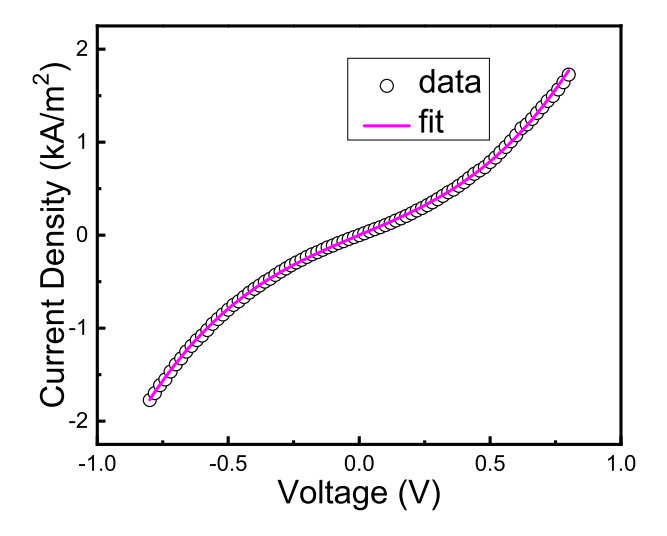


Figure 5.11: IV characteristics of 3 nm MgO barrier measured at 300 K and fit to Simmon's relation for tunneling current.



**Figure 5.12:** IV characteristics of 3 nm MgO barrier junction measured at 70 K and fitted to Simmon's relation for tunneling current.

Barrier thickness	Temperature	Parameters from fit		R-square
(nm)	(K)	s (nm)	φ (eV)	
2	300	1.9677	0.9416	0.9994
3	300	2.4388	0.8825	0.9998
3	70	2.6489	0.7726	0.9983

**Table 5.2:** The fitting parameters of IV characteristics of MTJ with 2 nm and 3 nm thick barriers are depicted here.

Barrier thicknesses obtained from the fits are found to be close or less than the expected thickness. This has been understood as due to image forces which reduces the lateral area of the potential barrier [6].

Quantum mechanically, there is a finite probability for electrons to tunnel across the potential barrier as elucidated with the WKB approximation [7]. Transmission probability in one dimension can be expressed as,

$$T(E) \approx exp\left(-2\int_0^t \sqrt{2m_e[U(x) - E]/\hbar} dx\right)$$
 (5.9)

where,  $m_e$  and E are mass and energy of electron respectively and t is the thickness of the barrier. Tunneling probability exponentially decay with increase in the barrier thickness and barrier height and it is independent of temperature. From the J-V characteristics it can be seen that the current is independent of temperature and current density has been decreased with increase in barrier thickness. Therefore, the conditions for quantum mechanical tunneling have been satisfied in these films.

# 5.6 Tunneling Magnetoresistance of MTJ

Tunneling Magnetoresistance has been measured in cryomagnetic probe station using Keithley 2635 source meter following the equation 5.2. Tunneling magnetoresistance of a 2 nm MTJ device has been shown in figure 5.13. A TMR of 7 % has been obtained.

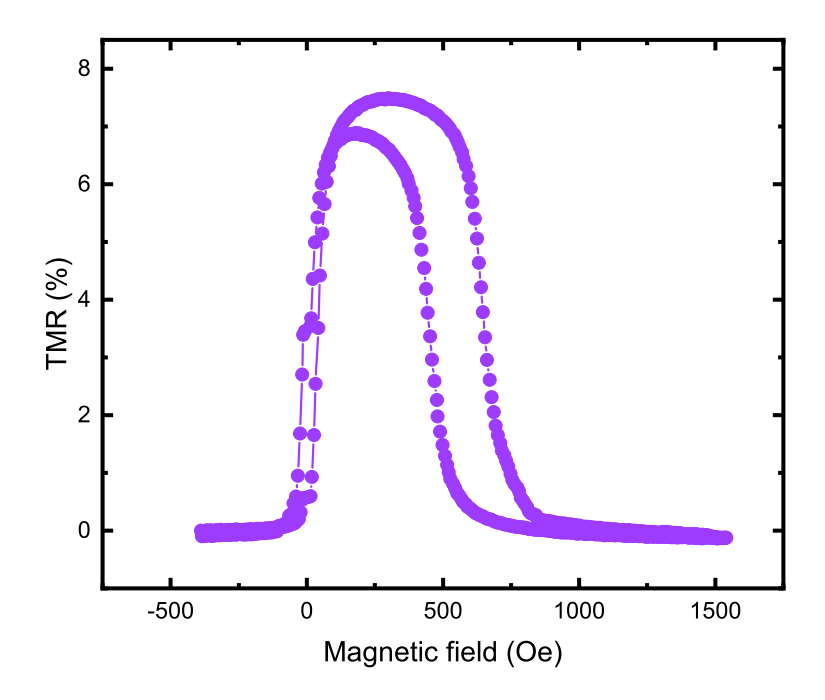
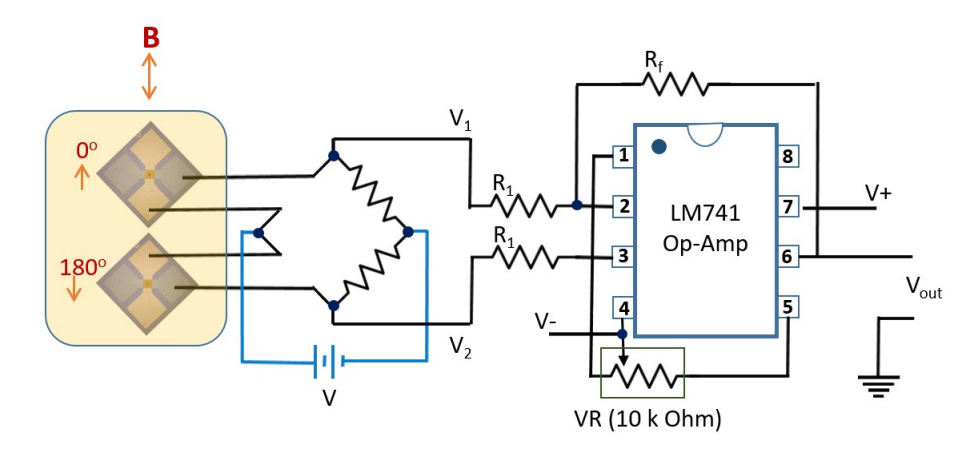


Figure 5.13: TMR of a 2 nm MgO barrier MTJ.

# 5.7 Circuit design for MTJ sensor

Magnetic field sensors based on MTJ are much better compared to that from Hall sensor. This is due to a better response to a small change in magnetic field from a MTJ compared to a hall sensor. A circuit design has been established to use the MTJ for magnetic field sensor applications as shown in the figure 5.14.



*Figure 5.14:* Circuit design of low field magnetic field sensor using MTJs.

Two MTJs have been kept with their zero field magnetization of reference layer antiparallel to each other. They have been used as two resistor component of bridge circuit. Voltage is supplied to the diagonal ends of the nodes of the bridge and the output is taken from the other two nodes. Other two resistors are suitably chosen so that the output voltage becomes the least without an external magnetic field. The output of the bridge circuit is shown in figure 5.15. the output is amplified using LM741 op-amp for a gain of 200 by choosing  $R_1$  as 50 Ohm and  $R_f$  as 10 K Ohm. The output, thus obtained as a function of magnetic field is shown in figure 5.16.

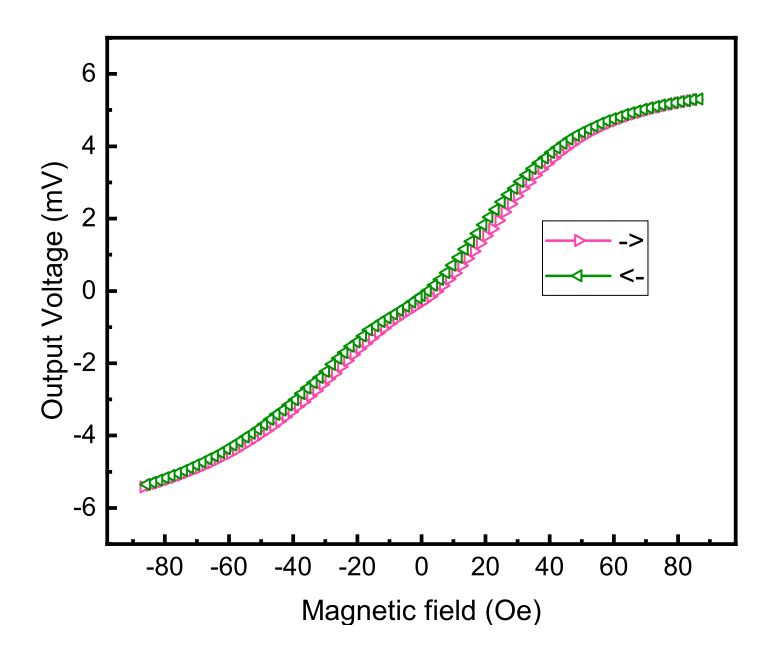


*Figure 5.15:* Output voltage obtained from the sensor circuit.

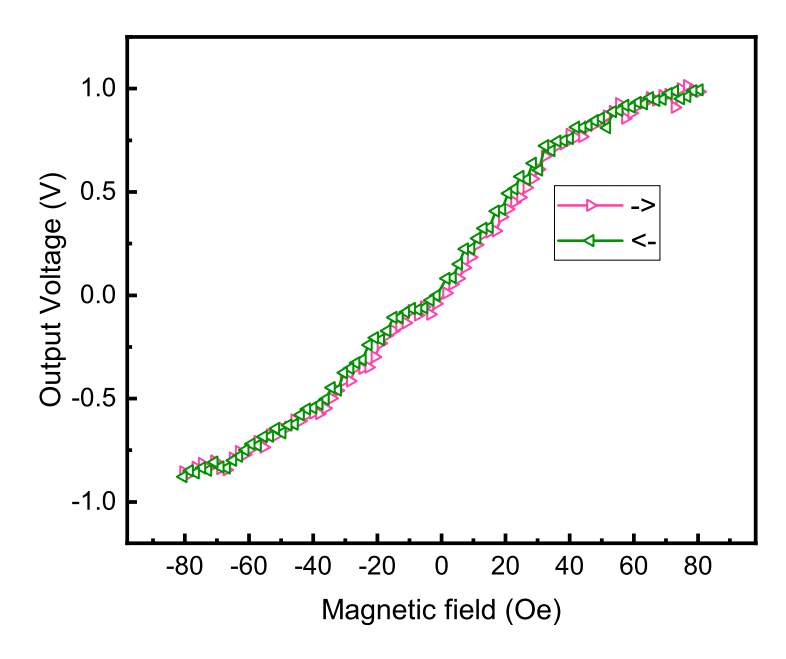


Figure 5.16: Output voltage obtained from the sensor circuit after amplification using LM-741 op-amp.

## 5.8 Conclusion

A method of fabricating Magnetic Tunnel Junction with photolithography as the only patterning unit has been established. This is a cheaper and simple method in comparison with the usual fabrication processes of MTJ using ion etching. Growth of MgO (002) over thermally oxidized silicon substrate has been studied as this is the best underlayer for MgO barrier MTJ. Exchange bias of IrMn/FeCo bilayer has been optimized to achieve unidirectional anisotropy at maximum range from zero field on positive and negative axis. Optimum thickness of IrMn found is 10 nm. Device pillar dimensions have been verified using SEM micrograph. Further, the MTJ fabrication process has been explained. IV characteristics of the resulting device has been measured, which shows properties of tunneling. This was fitted to Simmon's relation for tunneling current. A TMR of 7 % has been obtained from a 2 nm film. A circuit has been designed for sensor application embedding two MTJs as components of wheatstone bridge and amplifying the output. The outputs before and after amplifying have been characterized.

# References

- [1] J.-G. J. Zhu and C. Park, *Materials Today*, vol. 9, pp. 36–45, 2006.
- [2] W. H. Butler, X.-G. Zhang, T. C. Schulthess, and J. M. MacLaren, *Physical Review B*, vol. 63, p. 054416, 2001.
- [3] M. Kiwi, Journal of Magnetism and Magnetic Materials, vol. 234, pp. 584–595, 2001.
- [4] F. Radu and H. Zabel, arXiv:0705.2055 [cond-mat], vol. 227, pp. 97–184, 2008. arXiv: 0705.2055.
- [5] J. G. Simmons, Journal of Applied Physics, vol. 34, pp. 238–239, 1963.
- [6] T. Kiyomura, Y. Maruo, and M. Gomi, *Journal of Applied Physics*, vol. 88, pp. 4768–4771, 2000. Publisher: American Institute of Physics.
- [7] H. Swagten, "Chapter One Spin-Dependent Tunneling in Magnetic Junctions," in *Handbook of Magnetic Materials*, vol. 17, pp. 1–121, Elsevier, 2007.

# Chapter 6

# Conclusion

This chapter summarizes the results discussed in this thesis. Further, future direction to be continued in this research is analyzed here.

# 6.1 Summary

The use of nanomaterials can be traced back to 600 B. C. Wootz steel manufactured those times in ancient India consisted of Carbon nanotubes and cementite nanowires and it was exported around the world. The pottery in the middle ages and renaissance often shows metallic glitter produced using Copper and gold nanoparticles [1]. However, it took long years until 1959 - when Richard Feynman pointed out the significance of the materials at reduced size in his talk "There is plenty of room at the bottom" to bud the thought that there are fascinating phenomena hidden in the nano-world [2]. Further, Invention of Scanning Tunneling Microscope in 1981 offered a stepping stone for scientific community to really

move in to the nanoscales and see the mysterious properties of the nanomaterials. Progress of nanoscience, afterwards, was tremendous with a large variety of applications drawing out from the research [3].

In the modern world, the electronic industry is still ruled by the semiconductor technology. However, it won't be too long to replace the electronic technologies from semiconductor to metallic and magnetic nanomaterials while looking at the tunable nature of these materials in the quantum world. The progress of research and publications show that a large amount of research is conducted in laboratories across the world and imbibing this into technology can miniaturize with enhanced properties of the devices.

The nanostructures have been widely studied to explore the properties to convert into applications. A considerable amount of theoretical works has been come out to perceive the transport mechanisms in nanomaterials, for example single electron transistor, spin FET, etc. Further, electron transport in nanomaterial films have shown diverse mechanisms. This diversity arises from the size, structure and dimenstions of nanostructures. As the size of the constituent element in a material comes to nanoscale, surface to volume ratio of atoms increases drasticall and the energy level separation increases causing quantum confinement. Electronic conduction can be tuned in granular films by controlling the percentage of the amount of metal or insulator and in nanocluster films by reducing the thickness of the film. Metal-insulator transition in these structures have not yet been understood propertly. A vast amount of research is in progress over magnetic tunnel junctions observing huge applications owing to the giant TMR ratio. This shows the relavance of the thesis as it explains the transport mechanism in nanogranular and nanocluster films around metal-insulator transition by controlling the inter-

cluster separation and dimensionality and a simple and cost effective technique of microfabricating magnetic tunnel junction using optical lithography.

FePt-C is a strong candidate to study as the superparamagnetism occurs only at a size less than 3 nm because of the huge perpendicular magnetic anisotropy associated with the L1<sub>0</sub> ordering in these films. Intergranular distance of FePt-C nanogranular film has been modified by co-sputtering or sequential sputtering at various substrate temperatures. The resistance measured in these films show varying so much, i.e., from a  $k\Omega$  to a few hundred  $k\Omega$  at room temperature. Depending on the intergranular separation, different conduction mechanisms such as ES-VRH, M-VRH and extended critical region have been observed above 25 K. This explores the possibility of tuning the conduction regimes by varying intergranular distance. In disordered films metal-insulator transition is decided by the Anderson criteria. This has been simplified by Zenavova and Zebrodskii. This calculation shows that below 21 K the samples are metallic. An extrapolation of VRH fit to low temperatures shows that conductivity is enhanced at low temperature comparing to the hopping mechanism. The enhanced conduction at zero field was attributed to the intergranular interaction between perpendicular magnetic ordered granules. This was explained with a model. The tunablility of conduction in these structures can be utilized for spin dependent electron channel in spin FET.

Noble metals such as Au and Ag are the most suitable materials to study conduction in nanoclusters as the oxidation is comparably limited. Ag nanocluster films of near monolayer has been prepared by varying deposition time. A continuous to quasi continuous Ag nanocluster films have been obtained in this manner. Electron transport in these films show normal metallic behavior to a resistivity

minimum which moves up in temperature as deposition time reduces. Electron transport in the metallic regime fits to Bloch-Gruneisen equation modified to include carrier scattering. The minima in resistivity was fitted with an additional  $\sqrt{T}$  dependence of resistivity responsible for electron-electron interaction. The deybe temperature associated with electric resistance was found reduced as previously observed in silver nanowires. As the deposition time reduces the minimum in resistance moves up in temperature as well as the contribution from e-e interaction enhances. Though a logarithmic dependence was observed in nanoclusters previously, the mechanism has to be further understood along with Hall effect. Hall effect measurement of the film which does not show a minima is found to have the Hall coefficient enhanced for one order. Further, Hall coefficient was found showing similar trend previously reported in metallic Ag film.

Magnetic tunnel junctions have been one of the leading research topic resulting from huge magnetoresistance produced in them. A versatile fabrication technique has been established to microfabricate MTJs using only optical lithography. The best underlayer for MgO barrier tunnel junction is MgO (001). The growth of MgO (001) over thermally oxidized silicon has been studied by varying the Argon pressure and annealing temperature. Exchange bias of IrMn/FeCo bilayer has been optimized to achieve unidirectional reference electrode. The optimized thickness of IrMn is 10 nm. The microfabrication technique has been elaborated step by step. J-V characteristics of fabricated tunnel junctions fitted to Simmon's relation for tunneling current. A TMR of upto 7 % has been obtained. Further, a circuit has been designed and implemented using MTJs to use it as magnetic field sensor for low fields. This has to be further studied to engineer them for measuring higher magnetic fields.

# 6.2 Future perspectives

The nanostructures offer wide applications in daily life due to its modified physical properties, in comparison with its bulk counterparts or atomic form, arising from the large surface to volume ratio as well as the quantum confinement. Since these structures can be carefully controlled over the size, structure and dimensionality, it can be properly tuned for various applications.

The electron transport in nanogranular and nanocluster films has been studied at large. However, there are different preparation methods and dimensions. Electron transport in lower spacial dimensions is an area that has to be further explored. The physics responsible for different conduction mechanisms has to be understood to unify them. This requires further study in these systems by variying different controlling parameters. The metal nanogranular films have shown giant Hall effect, where Hall coefficient increases upto 4 orders compared to its bulk form. This enhancement has been attributed to the interference of conduction electrons when the size of the granule becomes comparable to the dephasing lenght of electrons. Scaling law of anomalous Hall effect is violated in nanocluster and nanogranular films. Nanoclusters are the suitable candidate to understand these studies as there is a proper control over the size of the clusters.

Invention of magnetic tunnel junction has a huge impact in modern technology. Spin dependent transport and spin filtering has been efficiently utilized in these devices. As the quality of the devices are improved the expenditure of manufacturing also has to be considered. Huge TMR ratio in MTJs can be properly utilized for magnetic field sensor applications with efficient engineering ways.

The two dimensional nanomaterials are promising materials to replace many of the semiconductor technologies as these films can be tuned at large. Exploration of the physical mechanism associated with these structures have a great importance to modify the structure for different requirements. This thesis provides a glimpse of this great truth.

# References

- [1] K. Sanderson, Nature, 2006.
- [2] J. Gribbin and M. Gribbin, Richard Feynman: A Life in Science. 1997.
- [3] L. K. Foong, M. M. Foroughi, A. F. Mirhosseini, M. Safaei, S. Jahani, M. Mostafavi, N. Ebrahimpoor, M. Sharifi, R. S. Varma, and M. Khatami, RSC Adv., vol. 10, pp. 15430–15460, 2020.

## **Publications, Conferences and Workshops**

#### **Publications**

- [1] **Joshy Joseph**, Jian Wang, B S D Ch S Varaprasad, Y K Takahashi, K Hono and A Rajanikanth, "Tunable Electron Transport in FePt-C nanogranular films with intergranular separation", Mater. Res. Exp., 7, 046405, 2020.
- [2] **Joshy Joseph**, C Bansal, K Jonathan Reddy and A Rajanikanth, "Electron electron interaction dominated electron transport in quasi-continuous silver nanocluster films" (accepted for publication in AIP Advances)

### Workshop/Conference

- [1] International Conference on "Magnetic Materials and Applications IC-MAGMA", DMRL, Kanjanbagh, Hyderabad, Poster: "Fabrication of Magnetic Tunnel Junction using Photolithography", 1-3 February, 2017.
- [2] Symposium on Frontiers in Nanoscience and Technology, University of Hyderabad, Hyderabad, 6-7 April 2018
- [3] Workshop on "Functional Magnetic Materials", University of Hyderabad, Hyderabad, 26th February 3rd March 2018.
- [4] National conference on "Physics at Small scales and Advanced Materials", University of Hyderabad, Poster: "Magnetic Tunnel Junctions, Fabricated using Optical lithography", 8-9 September 2017.
- [5] Workshop on "VLSI Designs and Sensors in Systems", University of Hyder-

abad, Hyderabad, 20-25 March, 2017.

[6] National Conference on "Frontiers in Physics", Hyderabad University, Hyderabad, 17-18 October, 2014.

[7] INUP familiarization workshop on "Nanofabrication Technologies", IISC, Bangalore, 21-23 May, 2014.

## Plagiarism report

# Electron Transport in 2Dimensional Films: FePt-C Nangranular Films, Ag Nanocluster Films and Microfabricated Magnetic Tunnel Junctions

by Joshy Joseph

**Submission date:** 17-Nov-2020 03:29PM (UTC+0530)

**Submission ID:** 1448831454 **File name:** thesis\_joshy.pdf (11.6M)

Word count: 20694 Character count: 105425

Librarian
Indira Gandhi Memorial Library
UNIVERSITY OF HYDERABAD

Central University P.O. HYDERABAD-500 045.

# Electron Transport in 2-Dimensional Films: FePt-C Nangranular Films, Ag Nanocluster Films and Microfabricated Magnetic Tunnel Junctions

ORIGINALITY REPORT			
9% SIMILARITY INDEX	2% INTERNET SOURCES	8% PUBLICATIONS	1% STUDENT PAPERS
PRIMARY SOURCES			
Varapra Hono, A electron in FePt-	oseph, Jian Wang Isad, Yukiko K Tal Ammanabrolu Raja I transport with int IC nanogranular fi ICh Express, 2020	kahashi, Kazu anikanth. "Tur ergranular se	nable paration
Varapra Rajanika intergra	oseph, Jian Wang sad, Y K Takahas anth. "Tunable ele nular separation in Materials Research	shi, K Hono, A ectron transpo n FePt-C nand	rt with ogranular
3 Submitt Singapo Student Pape		chnological U	Iniversity, <1%
4 "Sensor Publication	rs Set", Wiley, 199	95	<1%

Librarian
Indira Gandhi Memorial Library
UNIVERSITY OF HYDERABAD
Central University P.O.
HYDERABAD-500 045